Blue Laser Source for Laser-Induced Fluorescence

Jesper Holm Lundeman

Doctoral Thesis
2008

Lund University

Blue Laser Source for Laser-Induced Fluorescence

Printed in Sweden by Media-Tryck, Lund, 2008

Division of Atomic Physics
Department of Physics
Faculty of Engineering, LTH
Lund University
P.O. Box 118
SE–221 00 Lund
Sweden

http://www.atom.fysik.lth.se
http://www.atom.fysik.lth.se/medweb

ISSN 0281-2762
Lund Reports on Atomic Physics, LRAP-396

ISBN 978-91-628-7570-1

To my beloved
Anja, Anton & Eliane

Abstract

Laser-induced fluorescence is a clinical diagnostic tool, used for tumor demarcation and detection. The technique relies on the injection or topical application of a light sensitive drug called a photosensitizer. This substance has the ability to be accumulated to higher concentrations in cancer cells than in normal cells. This accumulation procedure takes from a few hours to several days, depending on the photosensitizer used. When the phtosensitizer is illuminated with 405 nm light it will fluoresce in the red spectral region. The difference in photosensitizer concentration from cancer cells to noncancer cells can therefore be detected as a change in the fluorescence level. Two photosensitizers were used in this work: ALA-induced PpIX and mTHPC. A high power laser system is needed in order for the fluorescence detection to work when imaging large areas in real time. The suppression of the ambient lighting can be overcome using a pulsed laser system combined with a time gated camera.

In this thesis such a laser system has been developed. Several factors were constraining the system, as it needed to be mobile, clinical certifiable, inexpensive and compact, all in order for easy operation in a clinical setting. The target wavelength of the system was 405 nm, and this was realized by doubling the output of an 810 nm diode laser. In order to generate sufficient power at 810 nm, an external cavity tapered laser amplifier system was constructed. It consists of a tapered diode, that were anti-reflection coated on both the front and back facets. On the back facet, a collimating lens is directing the output beam towards a diffraction grating, used in the Littrow configuration, that spectrally stabilizes the laser system and determines the operating wavelength. The 1st order diffracted beam from the grating was coupled directly back into the amplifier, resulting in an output beam from the laser diode with 1.9 W of output power at 810 nm. The tuning range of this system was 30 nm and could be achieved be a simple rotation of the diffraction grating.

In order to effectively frequency double the 810 nm laser beam, an external resonator containing a periodically poled KTP crystal was constructed. Periodically poled KTP was found to be sus-

ceptible to a photochromic damage called grey-tracking, at the power levels needed for generation of the 405 nm output beam. A very compact resonator design was used, as it allowed for a large acceptance bandwidth from the pump laser.

For stable continuous wave operation the external resonator needed to be phase locked, using a polarization sensitive electronic circuitry. An output power of 300 mW at the target wavelength of 405 nm was obtained from this external resonator system. Thermal issues in the crystal was severely limiting the output power of the system, necessitating the use of a very long nonlinear crystal of 30 mm in length. The pulsed laser source was realized by scanning the external resonator on and off resonance and more than 700 mW of output power was obtained. Both the continuous wave and pulsed laser systems were clinically used on patients diagnosed with skin cancer and underwent photodynamic therapy.

Populärvetenskaplig sammanfattning

En stadig voksende del af befolkningen rammes af forskellige former for cancer og relaterede sygdomme. Der findes i dag mange metoder til behandling af cancer såsom strålebehandling, kemoterapi og kirurgiske indgreb. Disse metoder er dog invasive over for patienten, og i en del tilfælde går rask væv til grunde under behandlingen. Dette kan skyldes at det er umuligt at afgrænse cancer området med sikkerhed, og derfor fjernes væv "for en sikkerheds skyld". Et andet problem kan være tilgængeligheden af tumoren, der kan ligge dybt under huden og derfor ikke kan nås uden at beskadige andet væv.

Fotodynamisk terapi (PDT) er en bahandlingsform som virker ved at et lysfølsomt stof, en *photosensitizer*, gives til patienten. Det kan ske ved påsmøring på huden, intravenøs injektion eller ved indtagelse som mikstur. Dette stof vil så fordele sig rundt i vævet, men vil ophobes i større mængder i cancer væv end i rask væv. Ved efterfølgende belysning med laserlys vil det lysfølsomme stof kunne starte en kædereaktion i cellen, som ultimativt vil føre til cellens destruktion. Denne reaktion er ikke afhængig af at cellen er en cancer celle, men da ophobningen er størst i disse celler vil skaden være langt større i disse celler end i rask væv.

I denne afhandling ses på brugen af laserlys til at diagnosticere væv for cancer inden der behandles. Dette er nyttigt da man derved vil kunne bruge proceduren som en simpel screening, f.eks. for hudcancer. Man vil også kunne afgrænse et eventuelt kirugisk indgreb mere nøjagtigt, og derved spare rask væv. Ydermere vil man kunne lave en simpel optisk biopsi uden at fjerne noget væv fra patienten, for at be- eller afkræfte en formodning om cancer. I områder hvor der kun er en lille mængde væv til rådighed, som eksempelvis i stemmebåndene, mave og tarm, hjernen, etc. vil en sådan skånsom screening være at foretrække, i stedet for den invasive og destruktive biopsi.

Den diagnostiske metode kaldes laser-induceret fluorescens måling, og bygger på det faktum at det aktive lysfølsommme stof

vil udsende rødt lys, efter at det er blevet belyst med blåt lys, begge farver er dog afhængig af det eksakte valg af photosensitizer. To typer er blevet brugt i det eksperimentelle arbejde: ALA-induceret PpIX og FosPeg (mTHPC). Begge stoffer vil selektivt blive ophobet i cancer væv og vil derfor ved blå belysning udsende karakteristisk rødt lys. Dette røde lys, fluorescensen, kan detekteres med et kamera, og vil derved danne et billede af hvor der er cancer og hvor vævet er raskt.

Det primære mål i denne afhandling har været at konstruere en sådan blå lyskilde som kan bruges klinisk. Der er derfor taget udgangspunkt i laser dioder, kendt fra CD-afspillere, dog i denne sammenhæng ca. 1500 gange kraftigere. Laser dioder er billige, mekanisk stabile og har høj energi effektivitet. Desværre findes der p.t. ikke laser dioder der afgiver nok lys i det blå bølgelængde område som skal bruges til at skabe fluorescens. Derfor er der brugt en ikke lineær krystal der konverterer det infrarøde lys (810 nm) til blåt lys (405 nm). Dette system er lavet i flere udgaver i løbet af projektet, for at opnå højest mulig kontinuerlig udgangseffekt (cw) samt at lave meget korte lyspulser. Disse korte lyspulser skal bruges i situationer hvor der ønskes en måling mens der er kraftig baggrundsbelysning, som eksempelvis på en operationsstue. Ved at bruge meget korte lyspulser, kan man programmere kameraet der skal opfange fluorescensen til kun at åbne blænden i en meget kort periode efter den blå puls er udsendt. Denne teknik kaldes time-gating og forbedrer signal/baggrund forholdet.

I projektet lykkedes det at konstruere begge systemer, og de er afprøvet på patienter, med hud-cancer. Begge systemer viste tydeligt potentialet i teknikken. Derudover blev systemet brugt til at måle koncentrationen direkte af FosPeg i mus, ved hjælp af fluorescensen, hvilket er nyttigt at vide da man derved vil kunne monitorere PDT effekten under behandlingen.

List of Publications

This thesis is based on the following papers, which will be referred to by their roman numerals in the text.

I **Tunable high-power narrow-linewidth semiconductor laser based on an external-cavity tapered amplifier**
M. Chi, O. B. Jensen, J. Holm, C. Pedersen, P. E. Andersen, G. Erbert, B. Sumpf, and P. M. Petersen.
Opt. Express **13**, 10589 (2005).

II **Wavelength stabilization of extended-cavity tapered lasers with volume Bragg gratings**
G. Lucas-Leclin, D. Paboeuf, P. Georges, J. Holm, P. Andersen, B. Sumpf, and G. Erbert.
Appl. Phys. B **91**, 493-498 (2008).

III **Generation of more than 300 mW diffraction-limited light at 405 nm by second-harmonic generation of a tapered diode laser with external cavity feedback**
O. B. Jensen, J. Holm, B. Sumpf, G. Erbert, P. E. Andersen, and P. M. Petersen.
Proceedings of SPIE **6455**, 645503 (2007).

IV **High power 404 nm source based on second harmonic generation in PPKTP of a tapered external feedback diode laser**
J. H. Lundeman, O. B. Jensen, P. E. Andersen, S. Andersson-Engels, B. Sumpf, G. Erbert, and P. M. Petersen.
Opt. Expres **16**, 2486 (2008).

V **Threshold for strong thermal dephasing in periodically poled KTP in frequency doubling of an 808 nm high power tapered diode.**
J. H. Lundeman, O. B. Jensen, P. E. Andersen, and P. M. Petersen.
submitted to Appl. Phys. B.

VI **Pharmacokinetic study following systemic administration of a pegylated liposomal temoporn formulation using uorescence imaging techniques**
P. Svenmarker, J Axelsson, S. Grafe, J. H. Lundeman, H. Cheng, H. Xie, , N. Bendsoe, S. Svanberg, P. Andersen, K. Svanberg, and S. Andersson-Engels.
manuscript in preparation.

VII **Bleaching of the age-related colouration of human donor lenses using monochromatic laser light**
L. Kessel, L. Eskildsen, J. H. Lundeman, O. B. Jensen, and M. Larsen.
Submitted to: Experimental Eye Research.

Other related publications by the author:

Novel low-loss 3-element ring resonator for second-harmonic generation of 808nm into 404nm using periodically poled KTP
J. Holm, O. B. Jensen, B. Sumpf, G. Erbert, P. E. Andersen, and P. M. Petersen
Proceedings of SPIE **Volume 6455**, 645504 (2007).

Contents

Papers

Chapter 1

Introduction

Laser-induced fluorescence (LIF) is an exciting medical diagnostic tool, for use with detection and demarcation of cancer. The technique is based on measuring the light emitted from a drug injected into the patient, when the patient is irradiated with laser light of a specific wavelength. Unlike many other imaging techniques such computerized tomography (CT), positron-electron-tomography (PET) and x-rays, laser-induced fluorescence does not contain any radioactive substances to be injected. The drug used in LIF, called a photosensitizer, is non-toxic to the body and either metabolically broken down, or cleared from the body. The photosensitizer do, however, make the patient light sensitive for a certain period of time, which must be planned for in advance of the treatment or diagnostic procedure.

Laser-induced fluorescence is noninvasive, only the injection or topical application of the photosensitizer is invasive, the fluorescence detection and subsequent analysis is not. Furthermore no tissue is removed from the patient, as in a standard biopsy. An important fact, when testing for the possibility of cancer in e.g. the vocal folds, the intestine wall and in neurosurgery.

Because of the emitted fluorescence is originating only in cells having a large concentration of photosensitizer, additional information can be gained compared to the white light image. This can prevent healthy tissue from being removed, and also make sure that all of the tumor is removed including any metastases, that might not be visible in white light. The intention of the LIF system is that it could be used in real time during surgery, assisting the surgeon in the decision of tissue type.

Unfortunately there are also some drawbacks to the technique, first is the already mentioned light sensitivity. For some photosensitizers this condition can last up to three months. Newer photosensitizers have lowered this to only 24 hours, making it a lot more attractive diagnostic procedure. Another and more fundamental

issue is the fact that light cannot penetrate further than a few mm into the body, when illuminated from the outside. Hence detection of deeper lying tumors is not possible.

1.1 Available Light Sources

In order for the photosensitizer to fluoresce it needs to be in its first excited state. This is efficiently achieved by using a 405 nm laser source, that is absorbed by the photosensitizer. A subsequent relaxation includes fluorescence or an energy transfer to oxygen, creating the cytotoxic species that is responsible for cell death in photodynamic therapy (PDT). Lamps can be used as excitation sources around 405 nm, but they are very ineffective, due to their broad band nature, and omnidirectional radiation profiles. Laser sources are more interesting as they are spectrally narrow and directional.

Three laser systems have previously been used at the Lund University Medical Laser Centre for biomedical fluorescence diagnostics. A pulsed nitrogen laser operating at 337 nm, pumping a dye cell tuned to 405 nm output. The pulse energy are only a fraction of a μJ with a repetition rate of 20 Hz. This system cannot effectively be used for imaging due to the low repetition rate and pulse energy, but only for point measurements. The second system is a frequency doubled Alexandrite laser (385 nm) with a pulse energy around 1 mJ, which enough for extended area imaging. However, the system is big measuring about 1 m^3, weighing more than 200 kg and water cooled, making it a difficult system to operate, especially in a clinical setting. The newset system is a GaN laser diode used for point measurement, due to it inability to work in pulsed operation.

1.2 Specifications

The laser source to be developed had to be compact, semi-portable and easy to operate in a clinical setting. Wide bandgap laser diodes like GaN based 405 nm diodes, were not able to supply more than 60 mW (120 mW as of march 2008) and cannot be used in Q-switched mode due to the very short excited state lifetime. 810 nm diodes however, are routinely used for pumping YAG based lasers, and have with the new tapered design become available as prototypes with powers up to 2 W.

The target specifications were to create a suitable narrow linewidth pump source based on an external cavity configuration providing at least 1 W of cw power in an almost diffraction limited output beam. The pump then were to be frequency double providing at least 200 mW of cw output power in a diffraction limited beam at 405 nm. The pulse specifications were either in

sync with a standard PAL video (50 Hz field-interleaved) or an integer multiple of this base frequency, to provide better signal-to-noise or signal-to-background ratios by averaging. The duty cycle of the pulses must no be higher than 10^{-3} in order to be able to effectively suppress any operating room light from the fluorescence recordings.

1.3 Structure of the Thesis

The thesis is divided into 3 main parts, in accordance with the three phases during the project. Chapter 2 concerns diode lasers in general and the tapered amplifiers in particular. The basics of diode lasers are presented with the emphasis on the material system used in the experimental work on tapered amplifiers in Papers **I** and **II**. In chapter 3, the nonlinear interaction in crystals are presented, and the various optimizations that needs to be done in order to achieve a decent conversion efficiency. As the single pass efficiency is rather low at 808 nm, external resonators are used in chapter 4. The different design aspects are discussed relating to Papers **III**, **IV** and **V**. Finally in chapter 5 and 6, the concept of laser-induced fluorescence is introduced, with some experimental results of Paper **VI** presented in chapter 6.

Chapter 2

Diode Lasers

Following the first successful construction of a laser in 1960 by Maiman [1], it was suggested to use semiconductor material as gain media for lasers and already in 1962 lasing was reported in semiconductors [2–4]. The first devices were GaAs homojunction devices operated at cryogenic temperatures of liquid nitrogen, making them impractical for use in room temperatures applications. The diode lasers have since then improved in power output, wavelength coverage and lifetime. Diode lasers are found today in many applications and are an essential part of optical communication networks and entertainment systems using CD and DVD players. This chapter deals with the basic properties of diode lasers for use as continuous wave pump sources.

2.1 Emission and Absorption

In gas lasers and solid-state lasers, the energy levels are well-defined with a narrow linewidth. This is a result of weak interaction among the different molecules making up the laser medium. In semiconductors, on the other hand, the electronic states are not localized, and due to the Pauli exclusion principle the discrete states are broadened into bands of continuous energy states. The two main bands present in semiconductors, are the valence band and the higher energy conduction band. At temperature $T = 0$K the valence band is completely filled and the conductance band completely empty. The difference in energy between these two bands are called the band gap energy E_g, and typical values at room temperature are [5]: 0.7 eV in Germanium, 1.43 eV in GaAs and 3.4 eV in GaN. Electrons are populating both bands at finite temperatures, but for convenience it is common to express the dynamics of the valence band in terms of positively charged holes. The energy of an electron as a function of wavenumber is given as

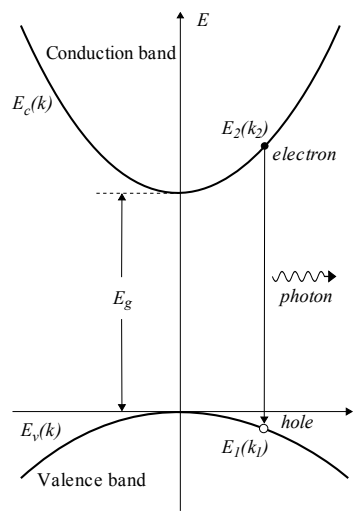

Figure 2.1. *The band structure for small $k-$vectors. The recombination of an electron from the conduction band and a hole in the valence band generates a photon. The momentum carried away by the photon ($\hbar k$) is negligible and hence transitions only occur for $k = k_2 = k_1$.*

$E(k) = \hbar^2 k^2 / (2m_0)$, where m_0 is the free-electron rest mass, and $\hbar = 1.055 \cdot 10^{-34}\text{J} \cdot \text{s}$ is Planck's constant. For small wavenumbers the energies in the conduction band E_c and valence band E_v will be given as

$$E_c = E_g + \frac{\hbar^2 k^2}{2m_e}, \qquad E_v = -\frac{\hbar^2 k^2}{2m_h} \tag{2.1}$$

The masses of the electrons m_e and holes m_h depends on the curvature of the band ($m = \hbar^2 \left(\partial^2 E / \partial k^2\right)^{-1}$), thereby making the effective masses dependent on the choice of semiconductor material [6]. For GaAs the effective masses are $m_v = 0.5m_0$ and $m_c = 0.068m_0$ for the valence band and conduction band, respectively. The band structure is shown schematically in Fig. 2.1

When the extrema of both bands are located at the same wavenumber, the bandgap is said to be direct (e.g. GaAs and InAs). This is due to the fact that a recombination between an electron from the conduction band and a hole from the valence band will result in emission of a photon with the energy $E_{ph} = E_2(k_2) - E_1(k_1)$. The relativistic momentum carried away by a photon is $\hbar k$, a very small amount, making transitions with $k_2 \neq k_1$ impossible. In indirect semiconductors (like Silicon and Germanium), the recombination process will need to be assisted by a phonon in order to conserve momentum. Because the number of phonons are low the recombination rate of such devices are very low making them unsuited for laser devices.

The possibility for an electron to occupy a state in the conduction band is given by the Fermi function

$$f(E,T) = \frac{1}{exp\left(\frac{E-E_f}{k_B T}\right) + 1} \tag{2.2}$$

with k_B being the Boltzmann constant and E_f is the Fermi-energy level. At $T = 0\text{K}$ the Fermi level is located exactly half-way between the valence band and the conduction band. Increasing the temperature or doping the semiconductor will change this energy level.

There are three different processes of electron-hole interaction important to lasing. First, the relaxation from the conductance band to the valence band by emission of a photon, a process called spontaneous emission. Second is the absorption process, in which a valence electron absorbs a photon of energy $E_{ph} > E_g$ and is excited up into the conduction band. Finally there is the process of stimulated emission, where an incident photon stimulates a conduction band electron to relax down to the valence band. This recombination with a hole will emit a photon, that will add coherently to the incident field. The three processes are shown schematically in Fig. 2.2.

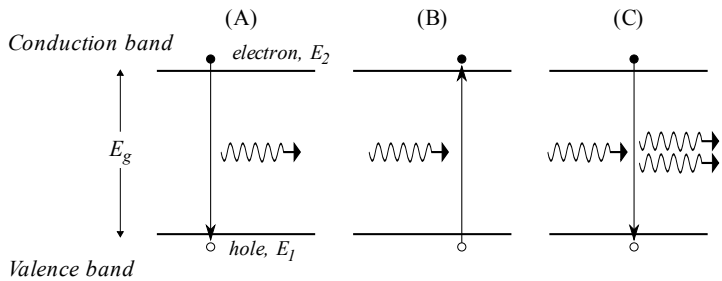

Figure 2.2. *The three different band to band transitions. A) spontaneous emission, B) absorption C) stimulated emission.*

In the spontaneous emission process the photon is emitted with random phase, polarization and direction, uncorrelated to any other optical field. The rate of spontaneous emission is directly proportional to the electron density and the hole density. The density of electrons is given as the density of states $D(E_2)$, times the probability of the states being occupied given by the Fermi function $f(E_2, T)$. Hence the spontaneous emission rate can be written as [7]

$$\mathcal{R}_{sp} = AD(E_2) f(E_2, T) D(E_1) [1 - f(E_1, T)]. \tag{2.3}$$

In the the stimulated absorption or just absorption process, an incident photon is exciting a valence electron into the conduction band, leaving behind a hole. The rate of stimulated emission depends on the densities of all three particles involved with the photon density $\rho(\hbar\omega)$

$$\mathcal{R}_{12} = B_{12}\rho(\hbar\omega) D(E_1) f(E_1, T) D(E_2) [1 - f(E_2, T)] \tag{2.4}$$

The last of the transitions is that of stimulated emission, where an incident photon stimulates a recombination of a conduction band electron and a valence band hole. The generated photon will enter the same quantum state as the incident stimulating photon, thereby increasing the power of the field. This is the transition responsible for lasing, whereas the spontaneous emission is the principle behind Light Emitting Diodes (LEDs). The stimulated emission also depends on the three densities like the stimulated absorption

$$\mathcal{R}_{21} = B_{21}\rho(\hbar\omega) D(E_2) f(E_2, T) D(E_1) [1 - f(E_1, T)] \tag{2.5}$$

The A, B_{12} and B_{21} coefficients are called Einstein coefficients and they relate as

$$B_{12} = B_{21} = B \qquad A = \frac{n^3}{\pi^2 \hbar^3 c^3} (\hbar\omega)^2 B \tag{2.6}$$

By dividing Eqs 2.3 and 2.5 and using the relationship in 2.6 it can be seen that the ratio between the spontaneous rate and the stimulated emission is given as

$$\frac{\mathcal{R}_{21}}{\mathcal{R}_{sp}} = \frac{B}{A}\rho\left(\hbar\omega\right) = \frac{\pi^2\hbar^3c^3}{n^3\left(\hbar\omega\right)^2}\rho\left(\hbar\omega\right) \tag{2.7}$$

It is an important requirement for lasing that this ratio is larger than unity.

2.1.1 Rate Equations

The rate equations are a coupled set of equations describing the phenomenological behaviour of the populations of holes and electrons in the laser. These equations couple the internal recombination mechanism with the external pump, and predict the expected electrical to optical performance. The rate of which the carrier concentration changes can be written as [7]

$$\frac{dN}{dt} = \mathcal{R}_{gen} - \mathcal{R}_{sp} - \mathcal{R}_{stim} - \mathcal{R}_{nr} \tag{2.8}$$

The change in the electron population is affected positively by the rate of generated electrons due to pumping, and negatively by the spontaneous emission, stimulated emission and the non-radiative decay due to phonon interaction. The generated rate of carriers depends on the injected current I divided by the electronic charge q, injected into the volume of the active layer. This volume is defined by the thickness d of the layer times the length L and width W of the injected region. Hence the generated rate can be written as

$$\mathcal{R}_{gen} = \frac{\eta_i I}{qdLW} = \frac{\eta_i j}{qd} \tag{2.9}$$

with $j = I/(LW)$ as the current density, and η_i as the fraction of the injected current that actually reaches the active region. The spontaneous recombination rate depends on the presence of an electron and a hole at the same time, and hence depends on the square of the carrier density

$$\mathcal{R}_{sp} = BN^2 \tag{2.10}$$

where B is the bimolecular recombination coefficient. The two main non radiative decay routes in a semiconductor is either via defects or through the intermediate use of third carrier, hence two terms contribute to the non-radiative rate

$$\mathcal{R}_{nr} = AN + CN^3 \tag{2.11}$$

The first term is the defect term, and the second is the Auger term. The $\mathcal{R}_{sp}$ and $\mathcal{R}_{nr}$ can be combined into a lifetime term as $\frac{N}{\tau}$, where

τ is the decay time for these processes, and can be experimentally verified by measuring the emission immediately after removing the pump current.

The stimulated rate is controlled by the gain coefficient g, the group velocity v_{gr} of the photons, and the number of photons

$$\mathcal{R}_{stim} = g v_{gr} N_{ph} \tag{2.12}$$

Combining the different terms, the final rate equation for the carriers is

$$\frac{dN}{dt} = \frac{\eta_i j}{qd} - \frac{N}{\tau} - g v_{gr} N_{ph} \tag{2.13}$$

The gain of the semiconductor medium is usually assumed to be linear for low current densities, with a logarithmic perturbation to account for saturation effects for high current densities. The gain is related to the carrier density in the linear approximation as

$$g\,(N) = a\,(N - N_{tr}) \tag{2.14}$$

where a is the gain constant and N_{tr} is the carrier density needed to make the lasing medium transparent. The gain constant can become very large on the order of 100 cm^{-1} compared to $10^{-2} - 10^{-3}$ cm^{-1} for a typical HeNe gas laser.

The rate equation for the photon density N_{ph} can analogously be written as

$$\frac{dN_{ph}}{dt} = g\Gamma v_{gr} N_{ph} + \Gamma \beta_{sp} \mathcal{R}_{sp} - \frac{N_{ph}}{\tau_{ph}} \tag{2.15}$$

These two equations can be used to derive the electrical and optical performance of laser diodes.

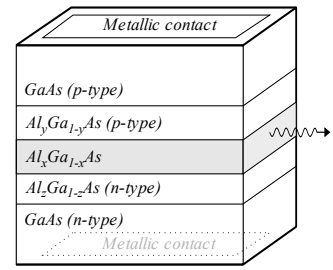

Figure 2.3. *The double heterostructure of a GaAs laser device. The active layer is the undoped AlGaAs center layer (grey). The surrounding layers have larger bandgap energies and hence will concentrate the injected electrons in the active region. Electrons are injected through the metalized contacts on top and bottom of the structure.*

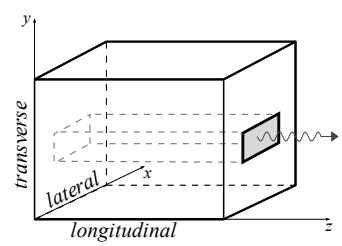

Figure 2.4. *The geometry of a typical laser structure. The directions and their relation to the orientation of the device are shown on the coordinate axes.*

2.2 Structure of Diode Lasers

Modern diode lasers consist of a p-doped layer and an n-doped layer separated by a thin undoped layer called the active layer. This layer is the p-n junction, that allows for recombination to take place and thereby the creation of light. If the surrounding $p-$ and $n-$type layers are of a different material than the active layer, the structure is called a heterostructure. The first diode laser implementations were all made in the same material and therefore called homo-structures, unlike today's lasers, that almost exclusively are manufactured as heterostructures. By using a heterostructure the bandgap can be made larger for the surrounding layers than for the active layer, resulting in the pumped electrons being confined to the central active layer of lowest energy. The outer layers (the cladding) also have lower index of refraction, hence they will confine the optical field to the active layer, increasing the effectiveness of the laser diode, as the overlap between the pumped region and

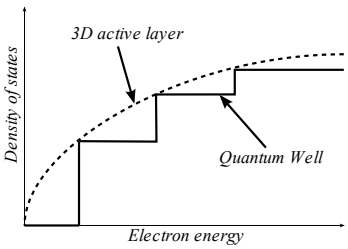

Figure 2.5. *Density of states function for the 3 dimensional active layer of a standard double heterostructure laser, compared with the discrete stepfunction of a 2 dimensional quantum well device.*

the optical field increases. A double heterostructure (DH) laser contains two such outer layers as shown in Fig. 2.3.

When a forward bias is applied to the diode, recombination will take place in the active layer or the junction. A steady supply of electrons from the current source will provide electrons for recombination. At a certain current density J_{th} the threshold for lasing is achieved, at which point the gain g exceeds the loss α. For laser oscillation to occur the cleaved end facets can be used directly, creating a simple Fabry-Perot standing wave resonator. In GaAs the index of $n = 3.4$ results in approximately 30% Fresnel reflection due to the large index difference. Both facets can be coated and usually one facet is coated with a High reflectivity (HR) coating with $R > 95\%$ and the output facet is coated for a target reflectivity of a few percent.

For semiconductor lasers it is customary to denote the directions as lateral (x), transverse (y) and longitudinal (z), as shown in Fig. 2.4. The lateral direction is the "width" of the waveguide, and usually larger than the transverse direction corresponding to the "height". The transverse direction is normal to the active layer, that are located in the $x - z$ plane. The longitudinal direction is along the length of active layer and coincides with the lasing direction.

2.3 Quantum Well Lasers

The active layer thickness is typically around 100 nm to 500 nm [8] in standard double heterostructure (DH) devices, resulting in a 3-dimensional density of states function given as

$$D_c(E) = 4\pi \left(\frac{2m_c}{h^2}\right)^{3/2} E^{1/2}. \tag{2.16}$$

If the active layer thickness is reduced to about 10 nm, the electronic states in the active layer will no longer form a continuum, but be discrete states. Such devices are called quantum well (QW) devices, in analogy to the potential well problem known from quantum mechanics. The reason for this quantization of the states can be understood from the fact that the electronic wave function is not localized but is extending over several lattice sites. In GaAs the Bohr radius $r_b = 0.53(m_0/m_c)\varepsilon/\varepsilon_0 = 8.6$nm [6] with $m_c = 0.068m_0$ and $\varepsilon = 11\varepsilon_0$. The lattice spacing in GaAs is only 0.562 nm [8], resulting in a spread out of the wave function. Figure 2.5 shows the density of states for the two different geometries. Quantum well lasers have a lower threshold current than DH lasers, due to their smaller active region [7]. More importantly is the ability to apply strain to the thin QW layer, either in form of compression or tension. The strain splits the bandstructure, and thereby changes the fundamental parameters of the material.

Hence the gain band can be altered by applying strain [9], and the threshold current is lowered for compressive strain and increased for tensile strain [8].

The tapered structures used in the experimental work, are all single quantum well structures. Multi quantum well structures are more common as this will increase the overlap and thereby the modal gain, but it is important in tapered lasers to avoid filamentation to maintain the spatial beam quality [10].

2.4 Light Output

The optical output power as a function of the current density j is divided into three regimes; below threshold for stimulated emission, the linear gain regime and the saturation regime. Below threshold the output power is dominated by amplified spontaneous emission (ASE) and is incoherent and spectrally very broad. This is the output seen from Light Emitting Diodes (LEDs).

Above threshold the light generation is linear with an increase in carrier density, and thereby supplied current. The lasing condition is met when the overall gain is larger than the losses of the optical mode. The fraction of the optical mode that overlaps with the gain region are denoted by an overlap parameter Γ. The part of the optical mode that propagates outside of the active layer, will not experience gain but intrinsic material absorption α_i. The effective gain or modal gain g_{modal} will then be given as $g_{modal} = \Gamma g > \alpha_i$, a condition that must be met in order for lasing to occur.

The mirror losses α_m must also be taken into account when the lasing condition is to be found. By using the reflectivities of the two end mirrors R_1 and R_2 and the length L of the device the lasing condition for the device is given as

$$\Gamma g_{th} = \alpha_i + \frac{1}{2L} ln\left(\frac{1}{R_1 R_2}\right) = \alpha_i + \alpha_m \qquad (2.17)$$

where g_{th} is the threshold gain, of the device. The main difference between transparency and threshold is that the mirror losses are taken into account when calculating the threshold condition, whereas the transparency condition is only concerning the material properties of gain g and absorption α_i.

When the current is increased to the threshold current the stimulated emission starts to amplify the ASE field (or an injected field), for those frequencies that are above transparency. Further increase in the current will increase the amplification of these modes, and due to mode competition the frequency spectrum will narrow considearbly, as the gain is not equal in magnitude for all wavelengths. An experimental plot of the power-current characteristics of the tapered diode laser used as pump source in Paper **V**

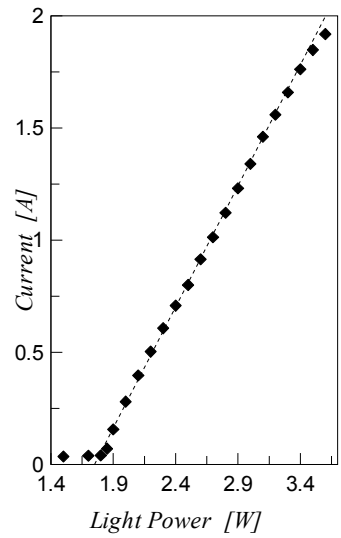

Figure 2.6. *The laser output in Watt, as a function of the supplied current, for the tapered device used in Papers **IV-VI**. The saturation has not been experimentally investigated, as such measurements contains the risk of destroying the device. The dashed line is a linear fit showing the three regimes of operation.*

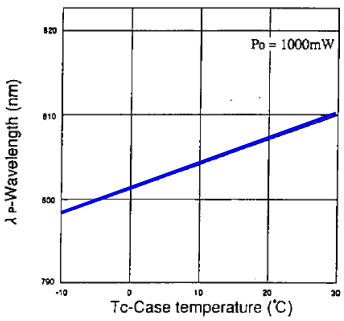

Figure 2.7. *The peak wavelength λ_p as function of temperature, for a commercial 808 nm high power diode (Sony corp. SLD323V).*

is shown in Fig. 2.6. Below threshold (1.85 A) the power output is negligible, changing into a linear dependence on injected current above threshold. A slight saturation can be observed at large injected currents. This device was routinely operated at 3A, well below saturation.

For Fabry-Perot devices, the change in photons in the oscillating field is described by Eq. 2.15. Two main contributions are depleting the photon population; re-absorption in the material and coupling out of the resonator at the output mirror(s)

$$\frac{dN_{ph}}{dt} = -\left(\alpha_i + \alpha_m\right) v_{gr} N_{ph} \tag{2.18}$$

with α_i as the internal material absorption and α_m the mirror loss. v_{gr} is the group velocity of the photons in the medium and hence contains the index of refraction. The total output power is then given as the rate of photons leaking through the output mirror times the photon mode volume and their energy [7]

$$P = \alpha_m v_{gr} N_{ph} \hbar\omega \frac{LWd}{\Gamma} \tag{2.19}$$

By using the fact that the photon density can be written as a function of the current density as

$$N_{ph} = \eta_i \frac{1}{q d v_{gr} g_{th}} \left(j - j_{th}\right) \tag{2.20}$$

and inserting into 2.19 the result is while converting current densities to currents

$$P = \eta_i \frac{\alpha_m}{\Gamma g_{th}} \frac{\hbar\omega}{q} \left(I - I_{th}\right). \tag{2.21}$$

By using the laser threshold condition 2.18 we can finally write P as

$$P = \eta_i \frac{\alpha_m}{\alpha_i + \alpha_m} \frac{\hbar\omega}{q} \left(I - I_{th}\right) = \eta_d \frac{\hbar\omega}{q} \left(I - I_{th}\right) \tag{2.22}$$

where the differential quantum efficiency η_d has been introduced. The quantum efficiency describes the effectiveness of the device in converting electric energy from the current source into photons. It is defined as

$$\eta_d = \frac{q}{\hbar\omega} \frac{dP}{dI}. \tag{2.23}$$

From Eq. 2.19 it can be seen that the power derivative regarding length is constant, resulting in a linear increase in power through the device. This is different from tapered amplifiers as discussed later.

From the rate equations it can be deduced that the carrier density as a function of current density is rising fast below threshold,

but once threshold is reached the carrier density gets clamped to a constant value. This is due to the fact that all "extra" carriers that are introduced into the device after reaching transparency, are effectively just increasing the gain and thereby adding to the stimulated field.

The gain bandwidth of semiconductors are typically tens of nanometers wide [9], but the gain peak is depending on temperature of the junction [7]. The tuning rate for GaAs is typically around 0.3nm/K as can be seen in Fig. 2.7.

The threshold current density j_{th} is depending on temperature T as

$$j_{th} = j_0 exp\left(\frac{T}{T_0}\right) \tag{2.24}$$

The result is that devices operated at low temperatures offer larger output powers for the same supplied current, than when operated at elevated temperatures. This is a very important aspect when designing the laser mount and cooling system.

2.5 Field Confinement

In order to avoid lasing in other than the longitudinal direction, the optical mode must be confined in both the lateral and the transverse directions. Different mechanisms provide the confinement in the lateral and transverse directions, and they are discussed independently in the following.

2.5.1 Transverse Confinement

In order to have an output beam consisting of only a single spatial mode, it is necessary to restrict the dimensions of the embedded waveguide. In order to do that, it has been found that the transverse dimension of the waveguide should be about 1λ [7]. The surrounding p and n type material of the active layer, provides an index contrast that will confine the optical field in the transverse direction. In Fig. 2.8 this effect is schematically shown. The figure is not to scale regarding the optical mode and the active layer thickness. The typical layer thickness is 100-500 nm, and hence will overlap 10-50 % of the optical mode. In quantum well structures this overlap is reduced to a few percent. The refractive index contrast is what keeps the optical mode confined to the active layer, however, this effect will not confine the carriers. This was one of the major problems with the first experimental homojunction structures, which required a very high current density in order to achieve amplification. However, by using another material with a larger bandgap than the active layer, the carriers will seek to the point with the lowest energy, which is the part with lowest bandgap, see Eq. 2.1. Hence the carriers will be confined to the

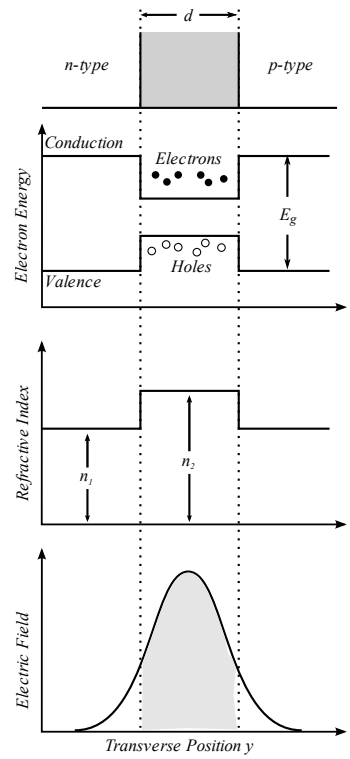

Figure 2.8. *The changes in bandgap and index around the active layer in a p-n junction. The narrowing of the bandgap combined with the increasing index is confining both the carriers and the optical field. The overlap of the optical field with the carriers are shown at the bottom.*

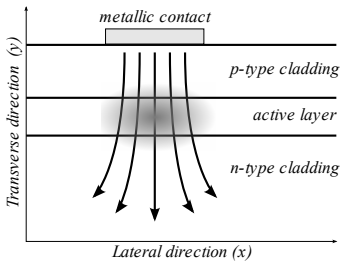

Figure 2.9. *The effect of lateral confinement due to gain-guiding. Carriers are only injected in the region defined by the narrow metallic strip. The optical field will only experience gain in this region.*

same physical space as the optical mode. In this way the threshold current is lowered as only the active layer and hence the optical mode, needs to be inverted. For lasers operating at around 800 nm, the waveguide thickness is usually 1 micron in height, this is somewhat larger than the 1λ size, however the loss for the higher order modes, are very large, as only the center part of the mode is amplified, thereby suppressing all but the lowest order fundamental mode. Recent devices has tried to expand the transverse dimension of the waveguide up to 4 μm, calling it a super large optical cavity (SLOC) [11]. This increased waveguide thickness reduces the divergence angle for the output beam, making it easier to collimate, and to effectively couple into the semiconductor for feedback or injection purposes. When increasing the size of cladding layers, the optical mode will increase in size, reducing the overlap with the active region leading to an increased threshold current.

2.5.2 Lateral Confinement

Gain Guiding

In order to confine the optical field in the lateral direction of the waveguide, two different techniques are used: gain guiding and index guiding. The simplest way to achieve confinement is to use an effect called gain-guiding. When carriers are injected into the device, they will travel directly from the top electrode to the bottom electrode as sketched in Fig. 2.9. If the metallic contact is shaped as a thin stripe there will only be injected carriers in this narrow region. Hence inversion can only take place directly beneath the electrode, thereby effectively establishing a region of lasing defined by the gain, hence called gain guiding. The refractive index of the semiconductor material is dependent on the local carrier density. This effect will spatially broaden the optical field towards the edges of the gain region (defined by the stripe) [9]. This antiguiding effect is described by using the anti-guiding parameter

$$\beta_c = -2k_0 \frac{\Delta n}{\Delta g} \tag{2.25}$$

where Δn is the change in refractive index when the gain has changed Δg and k_0 is the vacuum wave-vector. The parameter β_c is also called the linewidth broadening factor [12] because it results in a broadening of the intrinsic linewidth of a semiconductor laser. The anti-guiding parameter is dependent on the injected current, but is generally having values in the range 1.5-3 for GaAlAs lasers [13]. The change in the local index of refraction due to the carrier density is given as [12]

$$\Delta n = -\frac{\beta_c}{2k_0}\Delta g + i\frac{\Delta g}{2k_0} \tag{2.26}$$

The anti-guiding effects broadens the field spatially and leads to self-focusing, resulting in filamentation in devices with a width larger than approximately 6 μm [14]. Spatial hole burning arises in such devices due to areas of large stimulated emission, resulting in a decrease in carrier concentration, and hence an increase in the index will result.

Because the confined region changes with pump level, the lateral mode will also depend on the pumping. This generally results in poor lateral mode control, and makes such devices difficult to operate.

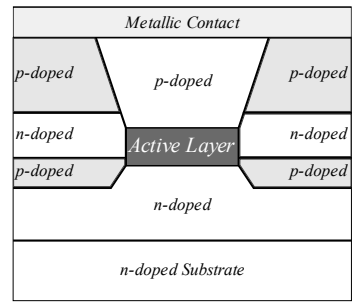

Figure 2.10. *Cross section of an index guided structure. The extra layers that make up the lateral cladding requires etching and regrowth of the wafer. Such devices are called buried heterostructures, due to the p-n-p layers. Adapted from [7]*

Index Guiding

An index guided structure, as shown in Fig. 2.10, contains an embedded part of lower index that surrounds the waveguide containing the active layer. This index step will confine the optical field just as the transverse confinement does through total internal reflection. The manufacturing of such structures, are very complicated compared to the gain guided devices, as it requires etching and regrowth of the low index regions. Single mode diodes usually employ index guiding structures in order to optimize their spatial properties, whereas high power devices tend to be gain guided. Index guided lasers do not suffer from the problems with poor lateral mode control that the gain guided devices inherently posses, and is therefore easier to couple into e.g. transmission fibers in optical networks.

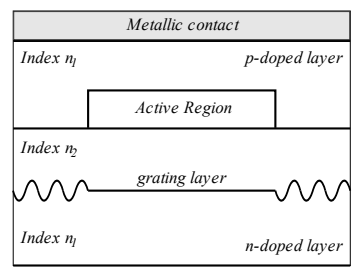

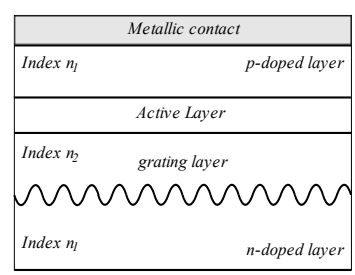

Figure 2.11. *The structure of the embedded grating in DBR laser (top) and a DFB laser (bottom). The difference in index $n_1 - n_2$ of the layers provide the periodic perturbation needed for the wavelength selective reflection to work.*

2.5.3 Longitudinal Mode Selectivity

The longitudinal length of single mode diode lasers is typically from 0.5 mm to 1 mm and hence will support a huge number of different longitudinal modes. Adjacent modes are separated by $c/2Ln$, where L is the length of the device, and n is the effective refractive index. Every mode have a different energy and frequency, and therefore will make the output spectrum of a simple Fabry-Perot laser quite wide. A wavelength span of more then 0.2 nm is typical.

For some applications the multi longitudinal mode nature of a diode laser is unwanted, and a lot of work has been done in order to narrow the spectrum as much as possible [15–18].

The various kind of mode selectivity generally work on the principle of inducing unequal losses for the modes in the gain band of the laser. Through mode competition the mode with the lowest loss will be amplified the most, and if the power ratio to the side modes is large enough, it will essentially be the only mode present in the device. This parameter is called side mode suppression ratio SMSR, and is typically 20 dB or larger for high power single frequency devices. When only a single frequency is present in the

output beam the diode laser is called a single frequency laser, and hence will automatically be single moded.

Different mode selective elements can be used, that decrease the number of lasing modes in the device. It is possible to embed a grating in the cladding layers below the active layer, that will work as a high order Bragg grating, and hence will only reflect a small range of frequencies [19, 20]. Such lasers are called distributed feedback lasers (DFB) and are very common in telecom applications [9]. If the Bragg grating is only placed at the end of the waveguide, they can be treated as wavelength dependent mirrors in a Fabry-Perot laser, a setup usually called Distributed Bragg Reflector (DBR).

Another possibility is to use an external diffraction grating, for the spectral selectivity. By fabricating a Bragg grating in a fiber pigtail, and placing it at the back facet, good wavelength stability can be achieved [21–23]. A modification of this process is to use a volume Bragg grating (VBG) that are manufactured in bulk glass. These can be made with large apertures, and hence used with broad area lasers or bars [24]. Both Bragg gratings suffer from the inability to tune the wavelength, except by changing the temperature of the grating itself. Although in some systems this might be a welcomed property, if exact wavelength stability in a large operating temperature range is needed. The VBG feedback mechanism was explored in Paper **II**.

It is also possible to extended the laser cavity by applying an anti-reflection coating to one of the facets, and use a reflector external to the laser in order to start the oscillations. Such setups are called external cavity designs, and provide a lot of flexibility, in choice and placement of components. However, external cavity designs suffer from one major drawback, they are no longer monolithic, single-piece devices. This makes them more difficult to handle, operate, setup, and maintain.

One of the external cavity designs, that have been explored is the use of a diffraction grating in place of a mirror. The grating will spatially separate the input beam dependent on wavelength. Hence by rotating the grating and using the very small aperture of the laser diode as a slit, a very strong frequency selectivity can be obtained. If the back facet is HR coated, the grating must use the front facet for coupling between the laser cavity and the external cavity. The back facet can be used for the feedback if a sufficient AR coating can be applied and the laser mount allows for access to the back facet.

The simplest setup is the Littrow configuration, in which a blazed 1st order grating is used. The grating is placed such that the 1st order dispersion is reflected directly back into the laser. If used on the back facet (Fig. 2.12A) the 0th order reflection is not used. A small tilt of the grating will change the wavelength that is coupled back into the laser, but will also change the angle of

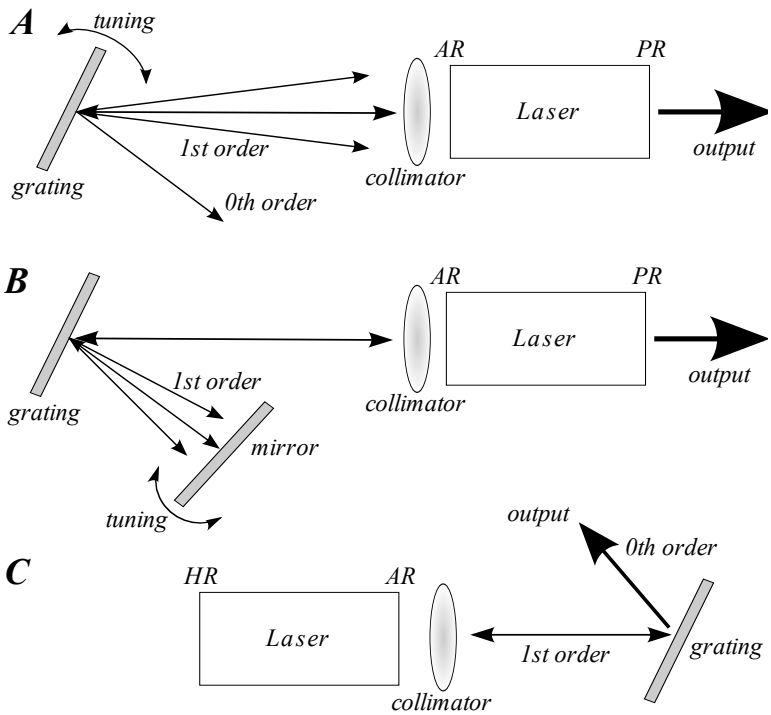

Figure 2.12. *Three different kinds of grating feedback using external cavities. A) Littrow configuration on back facet. B) Littman configuration on back facet (double pass on grating) C) Littrow on front facet, with 0th order as output.*

the directly reflected zero order beam. If used on the front facet as shown in Fig. 2.12C, the output beam direction will therefore change with the wavelength tuning. The Littrow configuration on the back facet is what was used in the setup described in Paper **I**, and used for frequency doubling in Papers **IV** and **V**.

The Littman configuration [25] (Fig. 2.12 part B) consists of a grating like the Littrow setup, but the 1st order is not reflected directly back into the laser. Instead it is directed to a mirror, that will retroreflect the beam for another dispersion pass at the grating. Because two passes are made on the grating the spectral selectivity is better compared to the Littrow configuration. Standard ruled grating have efficiencies of about 80 % around 800 nm and thus each pass of the grating will reduce the beam power with 20 %. The power coupled back into the laser from the Littman setup is therefore lower than in the Littrow setup.

A rather recent development is to use volume Bragg gratings (VBG) for external feedback. These are longitudinal gratings,

made in glass by periodically changing the index. They can be made with large apertures in the mm range compared to the fiber variety in the micron range. Volume Bragg gratings can be used both as reflectors or as transmitters, the latter property is useful when trying to make several distinct emitters emit at the same wavelength, like in a laser diode bar [24]. In the reflective mode it is used in the same way as the Littrow setup, except that the zero order is transmitted through the grating away from the laser. The thicker the grating, the narrower the reflection bandwidth, but the reflectivity decreases as well, so a compromise must be found. A VBG was used in Paper **II** to achieve single frequency oscillation in a tapered amplifier device. VBGs have a fixed wavelength reflection peak, that can only be changed through temperature tuning.

2.5.4 Spatial Output Mode

In single mode laser devices the spatial output mode is close to a fundamental Gaussian mode [6]. Because of the different sizes in exit aperture (typically 1 by 5 microns), the divergence are different for the two axes of the beam. For gain-guided lasers the output mode is also astigmatic (Fig. 2.13) as the gain guiding is curving the phase front in the lateral direction [27]. The astigmatism is measured as the distance between the facet and the virtual source point located behind the front facet. The ellipticity of the laser output beam is routinely removed by using an anamorphic prism pair or cylindrical lenses. Because the antiguiding effect in gain guided devices is current dependent, the amount of astigmatism in the lateral output mode changes with the supplied current. This makes them difficult to use in conditions of changing current, like on-off modulation. When used as pumps for second harmonic generation, it is important that the mode remains stable, in order for the subsequent mode matching optics to be positioned correctly for all pump powers.

2.6 Laser Diode Device Types

2.6.1 Single Mode Diode Lasers

The single mode laser devices are usually either made as a ridge waveguide laser, or as a buried heterostructure laser. The cross section of the device in Fig. 2.10 shows the latter geometry, whereas Fig. 2.14 shows the former. The buried heterostructure is capable of confining carriers in the active region, the photon field by index guiding and the current thereby maximizing the interaction. The ridge waveguide is easier to manufacture, but do not confine the carriers, only the photons and the injected current. Both of these geometries are routinely produced for single mode output. The stripe laser is the gain guided version, in which the stripe is nar-

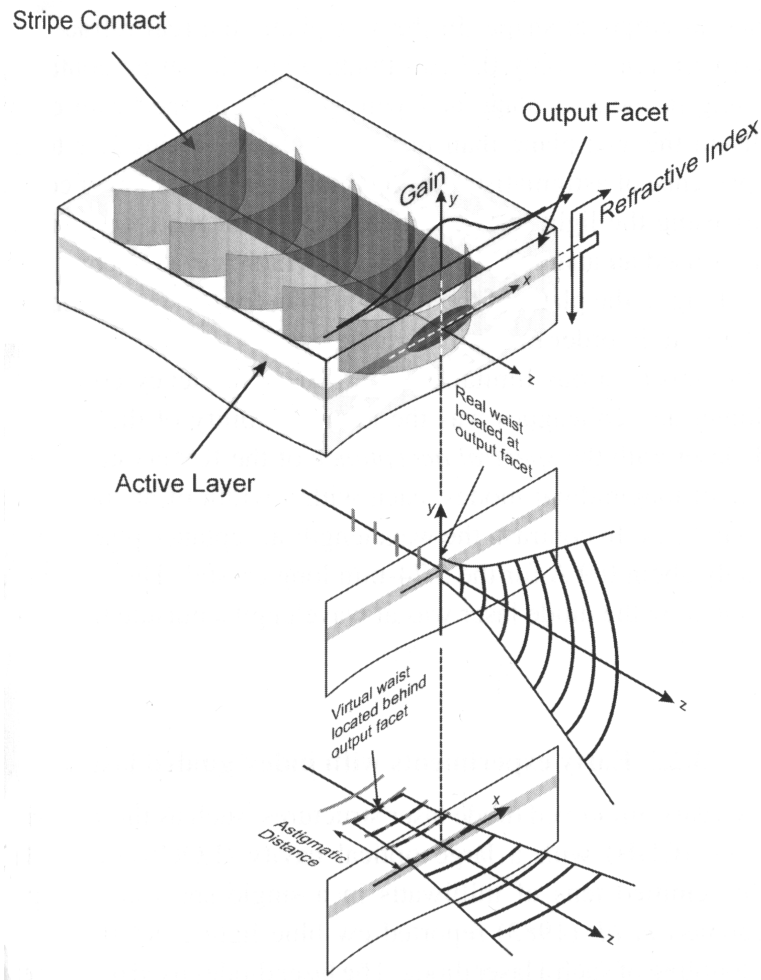

Figure 2.13. *The curved phasefronts gives rise to astigmatism in a gain-guided laser. From [26]*

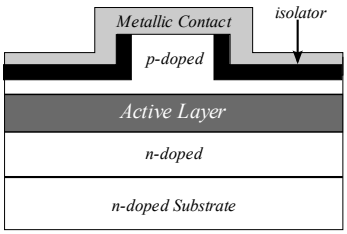

Figure 2.14. *The Ridge waveguide device structure. Another index guided structure, but unlike the buried heterostructure it does not have carrier confinement, only photon and current confinement.*

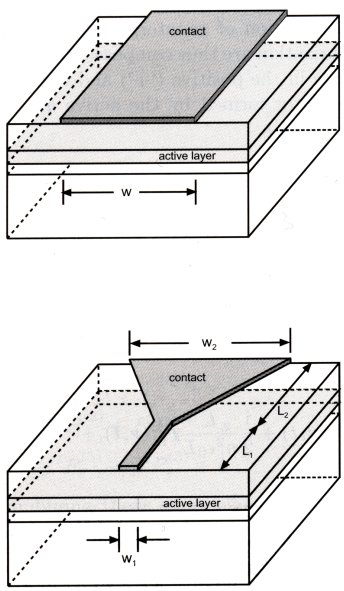

Figure 2.15. *On top the broad area laser geometry, featuring a very wide stripe width. Below the tapered device, showing the single-moded structure and the tapered amplifier.*

row enough to only allow a single mode to propagate in the gain guided active region. Single mode laser are only available up to about 200 mW in the 800 nm range, due to catastrophic optical damage (COD), occurring at the facet mirrors [28, 29]. The rather modest power compared to a standard light bulb, must all exit the facet within the small aperture of approximately 1 micron by 3 micron. This results in a huge intensity, that will heat the surface layer. This heating will increase the index of the semiconductor material resulting in a thermal lens that will self focus the beam, resulting in an even higher intensity. Hence the process of COD is very fast, and devastating to the facet. In order to increase the output power of diode lasers several different approaches have been tried, some of which will be described in the following.

2.6.2 Broad Area Lasers

A simple way to increase the power output without increasing the local intensity on the facet mirrors is to make the waveguide broader, thus creating the broad area laser (BAL). The aperture defined by the stripe width can be several hundred microns wide, extending into the mm range. When the width of the stripe defining the gain guided region is larger than 6 μm [14] the laser is no longer single moded in the lateral direction. Hence for a typical BAL size of 200 μm, a large number of lateral modes are present. Because of the poor spatial coherence resulting in such a large number of modes, the devices are usually made as gain guided structures, as an index guiding structure would just make the manufacturing unnecessarily complicated. The large number of different modes also result in a wide output spectrum of a few nm and thereby in poor temporal coherence.

Broad area lasers suffer from a phenomenon called filamentation, which degrades the output characteristics [30]. The very large intensities inside the active region will deplete the carrier-density, thereby changing the index according with the lateral anti-guiding effect, Eq. 2.26. This results in a very fast dynamic within the laser, that continually changes the lasing modes. Several feedback mechanisms has been tried in order to narrow the output spectrum and enhance the spatial properties of the output, see e.g. [31].

2.6.3 Tapered Lasers & Amplifiers

The tapered geometry device consists of two devices fabricated on the same wafer to carefully integrate them. It is a MOPA (Master Oscillator Power Amplifier) design in which the master amplifier is a single-moded waveguide laser, followed by a tapered power amplifier section. A schematic is shown in Fig. 2.15 showing the tapered diode defining the tapered section, as a continuation of the single-moded section. It is only the lateral direction of

the laser device that is tapered, the transverse distance is of the same dimension both in the single-mode part and the tapered part. The taper angle is chosen to match the diffraction pattern of the fundamental spatial mode of the laser, as it propages from the ridge section [34]. The first implementations of the tapered design were amplifiers without a preceeding single mode section.

The tapered semiconductor structure was pioneered in the early 1990's [35]. The first implementations were amplifiers operating at 980 nm [36, 37] soon followed by a a laser structure also operating near 980 nm [38]. Although several suggestions were made earlier on trying to use tapered structures to increase the single mode output power, it was not until the material process needed was available [39] that a successful tapered device could be manufactured. In 1993 Waarts [32] succeeded in using a tapered amplifier structure operating at 980 nm, as a source for direct frequency doubling. They obtained 3.7 mW of second harmonic output power from a $KNbO_3$ crystal, that were temperature phase matched (see section 3.5) to the lasing wavelength of the laser. The laser used a DBR structure on each end of the ridge section (Fig. 2.16) in order to narrow the lasing spectrum. In 1994 Mehuys increased the power to 5 W at 952 nm [40] followed in 1995 by a single frequency version providing 1 W [41] using Bragg reflectors. In 1997 Goyal and coworkers used an external cavity configuration shown in Fig. 2.17a consisting of a grating and an etalon. This setup allowed for tuning of the laser wavelength, as the angle of incidence on the grating could be changed by rotation. A tuning range of 17 nm was observed, for this laser structure centered at 783 nm. Goyal noted that the effective bandwidth of the lasing spectrum was quite wide compared to the intrinsic linewidth of the setup, despite using an intracavity etalon, see Fig. 2.17b. The same behaviour was observed on the 808 nm samples used throughout this work, limiting the obtainable Finesse in the external cavities used for second harmonic generation. Feedback from fiber Bragg pigtail for providing the frequency selective feedback was later reported in 1998 [23], and in 2002 tapered lasers operating at 735 nm with 2 W ouput power were reported [42, 43]. The first amplifier results at 808 nm were published in Paper **I**, and laser devices with output power of 4.4 W and reliability data followed in 2006 [44–46].

A different characteristic about the tapered device compared to a ridge device is that the gain is not constant along the length of the tapered device. This can be understood as the total current is not the same at every cross section along the length of the device. The change in output power of the tapered diode can be found analogously to the Fabry-Perot single-mode device. Walpole [34] deduced the change in power as a function of radial distance r in

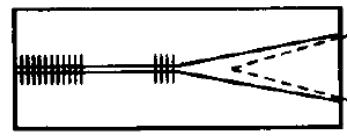

Figure 2.16. *The laser structure used by Waarts et al. [32] employing Bragg reflectors at each end of the ridge section. 1 W output power at 980 mW was achieved, and the subsequent doubling in a $KNbO_3$ crystal resulted in 3.7 mW of 491 nm power.*

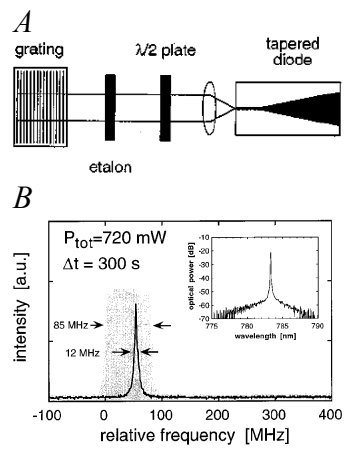

Figure 2.17. *A) The external laser used by Goyal [33] using a grating for feedback, and an etalon filter. The grating allowed for tuning the laser 17 nm around 783 nm. B) The output spectrum showing the center wavelength change with time. During a 300 s period, the laser line moved within the 85 MHz range indicated in grey.*

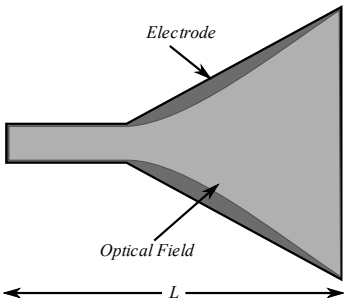

Figure 2.18. *The optical field do not expand as rapidly when starting to diverge in the tapered section, resulting in a lower efficiency in this area of the tapered device.*

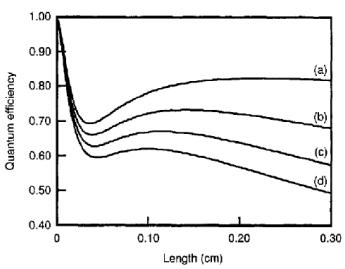

Figure 2.19. *Efficiency of a tapered device as function of length. The different internal absorption coefficients are (a) 1 cm^{-1}, (b) 3 cm^{-1}, (c) 5 cm^{-1}, (d) 7 cm^{-1}. From [34]*

cylindrical coordinates as

$$\frac{\partial P}{\partial r} = \left[\frac{\gamma_u}{1 + P/P_{sat}} - \alpha_i \right] P. \tag{2.27}$$

In the above γ_u is the unsaturated gain and P_{sat} is the saturation power. The derivative of the power is not constant as it is for single-mode lasers, but instead depends on r

$$P_{sat} = 2\phi r I_{sat} \tag{2.28}$$

where ϕ is the taper angle. But because the beam is allowed to expand as it propagates, shown in Fig. 2.18, the light intensity does not increase linearly with length, thereby reducing the spatial hole-burning tendency. A Gaussian beam is only diverging linearly in the far field, slower in the confocal range about a waist. Because the electrode is made geometrically triangular, the beam will not initially diverge as fast as the gain region, and hence the efficiency of the device will drop markedly in this area. As the beam starts to diverge faster, the efficiency will also increase. In Fig. 2.19 the efficiency of a tapered device with different internal losses is shown as a function of radial distance in the tapered section. The sharp drop off, due to the slower divergence of the optical field than the electrode, is followed by an increase as the beam is expanding faster and finally when gain saturation is reached the efficiency is slowly decreasing again.

Like in BAL's filamentation can build up in the tapered section, resulting in poor performance. Mikulla [10] has shown that if too large a modal gain is applied to the beam it will create spatial hole burns, and the output intensity profile (the near filed) will have large spatial oscillations. Lowering the gain the ideal flat-top profile, is found as can be seen in Fig. 2.21. The flat top near field spatial profile is desired as it results in a nice far field spatial profile. The far field can be obtained as the Fourier transform of the near field and a square function transforms into a sinc function, where about 84 % of the power is located between the first nulls in the far field profile [47]. Due to this low gain required the tapered devices are usually fabricated with only a single quantum well, to decrease the modal gain.

The tapered laser in general has its back facet HR coated in order to provide the lowest threshold current. This setup is monolithic and very robust, but does not work in single frequency mode, and only around the gain peak of the material. These lasers are usually on the order of 1 nm in spectral bandwidth, and thus unsuitable for nonlinear interactions.

In order to make the laser single frequency, it is necessary to provide a frequency selective feedback mechanism. This can be done through several means either internally via Bragg gratings (DBR) [41] or externally to the device by using a ruled grating like

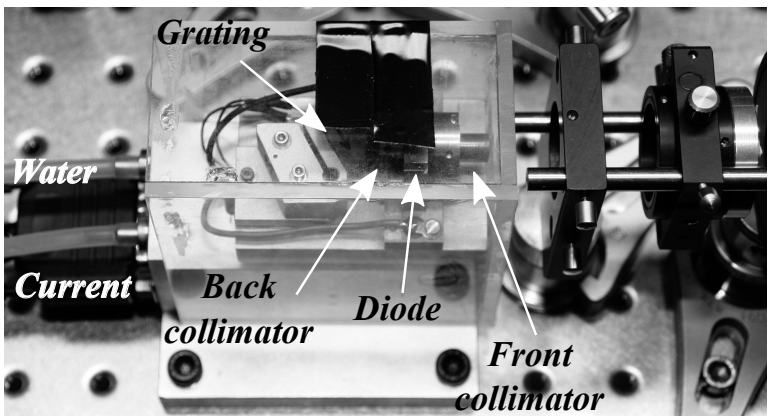

Figure 2.20. *A picture of one of the tapered amplifier setups. The front and back collimator lenses are attached directly to the laser mount, with the grating placed as close as possible to the back collimator. The small plexiglas (PMMA) housing helps reduce the effective linewidth of the laser.*

in Paper **I**, a Volume Bragg Grating(VBG) (Paper **II**) or phase conjugate feedback [48]. When used with an external feedback mechanism, it is important to have as low a back facet reflectivity as possible, to avoid coupled cavity effects. Diodes made in this way are just called tapered amplifiers. All these coupling schemes work on the back facet, as any feedback through the front facet will get amplified in the tapered section and will make the laser unstable [49]. To avoid reflected light baing coupled back into the laser, an optical isolator can be used. The isolator will only allow for light of a given polarization to pass through in one direction, thereby effectively shielding the laser.

By using a VBG for the spectral filtering the mechanical stability increases compared to the diffractive grating feedback, due to its smaller sensitivity to angular perturbations. The VBG can not be used to tune the wavelength of the amplifier, though, as it does not disperse the beam, like the planar grating does. The only way of changing the center reflection wavelength is to heat the entire grating, thereby changing the length of the material. The reflectivity of the grating is not as high as for gold diffraction grating, making it more difficult to saturate the amplifer. The one used in Paper **II** provided about 40 % reflection, compared to 85 % reflection of the ruled gold grating used in Paper **I**. A picture of the tapered diode laser used in Papers **IV**-**VII** is shown in Fig. 2.20.

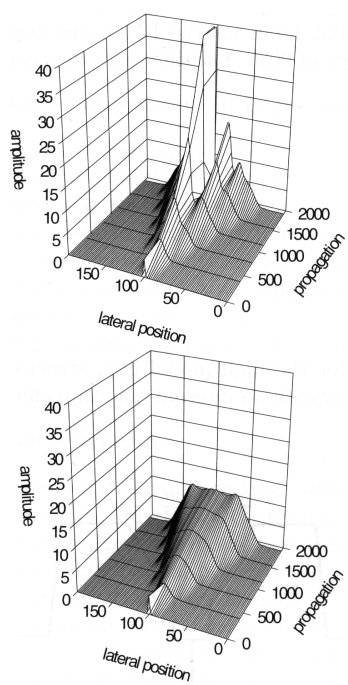

Figure 2.21. *The evolution of the field in a tapered amplifier, for two different modal gains. Large gain (top) results in filamentation and poor output profile. Low gain (bottom) produces a well defined flat-top beam. [10].*

2.7 Other Blue Laser Sources

Other laser systems for generating a high power 400 nm source exist. In this section a brief overview is presented, for ease of comparison, with the frequency doubled diode laser system, developed in this work.

2.7.1 Gallium-Nitride Diode Lasers

The Gallium-nitride (GaN) semiconductor lasers are a relatively new semiconductor laser system pioneered by Nakamura of Nichia Corporation in the late 1990's [50]. GaN is a material with a large bandgap of 3.4 eV, but do not as the GaAlAs system have an easily interchangeable partner for lattice matching and substrate growth. Despite these difficulties, Nichia has commercialized a 120 mW single-mode diode [51], with a threshold current of only 35 mA, and a slope efficiency of 1.4 W/A. Larger powers are generated at the expense of beam quality like for GaAs devices by increasing the width of the laser, resulting in a BAL design. No tapered laser design has been demonstrated yet in GaN, that might otherwise be able to produce higher output power while maintaining the excellent beam properties of the ridge laser. A GaN based system will be very rugged, easy to operate and portable.

2.7.2 Frequency Doubled DPSS systems

Diode pumped solid state (DPSS) lasers are a very mature technology, that can deliver high power and short pulses. Of particular interest for reaching 405 nm is the doubled Ti:Sapphire (TS) system. The TS crystal has a large absorption peak around 530 nm, that happens to coincide with the doubled wavelength of a 1064 nm YAG laser [52]. This fact is usually used in order to pump the TS optically. The emission spectrum is very broad ranging from 650 nm to 1100 nm, peaking at 800 nm. A large diode laser bar of 808 nm is used to pump the YAG crystal, generating a 1064 nm beam. This beam is then doubled to 532 nm beam, and used to pump the TS crystal that emits at the desired wavelength around 800 nm. This output can finally be frequency doubled to 404 nm. It is obvious that it will be more energy-efficient to double the output of the laser bar directly instead of using the two solid state laser systems. However, only the new tapered laser diodes provide the spectral and spatial purity needed for the second harmonic generation to be efficient.

2.7.3 Alexandrite Lasers

The alexandrite laser is a solid state laser were the active lasing medium is the alexandrite crystal ($BeAl_2O_4$). It has a strong emis-

sion line at 755 nm that is used in dermatology, due to its large penetration depth. The alexandrite are usually working in pulsed mode operation using a large lamp for optical pumping. This makes the system bulky, and expensive to operate. The 755 nm can be doubled to 378 nm in order to be useful for diagnostics, even then it is a bit off the absorption peak of 405nm for the photosensitizers used in this work.

Chapter 3

Second Harmonic Generation

As early as 1961 Franken [53] reported that second harmonic generation (SHG) had been achieved in quartz. This was basically the beginning of an experimental investigation into the fields of nonlinear optics, which now could be explored using lasers. This chapter deals with the fundamentals of second harmonic generation or frequency doubling in nonlinear crystals.

3.1 Basic Principles of SHG

The interaction between light and matter is described by the Maxwell equations and the constitutive equations [54]. They describe the evolution of the electric field $\mathbf{E}$ and the magnetic field $\mathbf{H}$

$$\nabla \times \mathbf{E} = -\frac{\partial \mathbf{B}}{\partial t} \tag{3.1}$$

$$\nabla \times \mathbf{H} = \mathbf{J} + \frac{\partial \mathbf{D}}{\partial t} \tag{3.2}$$

$$\nabla \cdot \mathbf{D} = \rho \tag{3.3}$$

$$\nabla \cdot \mathbf{B} = 0 \tag{3.4}$$

where $\mathbf{B}$ and $\mathbf{D}$ are the induced magnetic and electric fluxes, $\mathbf{J}$ is the current density and ρ is the charge density.

The constitutive equations gives the relation between the $\mathbf{E}$ and $\mathbf{D}$ fields, as well as $\mathbf{B}$ and $\mathbf{H}$

$$\mathbf{D} = \varepsilon_0 \mathbf{E} + \mathbf{P} \tag{3.5}$$

$$\mathbf{B} = \mu_0 \mathbf{H} + \mathbf{M} \tag{3.6}$$

$$\mathbf{J} = \sigma \mathbf{E} \tag{3.7}$$

where ε_0 and μ_0 are the vacuum permittivity and susceptibility, respectively, $\mathbf{P}$ is the induced polarization field, $\mathbf{M}$ the induced

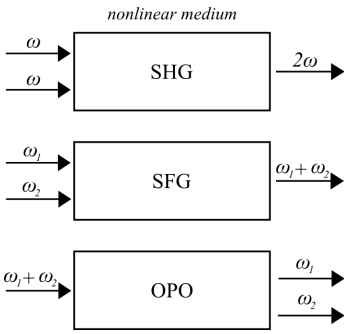

Figure 3.1. *Examples of 2nd order nonlinear processes. All SHG is seen to be the degenerate of the SFG process.*

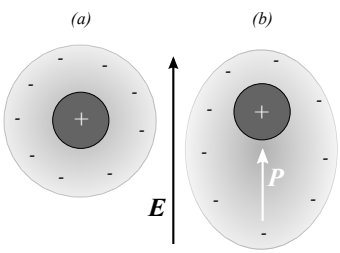

Figure 3.2. *A positive nucleus surrounded by a cloud of electrons. (a) No external field applied. (b) an external field* $\mathbf{E}$ *is applied, and the displacement of the electron cloud gives rise to a polarization* $\mathbf{P}$.

magnetization and σ the conductivity. As nonlinear crystal are nonmagnetic $\mathbf{M}$ can be set to zero. The wave equation for electromagnetic waves can be found by taking the curl of Eq. (3.1)

$$\nabla \times \nabla \times \mathbf{E} = -\mu_0 \frac{\partial}{\partial t} (\nabla \times \mathbf{H}) \tag{3.8}$$

were Eq. (3.6) has been used. By using the vector identity $\nabla \times \nabla \times \mathbf{E} = \nabla (\nabla \cdot \mathbf{E}) - \nabla^2 \mathbf{E}$ and inserting Eqs (3.2), (3.5) and (3.7) we obtain the wave equation

$$\nabla^2 \mathbf{E} = \mu_0 \sigma \frac{\partial \mathbf{E}}{\partial t} + \mu_0 \varepsilon_0 \frac{\partial^2 \mathbf{E}}{\partial t^2} + \mu_0 \frac{\partial^2 \mathbf{P}}{\partial t^2}. \tag{3.9}$$

This wave equation is valid for any time varying fields, and is the basis for the coupled wave equations.

3.2 The Induced Polarization

When an electromagnetic beam is incident on matter a polarization field will be generated. This can be understood in the classical picture of an atom consisting of a positive charge surrounded by a negative electron cloud. The incident $\mathbf{E}$ field will apply a force to the atom resulting in the electron cloud being displaced from it's equilibrium position. This displacement will generate a dipole moment and hence a polarization of the atom [55]. For low power time varying incident fields, the polarization field will be of the same frequency. Hence the response from the atom will be linear, in the sense that if the driving field is oscillating with a frequency ω_1 then the atom will respond with a polarization field at the same frequency. This linear response regime is in fact covering all the optical phenomens in our daily life, and we need the very high power densities from e.g. a laser in order to deviate from this linear response. However, for sufficiently high intensities the polarization will contain a nonlinear term [56]

$$\mathbf{P} = \mathbf{P_L} + \mathbf{P_{NL}} \tag{3.10}$$

The nonlinear polarization can be written as

$$\mathbf{P_{NL}} = \mathbf{P^{(2)}} + \mathbf{P^{(3)}} + \dots \tag{3.11}$$

resulting in a total polarization given as

$$\mathbf{P} = \varepsilon_0 \chi^{(1)} \mathbf{E} + \chi^{(2)} \mathbf{EE} + \chi^{(3)} \mathbf{EEE} + \dots \tag{3.12}$$

Here the $\chi^{(n)}$ is the n^{th} order susceptibility of the material, and is a tensor of rank $n+1$. The 1st order term $\chi^{(1)}$ gives rise to the linear behaviour of the response. That is the refractive index and absorption in the material. The $\chi^{(2)}$ process governs three-wave interactions like second harmonic generation (SHG), sum-frequency

generation (SFG) and parametric mixing. The $\chi^{(3)}$ process is responsible for e.g four-wave mixing, the Kerr-effect and stimulated Raman scattering.

As energy must be conserved in the interaction the incident and scattered electric field must be of the same frequency in the linear case. However, for higher orders of χ, coupling of energy into other frequencies are possible. In this section we will only discuss SHG, that is the degenerate SFG case where $\chi^{(2)} = \chi^{(2)}(-\omega_3 : \omega_1, \omega_2)$, with $\omega_1 = \omega_2 = \omega$ and the resulting wave $\omega_3 = 2\omega$.

$$d = \begin{bmatrix} 0 & 0 & 0 & 0 & d_{15} & 0 \\ 0 & 0 & 0 & d_{24} & 0 & 0 \\ d_{31} & d_{32} & d_{33} & 0 & 0 & 0 \end{bmatrix}$$

Figure 3.3. *The d tensor for the KTP crystal. It contains only 5 non-zero elements due to the high symmetry of the crystal.*

3.3 The d Tensor

The susceptibility $\chi^{(n)}$ is a tensor of rank $n+1$, and hence the i^{th} component of the polarization P_i is given as

$$P_i = \varepsilon_0 \chi^{(1)}_{ij} E_j + \varepsilon_0 D^{(2)} \chi^{(2)}_{ijk} E_j E_k + \varepsilon_0 D^{(3)} \chi^{(3)}_{ijkl} E_j E_k E_l + \dots \quad (3.13)$$

with summation over repeated indices. The degeneracy factors $D^{(n)}$ depends on the number of distinguishable beams in the process. For second order process the degeneracy factor is given as

$$D^{(2)} = \begin{cases} 1 & \text{for indistinguishable fields} \\ 2 & \text{for distinguishable fields} \end{cases} \quad (3.14)$$

It is customary to redefine $\chi^{(2)}$ into another tensor variable given as $d_{ijk} = \frac{1}{2}\chi^{(2)}_{ijk}$. This d-tensor is of 3rd rank tensor consisting of $3^3 = 27$ different elements. However, due to the fact that the interaction do not depend on the order in which the fields are written, e.g. $E_j E_k$ must equal $E_k E_j$, the 27 elements can be reduced to 18 independent elements. A new notation is used for these elements, which contracts the three indices ijk into only two indices mn. The conversion rules is as following

$i:$	x	y	z			
$m:$	1	2	3			
$jk:$	xx	yy	zz	$yz = zy$	$xz = zx$	$xy = yx$
$n:$	1	2	3	4	5	6

resulting in $d_{24} = d_{yyz} = d_{yzy}$ and in particular $d_{33} = d_{zzz}$ the latter being important in many nonlinear crystals. Other symmetries might exist in the material depending on the physical properties. Crystals in particular have a high degree of symmetry like mirror planes and rotations and therefore many of the tensor elements vanish [55, 56]. As an example the d-tensor for a KTP crystal is given in Fig. 3.3, showing that only 5 elements are nonzero. The tensor elements are usually described in the coordinate system of the natural optical axes in crystals. And as such is only valid for propagation along these axes. If another direction of propagation

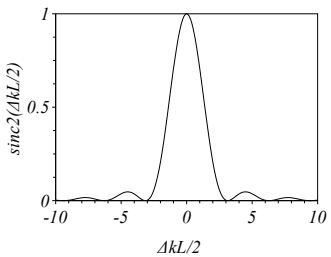

Figure 3.4. *The phasematching condition expressed by the sinc² function. Perfect phasematch is achieved when $\Delta k = 0$ independent of the length L of the crystal.*

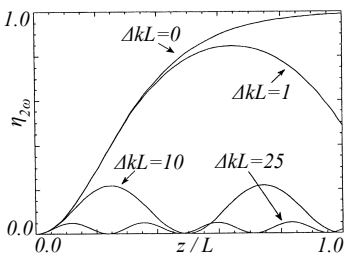

Figure 3.5. *The generated power will oscillate back to the pump beam if the phase matching is not perfect ($\Delta kL = 0$). Different values for ΔkL are plotted above. [56].*

is chosen the d-tensor needs to be translated into the new coordinate system, and the new element is therefore called the effective tensor element d_{eff}.

3.4 Coupled Wave Equations

In order to calculate the evolution of the incident field, the pump, and the generated second harmonic field, the coupled-wave equations are needed. They are derived from the wave equation Eq. 3.9 and the constitutive equations using the nonlinear polarization terms. For second harmonic generation the coupled-wave equations are given as [56, 57]

$$\frac{dA_{2\omega}}{dz} = iK\frac{2\omega}{n_{2\omega}c}d_{eff}A_{\omega}^{2}exp\left(i\Delta kz\right) \tag{3.15}$$

$$\frac{dA_{\omega}}{dz} = iK\frac{2\omega}{n_{\omega}c}d_{eff}A_{\omega}^{*}A_{2\omega}exp\left(-i\Delta kz\right) \tag{3.16}$$

In these equations it is assumed that the variation in the envelope of the field is negligible, during one optical period [55]

$$\left|k_i^2 A_i\right| \gg \left|k_i \frac{dA_i}{dz}\right| \gg \left|\frac{d^2 A_i}{dz^2}\right| \tag{3.17}$$

called the Slowly Varying Envelope Approximation (SVEA). This can be done by factoring out the rapid time and spatial variations of the $\mathbf{E}$ field as $\mathbf{E}\left(\mathbf{r},t\right) = \mathbf{A}\left(\mathbf{r},t\right)exp\left(i\mathbf{k}\cdot\mathbf{r}-\omega t\right)$, and only look at the envelope amplitude $\mathbf{A}$.

Usually an experimental setup will contain a length of nonlinear material, in which the 2nd order process will take place. Because of the very low absorption and high homogeneity in crystals, they are usually preferred as nonlinear materials, and hence we will assume that our material is a nonlinear crystal. In order to calculate the total power in the second harmonic beam exiting the crystal, Eq. 3.15 must be integrated over the crystal length L resulting in

$$I_{2\omega} = \frac{2\pi^2 d_{eff}^2}{n_{\omega}^2 n_{2\omega}\lambda_{2\omega}^2\varepsilon_0 c}I_{\omega}^2 L^2 \mathrm{sinc}^2\left(\frac{\Delta kL}{2}\right) \tag{3.18}$$

for plane waves as this derivation assumes. In Eq. 3.18 we have used the relation $I = \frac{1}{2c\mu_0}n\left|A\right|^2$ in order to express the result as an intensity instead of field amplitude. In the plane waves case the second harmonic intensity depends on the square of the length of the crystal, unlike the case where focused beams are used, in which only a linear dependence on length is found, see section 3.6.

The sinc-function is defined as [58] $\mathrm{sinc} = \frac{sinx}{x}$ and the term $\mathrm{sinc}^2\left(\frac{\Delta kL}{2}\right)$ in Eq. 3.18 is important as it states that the difference in k vector between the two waves must be zero for optimal conversion. The k vector is directly related to the index as $n_{\omega} = \frac{ck_{\omega}}{\omega}$

and thereby shows that the index of the crystal must be identical for the fundamental wave ω and the second harmonic wave 2ω. This condition is called phase matching and is due to material dispersion rarely occurring naturally in nonlinear crystals, but can be obtained through several techniques described in section 3.5. As it is easier to measure powers than intensities, it is common to reduce Eq. 3.18 to

$$P_{2\omega} = \eta P_{\omega}^2 \tag{3.19}$$

for systems where all values have been determined. The η parameter is called the single pass conversion efficiency or for non-resonant systems just the conversion efficiency, and is given in units of W^{-1}. These values are typically quoted in the literature instead of the d_{eff}-values as these are independent on the system setup.

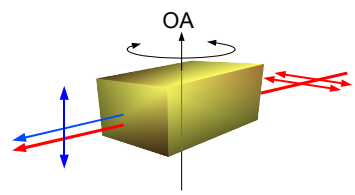

Figure 3.6. *Angle phase match. By rotating the crystal around the axis, the index changes for the SH beam. The effective tensor element d_{eff} changes likewise.*

3.5 Phase Matching

In order for the SHG to be truly efficient the two waves need to be in phase over as long a distance as possible when propagating in the crystal. This condition is called *phase matching*, and is needed in order for the generated SH wave to add constructively through the entire length of interaction. This can be seen if one tracks the generated SH power in the beginning of crystal through the crystal to the other end. If the newly generated power is not in phase with that generated in the beginning of the crystal, the newly generated contribution will not add constructively, and might in fact if the phase difference becomes larger than π subtract from the SH beam, thus reversing the energy flow from the SH beam back to the fundamental beam [57]. For that reason, the length of crystal the beams must travel in order to acquire a phase shift difference between them of π is called the *coherence length*. The coherence length is given as

$$L_c = \frac{\pi}{\Delta k} = \frac{\pi c}{2\omega_1 (n_1 - n_2)} \tag{3.20}$$

and is for most nonlinear crystals in the μm range. If no means for establishing phase matching is used, the SH power will oscillate spatially with a period of $2L_c$. Phase matching can be achieved in several ways of which the most common will be described here.

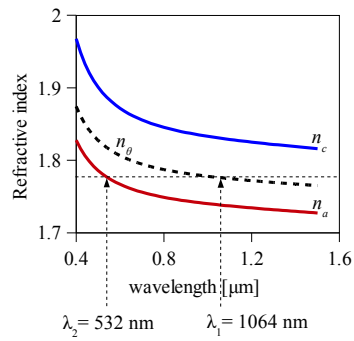

Figure 3.7. *The index of the a and c axes of KTP, together with the angle-tuned in-between n_θ index. Here illustrated for frequency doubling a Nd:YAG laser at 1064 nm. The calculation is based on Sellmeier equations from [59].*

3.5.1 Angle Phase Matching

In anisotropic materials the index of refraction is not a scalar quantity, but depends on the crystal axis. Uniaxial crystals have an ordinary index n_o which is independent of direction of propagation in the crystal, and an extraordinary index $n_e(\theta)$ that depends on the direction of propagation. Because $\chi^{(2)}$ is a tensor it is possible

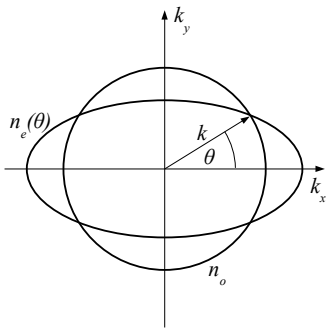

Figure 3.8. *Schematic of the change of index for the two orthogonal polarizations of the beam. The ordinary index is independent of direction (circle), whereas the extraordinary depends on direction (ellipse).*

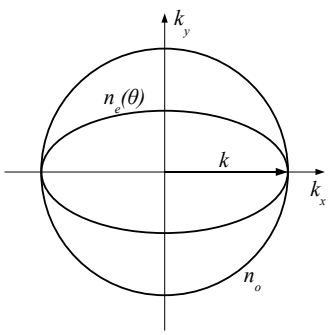

Figure 3.9. *Noncritical phase matching along one of the optic axes. No walk-off is occurring in this situation.*

to couple between orthogonal polarization states. Hence by propagating the fundamental beam polarized along the ordinary axis, it is possible for the second harmonic to be phase matched when propagating polarized along the extraordinary axis, resulting in orthogonal polarization states for the two beams.

Because of the index difference between the two polarizations, they also experience different permittivities. This changes the angle between the E and D vectors, resulting in a phenomenon known as walk-off. The result is that the energy (the Poynting vector $\mathbf{S}$) is no longer coinciding with the k vector - the propagation direction of the phasefronts. The result is that the two beams get spatially separated, and hence no interaction can take place. Worse is the fact that the beam changes spatial structure e.g. a Gaussian beam is no longer a Gaussian, which can be detrimental for the application of the second harmonic beam. For uniaxial crystal the walk-off angle ρ can be found from [60]

$$cos\rho = \frac{n_e^2 cos^2\theta + n_o^2 sin^2\theta}{(n_e^4 cos^2\theta + n_o^4 sin^2\theta)^{\frac{1}{2}}} \tag{3.21}$$

It is possible to define an effective length that is usable in a crystal with walk-off [61] called the aperture length

$$L_a = \frac{\sqrt{\pi} w_0}{\rho}. \tag{3.22}$$

As ρ is a material constant, the interaction length can be tailored by changing the beam waist w_0 in the crystal. The focusing however also affects the efficiency as described in section 3.6, and must be factored in when designing a system.

In Fig. 3.8 the index ellipsoid of a uniaxial crystal is shown. The circle represents the ordinary index that is constant for all directions of propagation in the crystal. The extraordinary index represented by the ellipse is not constant, and this allows for the phase matching. The intersections of these two loci are the directions in which phase matching can be achieved. Only a small perturbation of the k vector will result in a large change in index (distance between the loci), and thereby make the phase matching fail. The result is that the acceptance angle of the crystal is very small, and this type of phase matching is therefore termed *critical*.

3.5.2 Temperature Phase Matching

The problems with walk-off and small acceptance angles can be solved if the k vector can propagate along an optic axis in the crystal. This is, however, only possible for one wavelength, if possible at all. But due to the temperature dependence of the index and especially the difference in their derivatives in the different axes ($\frac{\partial n_i}{\partial T} \neq \frac{\partial n_j}{\partial T}$), it is possible in some cases to heat (or cool) the

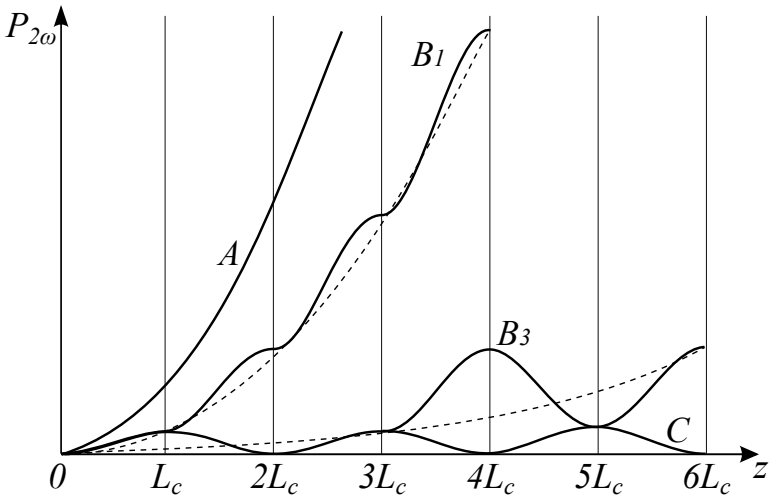

Figure 3.10. *Generation of second harmonic generation as a function of coherence lengths in periodically poled crystals. Line A is the ideal phase matched case as for birefringence phase matching. C is the case where no phase matching is established, and the power oscillates between the beams. B_1 and B_3 are the QPM cases of 1st and 3rd order, respectively, showing how the energy is fluctuating about a reduced efficiency compared to the perfect case. Adapted from [62]*

crystal and thereby achieve phase matching. This kind is called *non-critical* phase matching as rather large perturbations is needed for the phase matching to deteriorate.

3.5.3 Quasi Phase Matching

The largest tensor elements are usually of the type that requires the fundamental and second harmonic to propagate with the same state of polarization. However, as all materials have dispersion this situation cannot be phase matched. A very elegant solution to this problem is to change the sign of the d-tensor element for every coherence length in the crystal. In this way the phase difference accumulated during propagation over a coherence length cancel, hence this process is called *Quasi Phase Matching (QPM)*. There are several benefits to using QPM. First we can use the d_{33} tensor elements that are usually 5-10 times larger in materials like Lithium Niobate and KTP. Second we can propagate the beam along an optic axis and thereby achieve noncritical phase matching tolerances and no walk-off. Finally wavelengths not obtainable with angle phase matching can be reached.

The main idea of QPM is to invert the d-tensor after every coherence lengths. This has the effect of changing the phase of the generated field by π as can be seen from the coupled wave

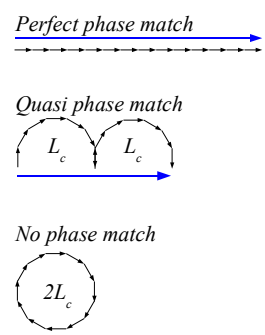

Figure 3.11. *Phasor diagrams for QPM compared to perfect and no phase match. Adapted from [26]*

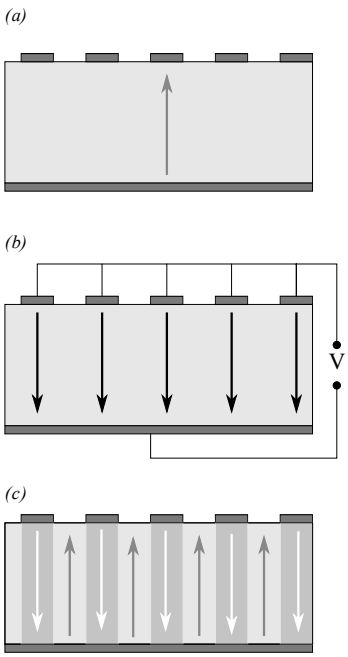

Figure 3.12. *The process of periodically poling the ferroelectric crystals. (a) electrodes are deposited on top and below the crystal (b) a high voltage is applied to the crystal, while heated. (c) the field has been changed after cooling down and removing the high voltage.*

equations Eq. 3.15. If the sign is not changed of the generated wave the power will just oscillate from one beam to the other for every $2L_c$ as can be seen as curve C in Fig. 3.10.

In order for quasi phase matching to work the acquired phase shift over one region of crystal must be an $n\pi + \pi/2$, where n just represents an integer, in other words the domain length must be of an odd number of coherence lengths. In such devices the effective nonlinearity tensor d_m can be written as

$$d_m = (2/m\pi)\, d_{eff} \quad \text{for } m \text{ odd.} \tag{3.23}$$

The lowest order of m is thus a first order modulation, for every L_c, and generally the domain length will be of length mL_c. In Eq. 3.23 it is assumed that a perfect modulation is done for every mL_c, however, this might not be the case, as the fabrication is difficult. A lower duty cycle than the optimum 50:50 will result in worse performance, and is thoroughly treated in [62].

Fabrication of QPM Structures

The concept of reversing the phase after one coherence length, was described by Armstrong et al. [57], who suggested to use a series of KDP crystals, but rotating every other by 180°. For many materials the coherence length is typically less than 5 μm for wavelengths below 1 μm, which makes this a very difficult task. Several early experimental attempts were made (e.g. [63–66]) but with limited success due to the difficulties of producing periodic structures on the micrometer scale.

Lithium Niobate, KTP and Lithium Tantalate (LT) are all ferroelectric materials. An important property of ferroelectrics are their ability to maintain an electric polarization in absence of an external applied field. These materials become unpolarized when heated to temperatures above the Curie temperature T_C. It is the crystal structure that allows for this freezing of the polarization, by the spatial arrangements of the conductive ions. This property is used when poling the crystals. The ions that produces the spontaneous polarization, can be moved in a desired direction by applying an external electric field. The crystal is lithographically patterned on the facet with a grating like structure using a conducting material, see Fig. 3.12. On the opposite side of the crystal another electrode is placed. When heating the crystal to T_C and applying the field, the polarization is induced in the crystal. By slowly cooling the crystal, while maintaining the applied field, the crystal will keep the polarization at room temperature. Because the grating pattern is periodic, and this process of storing a polarization in a material is called poling, these crystals are usually named periodically poled and abbreviated PP in front of the crystal name, e.g. PPKTP.

3.5.4 Phase Matching Tolerances

It is important to know how critical the different parameters are when designing a laser system based on a QPM crystal. That subject has been covered thoroughly by Fejer et al. [62] and a brief summary will be given here. We can rewrite Eq. 3.18 as

$$I_{2\omega} = I_{opt}\mathrm{sinc}^2\left(\frac{\Delta k\left(\zeta\right)L}{2}\right) \tag{3.24}$$

expressing the wavevector mismatch as a function of some parameter like length, temperature, angle, etc. If we Taylor expand the Δk around the value $\zeta = \zeta_0$ that provides optimum phasematching we get

$$\Delta k\left(\zeta\right) = \frac{\partial \Delta k}{\partial \zeta}\left(\zeta - \zeta_0\right) + \frac{1}{2}\frac{\partial^2 \Delta k}{\partial \zeta^2}\left(\zeta - \zeta_0\right)^2 + \cdots . \tag{3.25}$$

We are interested in the FWHM value of the sinc^2 term in Eq. 3.24. The sinc^2 function is 0.5 when its argument is 0.4429π. If we neglect the 2nd and higher order terms in the expansion, we find that the FWHM is given as [62]

$$\Delta\zeta = \frac{5.57}{L}\left(\frac{\partial \Delta k}{\partial \zeta}\right)^{-1} . \tag{3.26}$$

The wavelength bandwidth of a crystal is found to be

$$\Delta\lambda = \frac{0.4429\lambda}{L}\left[\frac{\partial n_1}{\partial \lambda} - \frac{1}{2}\frac{\partial n_2}{\partial \lambda} + \frac{n_2 - n_1}{\lambda}\right]^{-1} \tag{3.27}$$

and is seen to depend on the length of the crystal. The last term in the brackets $\frac{n_2 - n_1}{\lambda}$ are zero for birefringence phase matching, as the indices are equal in this case. The temperature bandwidth is also of importance for the system design, regarding the dimensioning of the oven holding the crystal. The temperature bandwidth is given as

$$\Delta T = \frac{0.4429\lambda}{L}\left[\frac{\partial n_{2\omega}}{\partial T} - \frac{\partial n_{\omega}}{\partial T} + \alpha\left(n_{2\omega} - n_{\omega}\right)\right]^{-1} \tag{3.28}$$

where $\alpha = \frac{1}{L}\frac{\partial L}{\partial T}$ is the coefficient of expansion for the material. As the pump source is generally a laser of high coherence, the wavelength bandwidth is less of a concern than the temperature bandwidth. For the PPKTP crystal used in Papers **IV** and **V** the theoretical temperature bandwidth is 0.37 K. The measured temperature bandwidth of the used PPKTP crystal was somewhat larger (0.44 K) than expected. This can be attributed to a nonoptimal duty cycle, and poling errors.

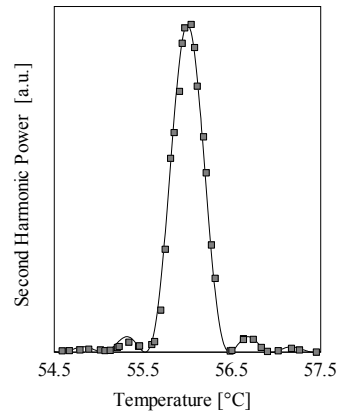

Figure 3.13. *Experimentally obtained temperature tuning of the PPKTP crystal used in Papers **IV** and **V**. The input is constant and the temperature has been varied. A sinc^2 function has been fitted to the measured datapoints (blue squares).*

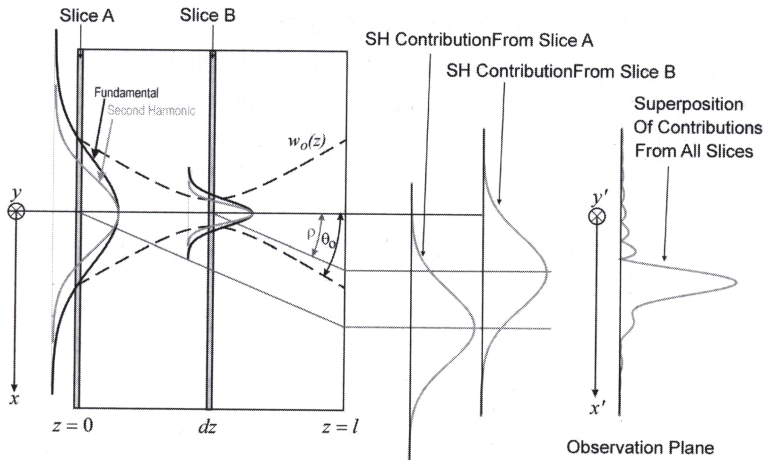

Figure 3.14. *For each thin slice dz the second harmonic is calculated, and then propagated out of the crystal, and into the far field. In the far field all of the contributions are integrated to yield the total spatial intensity. In the figure a very high value of B is used for demonstration, typical walk-off angles are some tens of miliradians. From [26]*

3.6 Beam Focusing

As the efficiency of the second order process depends on the intensity squared (Eq. 3.18), it is desirable to use the laser's ability to be focused to very small spotsizes, in order to maximise the efficiency of the nonlinear process. However, this will also make the beam diffract faster, thereby limiting the interaction length inside the crystal. A trade off between spotsize and interaction length must therefore be found. In the classic paper of Boyd and Kleinman [61] this problem was analyzed and the optimum position and focusing was found. The analysis is done by considering an incident laser beam with a Gaussian beam shape and a focus in the center of the crystal propagating in the z-direction (lab-frame). All the contributions to the generated beam from small slabs of dz in thickness are then propagated to the end of the crystal and into the far field, in order to calculate the total intensity generated. Several parameters are introduced in the analysis: the phase mismatch σ, the focal position μ in the crystal, the birefringence parameter B depending on the walk-off angle ρ, the focusing parameter ξ and the loss κ

$$B = \beta\xi^{\frac{1}{2}} = \rho\left(Lk_\omega\right)^{1/2}/2 \tag{3.29}$$

$$\xi = \frac{L}{b} = \frac{L\lambda}{2\pi w_0^2} \tag{3.30}$$

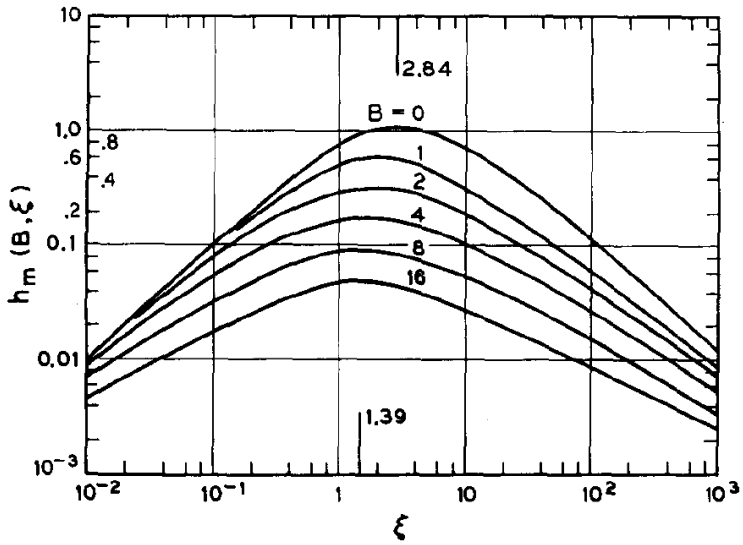

Figure 3.15. *Plot of the focusing function h_m versus beam focusing $\xi = L/b$ for different B values. From [61]*

here L is the crystal length and ρ given as Eq. 3.21. The b parameter is the confocal parameter of the Gaussian beam and equal to $2z_R$, with z_R being the Rayleigh length. The waist size of the Gaussian beam is here denoted w_0. From these five optimizable parameters a focusing function $h(\sigma_m, \beta, \kappa, \xi, \mu)$ is defined and is part of the general result of total generated SH power

$$P_{2\omega} = \frac{16\pi^2 d_{eff}^2}{\varepsilon_0 c \lambda_\omega^3 n_{2\omega} n_\omega} P_\omega^2 e^{-\alpha L} L h(\sigma_m, \beta, \kappa, \xi, \mu) \tag{3.31}$$

In case of negligible absorption the optimum position of the focus is in the center of the crystal, and hence $\kappa = \mu = 0$, which allows us to simplify h as $h(\sigma, \beta, 0, \xi, 0) = h(\sigma, B, \xi)$. The B parameter is given by the dispersion in the crystal and cannot be adjusted. This leaves the phase mismatch $\sigma = b\Delta k/2$ and the focusing to be optimized. The value that maximises h for fixed B and ξ can then be denoted σ_m and the corresponding focusing parameter $h_m(\sigma_m, B, \xi)$. The value of h_m is plotted in Fig. 3.15 as a function of focusing parameter. An important case is when $B = 0$ for non-critical phase matching, like in periodically poled crystals. The optimum value for $h_m = 1.068$ when the focusing is $\xi = L/b = 2.84$. In this case Eq. 3.31 reduces to

$$P_{2\omega} = 1.068 \frac{16\pi^2 d_{eff}^2}{\varepsilon_0 c \lambda_\omega^3 n_{2\omega} n_\omega} P_\omega^2 L \tag{3.32}$$

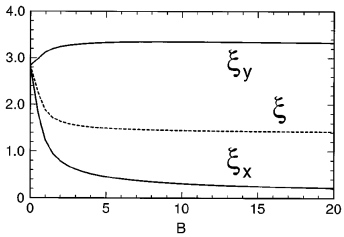

Figure 3.16. *The optimum focusing parameters as a function of the birefringence parameter. The critical (walk-off) direction is assumed to be in the x-direction. From [71].*

when absorption is negligible and in the case of optimum focusing.

As can be seen from Fig. 3.15 the optimization regarding the focusing parameter is not very critical. The h_m-parameter will only change by about 10% for focusing parametes in the range $1.52 < \xi < 5.3$ (for $B = 0$). This is the reason for the relatively high conversion efficiency of the 30 mm long PPKTP crystal used in Paper **IV**, although the beam was 4 times larger than the optimal size. The larger beam, however, allows for a lower temperature gradient in the crystal that otherwise would limit the conversion efficiency at high output powers, as reported in Paper **V**.

3.6.1 Elliptical Focusing

The theory presented in section 3.6 regarding optimal focusing of the pump beam is based on circular non-astigmatic beams. Circular beams are not always available, for instance in resonators or the direct output beams from laser diodes. For crystals with a high birefringence parameter B the use of an elliptical beam might in fact increase the conversion efficiency compared to the circular beam [67]. The reason for the increased efficiency is due to the walk-off experienced by the second harmonic beam. With elliptical focusing it is possible to use a tighter focus in the direction orthogonal to the walk-off plane, and hence increase the SHG conversion efficiency. In the walk-off plane a looser focus can be used, that will allow for a longer interaction length, due to the larger spatial overlap. The asymptotic forms of the generated second harmonic power was derived by Librecht and Simmons [68] based on the ellipticity $\alpha = w_x/w_y$ of the Gaussian beam. They define a new focusing parameter $\zeta = L/(\alpha k w_x^2)$ and then follow the same analysis as [69, 70] in order to calculate the generated second harmonic power. In the case of no walk-off, when non-critical phasematching is used, the asymptotic forms are given as

$$P_{2\omega} = K\frac{L^2}{\alpha w_x^2}P_\omega^2 \quad \text{for } \zeta << 1 \tag{3.33}$$

$$P_{2\omega} = K\pi^2\alpha k w_x^2 P_\omega^2 \quad \text{for } \zeta >> 1 \tag{3.34}$$

where

$$K = \frac{8\pi d_{eff}^2}{\varepsilon_0 c n_\omega^2 n_{2\omega}\lambda^2} \tag{3.35}$$

By splitting the focusing parameter in the two orthogonal directions of the beam ξ_x and ξ_y, the optimum values can be found as a function of the birefringence parameter [71, 72]. The analysis shows that in case of no birefringence the optimal focusing is circular as expected (see Fig. 3.16). An expected increase in conversion efficiency has been verified experimentally for elliptical beams in crystals with high birefringence [72].

3.6.2 Non Diffracting Beams

A non diffracting beam is a beam whose spatial profile does not change when propagating. The best known example is the Bessel Beam [73], so named as its intensity profile is a Bessel function. A simple question arises as to whether such a beam would in fact increase the overall conversion efficiency, as the interaction length could be very long compared to a focused Gaussian beam. In 1997 Shinozaki et al. [74] made a theoretical study showing that the Bessel beam was indeed more efficient than the Gaussian beam, by as much as 48 %. In 1999 this was disputed as Arlt et al. [75] published experimental data showing that the Bessel beam was never as effective as a Gaussian beam of equal power. The problem with Shinozaki's analysis was that the comparison was made between a Bessel beam with $\Delta k = 0$ and a Gaussian beam with the same phase match condition. This condition, however, is *not* the optimum for a Gaussian beam, as Boyd and Kleinman showed in their paper [61], instead a finite value is needed in order to compensate for the Gouy phaseshift around the focus [76]. In 2000 Magni made the full calculation and demonstrated that the Bessel beam was indeed inferior to the focused Gaussian [77] when used for second harmonic generation. The optimum beam, shown in Fig. 3.17 turned out to be slightly different from the fundamental Gaussian beam, but did only result in a 2 % higher conversion efficiency. Later Magni expanded the theory to include sum frequency generation (SFG) and difference frequency generation (DFG) of arbitrary polarization [78].

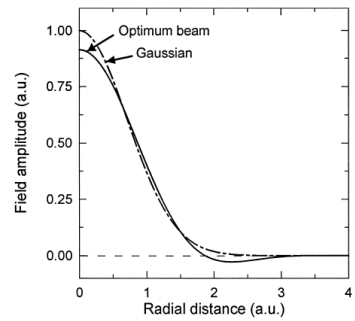

Figure 3.17. *Optimum beam profile, compared with the fundamental Gaussian beam. The optimum beam only provides 2 % higher conversion efficiency than the Gaussian beam.*

3.7 Nonlinear Crystals

Numerous different types of nonlinear crystals has been tested for SHG, at different wavelengths. A comprehensive list with data can be found in [79] and in the SNLO software [80]. Generally due to the high absorption of the materials in the UV/blue region only a small number of crystals are viable alternatives for the use of doubling 808 nm into 404 nm. In this section a brief review is done of some of these crystal materials.

3.7.1 Potassium Titanyl Phosphate - KTP

Potassium-titanyl-phosphate or $KTiOPO_4$ is a positive biaxial crystal, that was introduced in 1976 [81]. KTP belongs to a family of materials with chemical formulation $\{ K, Rb, Tl, Cs\}TiO\{P, As\}O_4$. The most common of these are KTP, KTA and RTP that are used for nonlinear frequency conversion and electro-optical cells (Pockels effect). The transparency range of KTP is 350 nm to 4.5 μm [82], and the damage threshold is high.

KTP is manufactured either in a hydrothermal process with high pressure and high temperature or in a low pressure and high temperature flux grown process. The manufacturing process is important for the physical properties of the crystal. The flux method is the most cost-effective due to the increased size of the boules that can be made. The hydrothermal process on the other hand provides better quality of the crystals. In particular hydrothermal crystals have higher damage resistance [83], lower ionic conductivity and higher resistance to gray-tracking. The Sellmeier equations also show differences between the two type of manufacture (see [79] and links therein). Gray tracking is a photo-chromic process in which the crystal starts to darken when exposed to high levels of radiation for long periods of time [84–86].

KTP can be non-critical phase matched for SHG down to about 995 nm [87] and this can be extended down to the important 980 nm region (InGaAs diodes) by doping the crystal with Na called KNTP [88]. Especially the doubling of the Nd:YAG laser line at 1064 nm to 532 nm has been extensively studied using angle phase matching [84, 89].

The largest d-tensor element in KTP is the d_{33} element with a value of 15.3 pm/V [90], that can only be accessed through periodically poling of the crystal. The poling of KTP can be done using the procedure described in section 3.5.3 and was done in 1994 [91] by applying a voltage of 2 kV/mm to the electrodes. This is an order of magnitude lower than what is required for Lithium Niobate and therefore allows for poling of thick crystals larger than 1 mm. Later in 1997 an ion-exchange process was used to reduce the ionic surface conductivity in flux grown KTP before applying the electrode [92]. Numerous different SHG experiments have been done with periodically poled KTP crystals see e.g. [93–97] The crystals used in this experimental work are flux grown PPKTP.

3.7.2 Lithium Niobate - $LiNbO_3$

Periodically poled Lithium Niobate $LiNbO_3$ is widely used due to its very high nonlinear tensor element of $d_{33} = 25$pm/V. Unfortunately LN suffers from a low threshold for photorefractivity [98], which limits its use in high power applications in the visible spectral region. This can be alleviated [99] by doping with a few percent MgO to create MgO:LN, and still maintain the large value of the d-tensor. The transparency range is about 330 nm to 5 μm, though with a lower damage threshold than KTP. The coercive field in LN is 21 kV/mm making it more difficult to electrically pole than KTP.

3.7.3 Lithium Tantalate - $LiTaO_3$

Lithium Tantalate is transparent down to 280 nm making it more interesting for UV application than KTP and LN. It has a damage threshold like KTP but do also suffer from mild photorefractivity. By controlling the crystal growth carefully it has been possible to grow stoichiometric LT (SLT) that does not suffer from photorefractivity. Poling of LT for SHG into the blue/UV range can only be made in about 0.2 mm thicknesses [100], which makes them difficult to work with.

3.7.4 The Borates

Lithium-tri-borate (LBO) [101], barium-borate (BBO) [102] and bismuth-borate (BiBO) [103] all belong to the borate group. All of these are transparent down below 200 nm, and this makes them the preferred choice when generating UV beams. They all have a very high damage threshold, that makes them ideal for intracavity and external cavity applications. None of the borates can be non-critical phase matched for SHG of 808 nm, and thus they will all infer a walk-off on the second harmonic beam. As described in section 3.5.1 this will limit the effective lengths of the crystals. The nonlinear d-tensor is 0.75 pm/V for LBO, 2.0 pm/V for BBO and 3.7 pm/V for BiBO for SHG of 808 nm light.

Chapter 4

Resonator Enhancement

For high power tapered laser diodes the output power are limited to a few Watts, which will only produce modest second harmonic powers in single pass setups. Typical single pass conversion efficiency parameters for periodically poled crystal are on the order of 1 $\%W^{-1}cm^{-1}$. Hence, in order to achieve high second harmonic output powers the fundamental beam needs to be amplified. Such amplification of the fundamental can usually be achieved by placing the nonlinear crystal inside the lasing cavity, and thereby take advantage of the higher intracavity power. This is not possible with diode lasers, as they are high gain devices with low reflectivities on their output facets. Another possibility is to place the nonlinear crystal in an external power buildup resonator[1]. This section concerns the concepts of external power build up resonators, specifically when used for second harmonic generation.

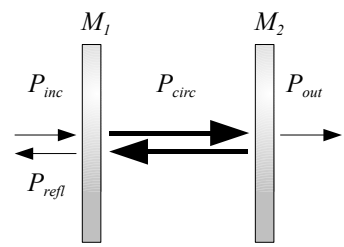

Figure 4.1. *The simple two-mirror standing wave resonator. The incident beam builds up in the resonator and after several passes exits through the output mirror.*

4.1 Concept of Resonators

An optical resonator is a device in which a laser beam is repeatedly propagating back and forth or around in a ring, due to reflections or refractions from optical elements. The simplest resonator consist of two (planar) mirrors set up in such a way that their normals are parallel (see Fig. 4.1). A beam that enters through mirror M_1 will propagate to mirror M_2 where it will be reflected back towards the first mirror, that again will reflect it back towards the second mirror and so on. Conceptually this kind of resonator is called a linear or standing wave resonator as the steady-state field in the resonator can be described as a stationary field or as a superposition of two waves propagating in opposite directions. Another possible configuration is the ring resonator, in which the propagation will be uni-directional. The ring resonator has two

[1] resonator and cavity are used interchangeably in the literature.

main advantages over the linear resonator. First the reflection on the outside of the input coupler is reflected at an angle, in order to allow for non-normal incidence needed for the ring geometry. This reduces the amount of reflected light that is coupled directly back into the laser source potentially destabilizing it. Secondly, the generated harmonic beam will be unidirectional, which will allow for a easier extraction from the resonator. The two separate frequency doubled beams of a linear resonator can be combined, but care must be taken to make sure it is done coherently.

4.2 Eigenmodes of a Resonator

When the beam is propagating inside the resonator it will diffract, and thereby the spatial mode distribution will change as it propagates. As the main idea of the resonator is to combine the incident field with the circulating field inside the resonator, these two beams need to be as identical as possible in order to sum coherently. The further the incident field is from the structure of the circulating field, the lower the coupling efficiency and power build up. It is therefore important that the resonator reproduces the beam parameters for every roundtrip at every position in the resonator. Hence at any reference plane in the resonator the spatial field distribution must only differ by a constant amplitude (the roundtrip loss) and an acquired phase factor for propagating one roundtrip. The spatial field distributions at n and $n+1$ roundtrips will thus be related as [76]

$$E_n(x,y) = \gamma e^{-ikL} E_{n+1}(x,y) \tag{4.1}$$

where γ is the loss coefficient and L is the roundtrip length. If this condition is fullfilled the beam is said to be in a supported mode of the resonator. It has been found numerically and experimentally [76], that these resonator modes can be described as Hermite-Gaussian or Laguerre-Gaussian depending on the symmetry of the resonator. For cartesian symmetry (square mirrors) the Hermite-Gaussian modes are dominant and for cylindrical geometry the Laguerre-Gaussian. Usually spherical optics are used and an expected cylindrical symmetry is expected. However, crystals and Brewster plates break this symmetry and favors the Hermite-Gaussian modes. The lowest order mode or fundamental mode is a simple Gaussian profile, and identical for both sets. The lowest order Gaussian mode is of most interest as it provides close to the highest conversion efficiency of all modes [77]. The divergence of the Gaussian modes is also increasing with mode order [76] and hence the diffraction losses in the cavity will be lowest for the fundamental beam. The coupling efficiency to single mode fibers that only support the fundamental Gaussian mode is crucial in many

applications, generally making it desirable to have the resonator operating in the fundamental Gaussian mode.

4.3 Gaussian Beams

A Gaussian beam can be described [76] as a spherical wave originating from a point source located at the position z_0, and propagating along the z-axis (see Fig. 4.2). The point source is of finite dimensions and called the waist of the beam. At this position the radius of curvature of the phase front is infinite and hence represents a planar wave, the transition from a converging wavefront to a diverging wavefront. It is important to realize here that a collimated beam usually seen as a parallel non-diverging beam is an idealization, that can not be achieved due to the finite extend of the source.

The amplitude u of a paraxial spherical wave with a point source at z_0 can be written as

$$u(x,y,z) = \frac{1}{R(z)} exp\left[-ik\frac{(x-x_0)^2 (y-y_0)^2}{2R(z)}\right] \tag{4.2}$$

where $R(z) = z - z_0$ is the radius of curvature of the wave at position z. Usually the propagation axis is chosen as the z-axis and we therefore set $x_0 = y_0 = 0$. We now introduce the q parameter as a complex radius of curvature, defined as

$$\frac{1}{q(z)} = \frac{1}{R(z)} - i\frac{\lambda}{\pi w^2(z)}, \tag{4.3}$$

again with R being the radius of curvature and w is the width or spotsize, defined as the distance from the center of the beam to where the intensity has dropped to $1/e^2$ as shown in Fig. 4.3. With this definition the Gaussian beam can be written as

$$u(x,y,z) = \frac{1}{q(z)} exp\left[-ik\frac{x^2+y^2}{2q(z)}\right] \tag{4.4}$$

$$= \frac{1}{q(z)} exp\left[-ik\frac{x^2+y^2}{2R(z)} - \frac{x^2+y^2}{w^2(z)}\right] \tag{4.5}$$

By including the Gouy phase shift and normalizing the expression the resulting expression for u becomes

$$u(x,y,z) = \left(\frac{2}{\pi}\right)^{\frac{1}{2}} \frac{exp\left[-ikz + i\psi(z)\right]}{w(z)} exp\left[-\frac{x^2+y^2}{w^2(z)} - ik\frac{x^2+y^2}{2R(z)}\right] \tag{4.6}$$

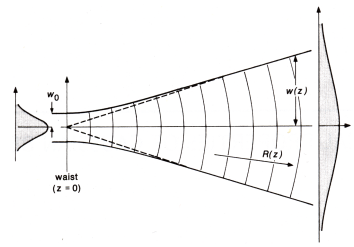

Figure 4.2. *The evolution of the width $w(z)$ as well as radius of curvature $R(z)$. The width at the focal point is called the waist w_0. From [76].*

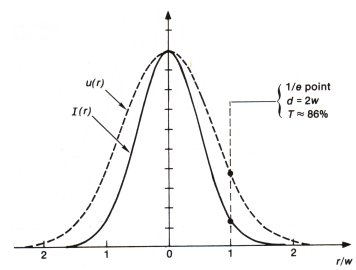

Figure 4.3. *The $1/e^2$ definition concerns the intensity $I(r)$. inside this defined width is 86% of the energy located. From [76].*

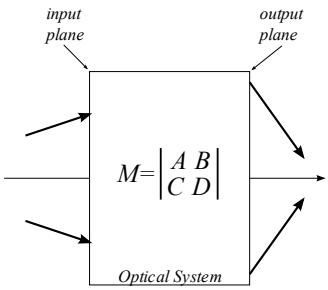

Figure 4.4. *An optical system can be expressed in terms of the ABCD matrix. It transforms the beam from the input plane to the output plane.*

with the width w, radius of curvature R and on-axis phase shift ψ given as

$$w(z) = w_0 \left[1 + \left(\frac{z}{z_R}\right)^2\right]^{\frac{1}{2}} \tag{4.7}$$

$$R(z) = z + \frac{z_R^2}{z} \tag{4.8}$$

$$\psi(z) = tan^{-1}\left(\frac{z}{z_R}\right) \tag{4.9}$$

where $z_R = \pi w_0^2/\lambda$ is the Rayleigh length of the beam.

4.4 Ray Transfer Matrices

The propagation of a Gaussian beam can be found by the simple propagation relation

$$q(z) = q_0 + z. \tag{4.10}$$

Of special interest is the q-parameter in the focus or waist of a beam. From Eq. 4.3 it can be seen that in the focus q is pure imaginary, indicating that it is a plane wave with infinite radius of curvature.

From geometrical optics the ray transfer matrix approach can be extended to the Gaussian beam regime where Kogelnik named it the ABCD law [104]. The ABCD law is used when transforming the beam by propagating it through optical elements like thin lenses, spherical mirrors, apertures, etc. For Gaussian beams the ABCD law is given by:

$$q(z_2) = \frac{Aq(z_1) + B}{Cq(z_1) + D}. \tag{4.11}$$

The elements A, B, C, D are all part of the ray transfer matrix combining all interactions between the beam and the optical elements encountered when propagating from $q(z_1)$ to $q(z_2)$.

Some of the commonly used ABCD matrices used in this work are listed in table 4.1, with more listed in [76, 105]. The transformation from start to end is calculated by multiplying the matrices in order to get the final transformation matrix.

As described in section 4.2 the resonator mode is self-consistent and can result in constructive interference between the incident field and the circulating resonating field if the two beams are in phase. It is very important when building resonators, that this eigenmode of the resonator is known, as the input beam must be shaped as close as possible to the resonator mode to increase the coupling efficiency, and hence the total power buildup inside the resonator.

Table 4.1: Some common ABCD matrices used when calculating eigenmodes of resonators. The tangential part is the out-of-plane part, and the sagittal is the in-plane part of the beam.

Optical element	Tangential	Sagittal
Thin lens focal length f	$\begin{pmatrix} 1 & 0 \\ 0 & \frac{1}{f} \end{pmatrix}$	$\begin{pmatrix} 1 & 0 \\ 0 & \frac{1}{f} \end{pmatrix}$
Spherical mirror, off axis (angle of incidence θ)	$\begin{pmatrix} 1 & 0 \\ -\frac{2}{Rcos\theta} & 0 \end{pmatrix}$	$\begin{pmatrix} 1 & 0 \\ -\frac{2cos\theta}{R} & 0 \end{pmatrix}$
Brewster interface (from n_1 into n_2)	$\begin{pmatrix} \frac{n_2}{n_1} & 0 \\ 0 & \frac{n_1}{n_2} \end{pmatrix}$	$\begin{pmatrix} 1 & 0 \\ 0 & 1 \end{pmatrix}$
Propagation in medium of index n	$\begin{pmatrix} 1 & \frac{L}{n} \\ 0 & 1 \end{pmatrix}$	$\begin{pmatrix} 1 & \frac{L}{n} \\ 0 & 1 \end{pmatrix}$

Stability of Resonators

The supported eigenmode can be found by the use of the ABCD roundtrip matrix of the resonator. The roundtrip matrix $\mathbf{M}$ is the resulting transform of the beam when propagated from an arbitrary reference plane and one time through the resonator back to the reference plane. In order for the resonator to be geometrically stable the half-trace of $\mathbf{M}$ must obey the inequality

$$|tr\,(\mathbf{M})| = \left|\frac{A+D}{2}\right| < 1 \tag{4.12}$$

If this relation is not true the field cannot circulate indefinitely, as each successive roundtrip will not reproduce itself exactly. This will lower the coupling efficiency and for low-loss resonators limit the build up power. The mechanical stability of the resonator will also be reduced as small changes in temperature or vibrations coupled into the mirrors, will change the coupling efficiency and hence the power build up. For those reasons such resonators are termed *unstable*. However, when operating in the stable regime ($|tr\,(\mathbf{M})| < 1$), the resonator will still support the mode despite small perturbations.

Eigenmodes

With knowledge of $\mathbf{M}$ the eigenmode q can be calculated as

$$\frac{1}{q} = \frac{D-A}{2B} \mp \frac{1}{B}\left[tr\,(\mathbf{M})^2 - 1\right]^{1/2}. \tag{4.13}$$

showing that there are two solutions to the eigenvalue problem. Only one of them is representing a valid physical mode, however,

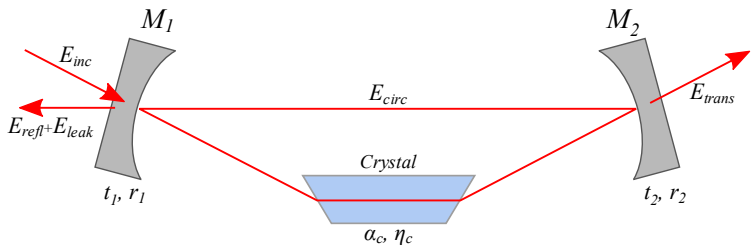

Figure 4.5. *The resonator geometry used in the experiments. The different reflectivities and loss terms are shown that contribute to the roundtrip loss. The loss from second harmonic generation is given as* γ_{SH}

as the other solution does not fall off with increasing r, thereby resulting in a mode carrying infinite power. The mode must have a negative imaginary term in order to provide this attenuation.

4.5 Power Buildup in the Resonator

When a field is incident on the input mirror of the resonator, part of the beam will be coupled into the resonator and add to the circulating field inside. the rest of the beam will be reflected by the input mirror. The circulating field inside the resonator will keep increasing in power until steady state is reached, in which the roundtrip losses are equal to the power coupled into the resonator. The theory of resonant enhancement in cavities with a nonlinear medium was first described by Ashkin et al. [106] and was later expanded by Kozlovsky et al. [107]. The treatment presented here is mainly based on Siegman [76] and Risk et al. [26].

The roundtrip losses are defined as all linear losses that the field experiences, except for the loss of the input coupler. A simple resonator is shown in Fig. 4.5 and from there the roundtrip losses can be seen to be $r_m = r_2\alpha_c$, where r_2 is the reflectivity of mirror M_2 and α_c is the total linear loss from passing through the crystal. If a larger numbers of mirrors are used then r_m will need to be multiplied by their amplitude reflectivities. Here we have used that the power reflectivity $R = r^2$ and for the mirrors we assume that $R + T = 1 = r^2 + t^2$.

The incident field is partly transmitted through the input coupler and acquires an i phase shift at the dielectric interface between air and glass. The steady-state condition on the inside of the input coupler will then be given as

$$E_{circ} = r_1 r_m E_{circ} e^{i\phi} + i t_1 E_{inc} \tag{4.14}$$

where the first right hand term is the roundtrip term for the circulating field. The phase factor is the acquired phase-shift from one roundtrip of propagation. By solving Eq. 4.14 we get

$$\frac{E_{circ}}{E_{inc}} = \frac{it_1}{1 - r_1 r_m e^{i\phi}} \tag{4.15}$$

In terms of powers this becomes

$$\frac{P_{circ}}{P_{inc}} = \frac{1 - R_1}{1 - 2\sqrt{R_1}\sqrt{R_m}cos\phi + R_1 R_m} \tag{4.16}$$

which is maximized when ϕ is a multiple of 2π, at which point no net phase is acquired during the roundtrip. The power enhancement can then be written as

$$\frac{P_{circ}}{P_{inc}} = \frac{1 - R_1}{\left(1 - \sqrt{R_1}\sqrt{R_m}\right)^2} \tag{4.17}$$

When building the resonator care must be taken to make sure the roundtrip length are an exact multiple of the 2π phase-shift, or introduce some means to achieve that dynamically. When free space optics are used, one of the mirrors can be mounted on a piezo-actuator, which allows for sub micron movement, and thereby change the acquired roundtrip phase-shift. In Fig. 4.6 an experimental sweep of such a piezo-mounted mirror is shown. The resonances can clearly be seen, with some smaller peaks in between. These smaller peaks are higher order modes, that are excited either through a misaligned cavity, or an imperfect pump beam containing these modes. Given temperature fluctuations, mechanical vibrations, and limitations in the optical elements, the complete elimination of higher order modes is very difficult.

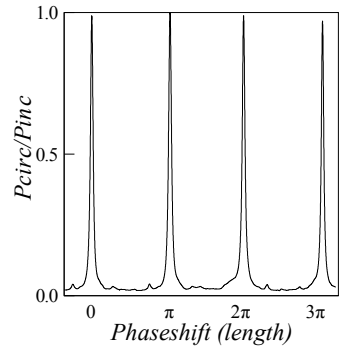

Figure 4.6. *Normalized resonance peaks of the experimentally used resonator. The power is measured through the HR mirror. The small peaks are higher order modes that have not been completely suppressed.*

4.6 Impedance Matching

The power reflected by the cavity can be found in a similar way as Eq. 4.14 where the reflected field is given as

$$E_{refl} = r_1 E_{inc} + jt_1 r_m e^{j\phi} E_{circ} \tag{4.18}$$

with the first right hand term being the direct reflection from the input coupler, and the second term is the transmitted portion of the beam that has experienced one roundtrip in the resonator. This can be rewritten as

$$\frac{E_{refl}}{E_{inc}} = r_1 - \frac{t_1^2 r_m e^{j\phi}}{1 - r_1 r_m e^{j\phi}} = \frac{r_1 - r_m e^{j\phi}}{1 - r_1 r_m e^{j\phi}} \tag{4.19}$$

which again on resonance with $\phi = 2m\pi$ gives

$$\frac{E_{refl}}{E_{inc}} = \frac{r_1 - r_m}{1 - r_1 r_m} \tag{4.20}$$

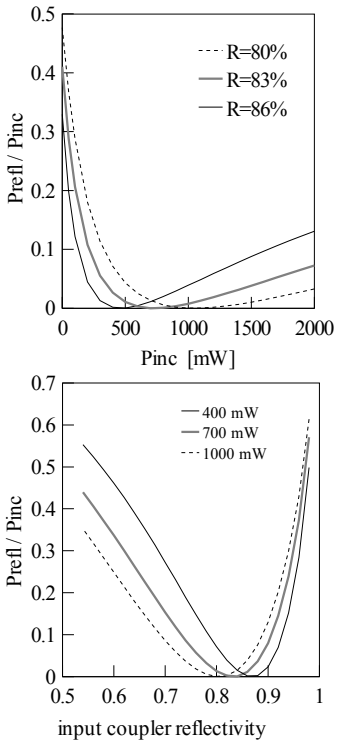

Figure 4.7. Top: *Shows the ratio between the reflected and incoming power vs. incoming power, for three different input coupler reflectivities.* Bottom: *The same resonator but with three different pump powers as function of the input coupler reflectivity.*

and for powers

$$\frac{P_{refl}}{P_{inc}} = \left(\frac{\sqrt{R_1} - \sqrt{R_m}}{1 - \sqrt{R_1}\sqrt{R_m}} \right)^2 \tag{4.21}$$

It can be seen that if $R_1 = R_m$ the reflection vanishes, resulting in all of the incident power being coupled into the resonator. This condition is called impedance matching, and might be counterintuitive as there is still a finite coefficient of reflection of the mirror. The reason is that the transmitted wave and the reflected wave are π out of phase, and the interference will be destructive. Are the two beams of equal amplitude, the fields will cancel out, and no energy will flow in that direction. As soon as the two 'reflectivities' are equal the resonator is impedance matched, irrespective of the incident power level.

However, when the phasematching condition is met in the crystal, it will generate a second harmonic beam, resulting in a loss for the circulating field. This additional loss must be accounted for in the roundtrip loss. Contrary to the linear losses, the nonlinear generation process is power dependent, and this results in the impedance matching to be power dependent as well. The nonlinear loss term is the single pass conversion efficiency of the crystal resulting in a transmission through the crystal of $T_{SH} = 1 - \gamma_{SH} P_{circ}$, with the single pass conversion parameter $\eta = \gamma_{SH} P_{circ}$ and γ_{SH} given as [107]

$$\gamma_{SH} = \frac{2\omega^2 d_{eff}^2 k_\omega}{\pi n^3 \varepsilon_0 c^3} \tag{4.22}$$

The power dependence on the resonator coupling is shown in Fig. 4.7, where the experimental resonator conditions have been used for the calculations. It can be seen that it is generally better for the input mirror to have slightly lower reflectivity, as the rate of change is faster when increasing the reflectivity of the input coupler.

4.7 Free Spectral Range, Finesse and Loss

By definition the distance (in frequency) between two resonance peaks are called the Free Spectral Range (FSR) and given as

$$FSR = \Delta\nu = \frac{c}{2L} \tag{4.23}$$

Beyond this frequency range the spectrum will just repeat itself.

The linewidth (in frequency) of a resonance peak $\Delta\omega_{FWHM}$ is an indication of the lifetime of a photon in the resonator. If the roundtrip loss is very low, two photons of slightly different frequency will travel many roundtrips, and their relative phase-shift will be large, and therefore will not interfere constructively. Large

roundtrip losses, results in only a few roundtrips, and therefore the difference in phase will be less. Hence the linewidth $\Delta\omega_{FWHM}$ is a measure of the accepted frequency bandwidth of the resonator. It is important when designing the resonator, that the acceptance bandwidth is larger than the laser linewidth, for effective coupling of the light.

The Finesse $\mathcal{F}$ is defined as the ratio of the free spectral range and the linewidth

$$\mathcal{F} = \frac{FSR}{\Delta\omega_{FWHM}} \tag{4.24}$$

and describes the resolving power of the resonator. The Finesse is also a measurement of the total loss L_{tot} of the resonator through the simple relation

$$\mathcal{F} = \frac{2\pi}{L_{tot}} \tag{4.25}$$

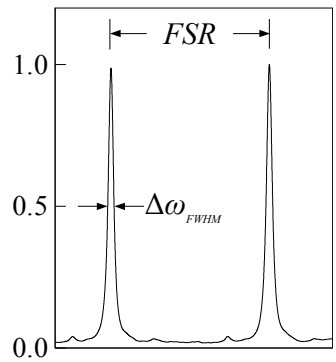

Figure 4.8. *Free Spectral Range and linewidth $\Delta\omega_{FWHM}$. The peaks are a blow-up of the first two peaks in Fig. 4.6.*

4.8 Mode Coupling Efficiency

If the incident mode on the resonator is not an eigenmode, it will couple as a superposition of modes into the resonator, and hence give rise to the scanning spectra with multiple peaks. All the energy in these modes are usually wasted, as we need a fundamental beam (or at least a single spatial mode beam) to exit the resonator. Therefore we try to transform the incident beam in order to optimize the coupling into the eigenmode of the resonator. The coupling Γ between two arbitrary modes E_1 and E_2 can be described as their normalized inner product [108]

$$\Gamma = \int \frac{E_1(x,y)\, E_2^*(x,y)}{|E_1(x,y)|^2\, |E_2(x,y)|^2} dxdy. \tag{4.26}$$

In order to calculate this, complete knowledge of the amplitude and phasefront needs to be known, at some reference plane. In the case of incident Gaussian beams, this problem was solved by Kogelnik [109]. If we have knowledge of the complex curvatures for the two beams to be matched, at the same z-coordinate, he showed the overlap could be calculated as follows

$$\Gamma = \frac{4}{\left(\frac{w_i}{w_r} + \frac{w_r}{w_i}\right)^2 + \left(\frac{\pi w_r w_i}{\lambda}\right)^2 \left(\frac{1}{R_r} - \frac{1}{R_i}\right)^2}, \tag{4.27}$$

here (w_i, R_i) is the incident beam parameters and (w_r, R_r) is the resonator beam parameters. The mode coupling power from incident to resonance mode are thus given simply as ΓP_{in}. Similar expressions can be found for higher order Hermite-Gaussian modes, see Maitland et al. [108]. It is important to note that if the incident beam is not a perfect Gaussian, then Eq. 4.27 will of course provide an upper limit to the overlap. The laser used

in the experiments, have successfully been coupled in with 85% efficiency. This is the overlap Γ_0 between a fundamental Gaussian mode, and the actual tapered laser mode. As stated earlier, the impedance must also be matched in order to avoid reflection from the resonator.

4.9 Changes For the Hot Resonator

Due to heating of the crystal material several different effects change the dynamics of the phasematched resonator compared to the non-phasematched resonator. Three main thermal issues have been important for the experimental work; thermal-lensing, local heating of the crystal and thermal expansion.

4.9.1 Thermal Lensing

When a Gaussian shaped beam is propagating through the crystal some of the power will inevitably by absorbed by the crystal. This absorption is usually not of particular importance as crystals with high transparency is used. In the NIR to visible/UV regime it is typically the borates BBO and LBO that are used, for medium power applications. These crystals have excellent transparency, but a low nonlinear efficiency. In order to use these crystals effectively a high finesse resonator is needed and according to Eq. 4.24 and 4.25 the resonator will have a low acceptance bandwidth. High power diode lasers can be unstable in absolute frequency and therefore needs a large acceptance bandwidth to achieve a high coupling efficiency. That can be obtained by using a long crystal with a high nonlinearity, effectively reducing the number of roundtrips in the resonator to less than 10, 1 or 2 orders of magnitude less than standard borate setups. One consequence of such a choice is increased absorption by the crystal. When the incident beam is Gaussian shaped the absorption will also be Gaussian shaped, and because of the nonzero temperature derivative of the index of refraction of the crystal, this will translate into a positive (GRIN) lens. This lens has the effect of changing the resonator eigenmode, and will of course be dependent on the circulating power and thereby on the incident power. The power of the thermal lens can be calculated as [110]

$$p = \frac{1}{f_{th}} = \frac{\alpha P_{circ}}{\pi K_c} \frac{\partial n}{\partial T} \int_{-L/2}^{L/2} \frac{dz}{w^2(z)} \tag{4.28}$$

where α is the absorption parameter of the crystal and K_c is the thermal conductivity. This effect can be compensated by adjusting the mode to that of the hot resonator [111, 112], though it makes it very difficult to setup, as the scanning mode pattern is

no longer the optimum. Another possibility is to dynamically adjust the mode inside the resonator with intracavity lenses, while the resonator is running [113], again this is difficult to adjust and it introduces rather high losses in the cavity. If the thermal lensing is not compensated the second harmonic mode will change, because the fundamental mode has changed and the coupling efficiency will decrease, due to the imperfect mode matching.

4.9.2 Reduction of the Effective Length

The large amount of heat absorbed by the crystal will locally change the temperature, and in steady state a temperature gradient will be established. When calculating the conversion efficiency of the crystal the temperature is assumed to be constant over the entire crystal, however with a large local heating that assumption will fail. The temperature increase generated by absorption can be found from solving the cylindrical heat equation $\nabla_r^2 T + \nabla_z^2 T = -Q/K_c$ with a Gaussian shaped source [114, 115]

$$\Delta T\left(r,z\right) = \frac{\alpha P_{circ} exp\left(-\alpha z\right)}{4\pi K_c} \times \left[ln\left(\frac{r_c^2}{r^2}\right) + E_i\left(\frac{2r_c^2}{w^2}\right) - E_i\left(\frac{2r^2}{w^2}\right)\right] \tag{4.29}$$

where K_c is the thermal conductivity, and $E_i\left(x\right) = \int_x^\infty \frac{e^{-u}}{u} du$ is the exponential integral function [116]. Figure 4.9 shows the temperature rise in a PPKTP crystal with 7 W of incident power due to absorption. The top part shows the contribution from the pump source only, while the bottom plot, shows what happens when 210 mW of blue power is generated according to Boyd-Kleinman theory. No thermal lensing effects have been included. The temperature bandwidth for a 30 mm PPKTP crystal is (according to Eq. 3.28) 0.37 K, and it can be seen that on the propagation axis the temperature difference is larger than that. This local temperature rise will therefore limit the generated second harmonic power, as the phasematching condition cannot be met over the entire length of the crystal.

4.9.3 Thermal Induced Bistability and Self-Locking

Another problem with the large absorption is the expansion of the crystal material itself. This expansion will change the roundtrip phase acquired by the field and as such the resonance peak will shift in frequency, which can be a source for bistable behaviour in the system [56]. The analysis is thoroughly described in Douillet et al. [110] and Ludlow et al. [117] and is briefly described here.

The change in refractive index with temperature is given as $n\left(T\right) = n\left(T_0\right) + \frac{\partial n}{\partial T}\Delta T$ with T_0 being the cold resonator temperature. When there is no absorption in the crystal (low circulating

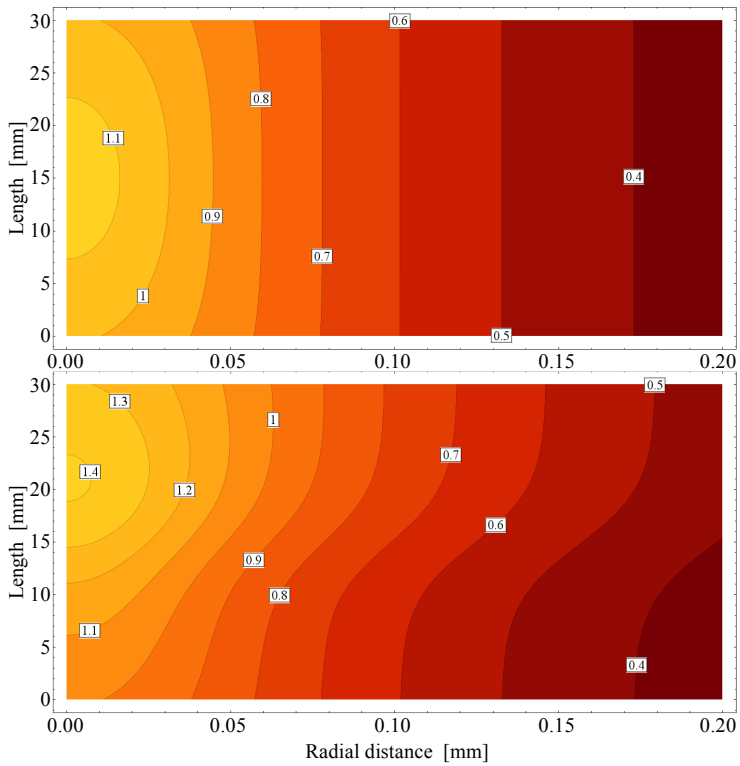

Figure 4.9. *Calculation of the change in temperature distribution in a 30mm PPKTP crystal, with 7 W input power and a waistsize of 50 µm. Note the asymmetrical scaling of the axes.*

power) the lineshape of a resonance peak can be written as

$$P(\nu) = \frac{P_0}{1 + F(\nu - \nu_0)^2} \tag{4.30}$$

where ν_0 is the resonant frequency, P_0 the power at the resonance and $2/\sqrt{F}$ is the FWHM of the resonance peak. Because of the temperature induced index change, the resonance peak will shift in frequency and ν_0 must be replaced with $\nu_0 + \Delta\frac{P}{P_0}$ in Eq. 4.30

$$P(\nu) = \frac{P_0}{1 + F\left(\nu - \left(\nu_0 + \Delta\frac{P}{P_0}\right)\right)^2} \tag{4.31}$$

The parameter Δ is called the *self locking range* as this is the frequency range that the resonance peaks can move. Figure 4.10 shows the bistable behaviour of the hot resonator. When scanning in one direction (to the right in Fig. 4.10) the crystal will expand

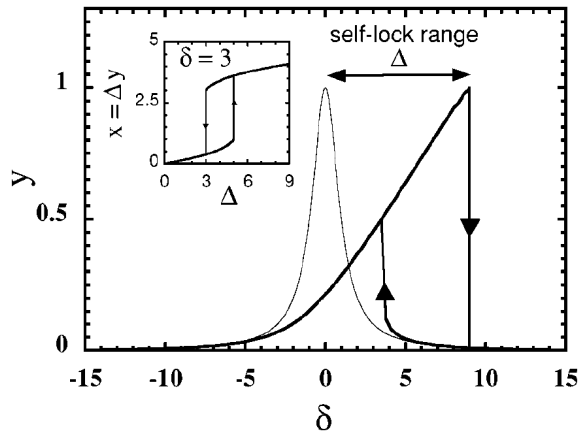

Figure 4.10. *The change in lineshapes are shown, with the thin Lorentzian as the cold resonance peak. The symbols relate to the treatment in the original work, $y = \frac{P}{P_0}$ is the the normalized intracavity power, δ the frequency detuning. From Douillet et al. [110]*

thereby increasing the roundtrip length, while the piezo mirror will decrease the length. This balance can go on until the top of the peak is reached, and a further move by the mirror will result in a cooling of the crystal, which suddenly is no longer phase matched, and the power will drop off immediately. When increasing the resonator length with the mirror, the crystal will start to heat up, but this time they do not balance and the peak is effectively compressed. This self-locking behaviour has been observed by several authors e.g. [96, 97, 110, 117–120]

4.10 Phaselocking

Previously it was shown that the circulating power is maximized when the roundtrip phase change is an integer multiple of 2π (Eq. 4.16). When the system is operating it will experience small temperature variations from the oven that will slowly reach steady state temperature, draughts of air induced by the operator will change the convection, changes in ambient conditions will alter the reference points for the thermal controller, mechanical vibrations coupled into the setup will change the distance between mirrors, etc. All these external perturbations will change the acquired phase shift during one roundtrip in the resonator. Hence in order to keep the system on resonance a phaselocking mechanism must be used.

In order for phase locking to work some kind of monitoring of

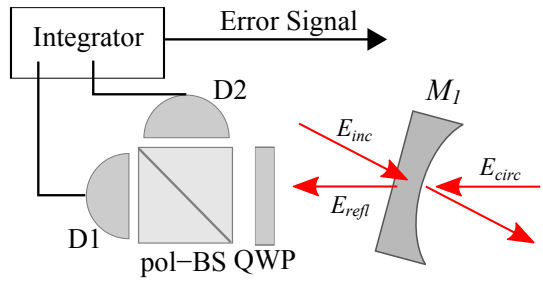

Figure 4.11. *The experimental setup used to generate the error signal in the Polarization Locking scheme. The incident field E_{inc} is linearly polarized and slightly angled compared to the $p-$polarization state supported by he resonator. The quaterwave plate (QWP) rotates the reflected signal, allowing the polarisation dependent beamsplitter (pol-BS) to decompose the beam. The generated error signal is sent to an amplifier driving the piezo mirror inside the resonator.*

the resonance peaks position compared to the laser frequency is necessary, and the different methods of locking are named after generation of this error-signal. There are basically two approaches to this, either the circulating field in the resonator is locked to the incident field (polarization locking frequency locking) or the incident laser field are frequency matched to the resonators resonance frequency (optical locking).

4.10.1 Polarization Locking

The polarization locking scheme was invented by Hänsch and Couillaud [121] and is based on the fact that different polarizations acquire different phase shifts in the resonator when propagating. A sketch of the experimental optical setup is shown in Fig. 4.11. The light incident on the resonator is in a linearly polarized state, which is slightly rotated compared to the supported polarization state of the resonator. Usually the roundtrip loss will be higher for one of the polarization states due to Brewster plates, mirror coatings, type-1 SHG processes or other deliberately introduced polarizing optical elements. The incident field can then be described as a superposition of the two orthogonal states of polarization of the resonator; the supported parallel $E_{inc,\parallel}$ and the orthogonal $E_{inc,\perp}$, or $p-$ and $s-$ polarization states. Inside the resonator only one of the components are experiencing low loss, the $E_{\parallel}$ component. Hence the $E_{inc,\perp}$ component of the light will be reflected

$$E_{refl,\perp} = r_1 E_{inc,\perp} \tag{4.32}$$

The $E_{\parallel}$ component consists of the direct reflection and the transmitted light through the coupler

$$E_{refl,\parallel} = r_1 E_{inc,\parallel} + it_1 r_m e^{i\phi} E_{circ,\parallel} = \left(\frac{r_1 - r_m e^{i\phi}}{1 - r_1 r_m e^{i\phi}} \right) E_{inc,\parallel} \tag{4.33}$$

On resonance the term in brackets in Eq. 4.33 is real and therefore the $E_{inc,\parallel}$ and $E_{inc,\perp}$ components are in phase, resulting in a linearly polarized reflected state. Off resonance the phase shift between the two components results in either slightly right or left-handed elliptically polarized light, depending on the sign of the phase difference. The quarter-wave-plate used in the experimental setup changes the states from RHC, linear and LHC into the same handedness but with a different tilt. This allows for a decomposition of the polarization state and thereby the ratio of the two components can be used to measure the distance from the resonance peak. The decomposition is experimentally done by using a polarization sensitive beamsplitter and two photodetectors as shown in Fig. 4.11.

Because of the inclusion of the quarter-wave plate, the setup is independent of the polarization direction of the linearly polarized signal on resonance. This is important when building a system, where the r_m coefficient changes and thereby the polarization direction of the reflected light as can be seen in Eq. 4.33. The broad wings of the error signal makes this locking scheme able to pick up large perturbations in frequency and phase, and therefore suitable for semi-mobile applications. The polarization-locking scheme has been implemented by several authors e.g. [122–125] as well as in Papers **IV** and **V**.

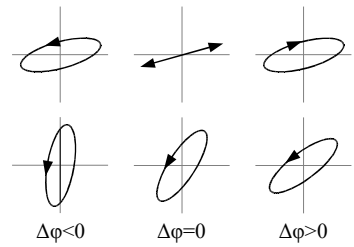

Figure 4.12. *Top row shows the reflected polarization state depending on the phase shift. The bottom row are the states after the quarter-wave plate. Adapted from [26]*

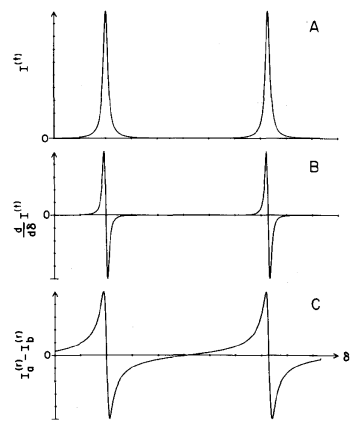

Figure 4.13. *The resonance peaks, and the error signals generated from the polarization scheme. A) the resonance peaks of the passive resonator. B) the first derivative of the resonance peaks. C) the dispersive error signal obtained using the polarization scheme. From [121]*

4.10.2 FM-Locking

In 1946 Pound [126] showed that a microwave cavity could be locked to a source by frequency modulation of the source. This technique was extended by Drever and Hall into the visible range [127] and hence called Pound-Drever-Hall locking. The basic idea is to frequency modulate the incident field with frequency ω_m and thereby induce sidebands in the spectrum located at $\omega \pm \omega_m$. These new frequency components will be π out of phase with each other, and when the resonator is on resonance the two components will be of exactly equal magnitude. Off resonance one of the sidebands will increase, at the expense of the other that will decrease. This behaviour allows for a lock-in amplifier to detect whether the resonator is below or above resonance. The resulting error signal is then either used to move a mirror in the resonator [113, 128, 129], or can be used to change the lasing frequency of the source itself [130, 131].

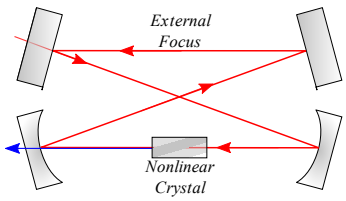

Figure 4.14. *Bowtie resonator [140] with four mirrors, can also be used with Brewster cut crystal.*

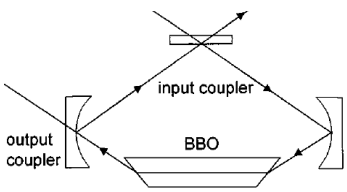

Figure 4.15. *Three mirror ring used by Bhawalkar et al. [125].*

4.10.3 Optical Feedback Locking

Another important locking technique is the passive optical locking, in which some part of the circulating field in the resonator is fed back to the laser, in order to use it as injection seeding. This technique is difficult to implement, as the coupled feedback into the laser must be carefully controlled. If not combined with any active locking [123, 132], this technique can be very slow in adjusting the system to large perturbations, as the circulating field might be very weak, and hence not large enough to seed the laser. This technique can be used in discrete elements setups [133, 134] or in monolithic rings [135] as these cannot easily be path length adjusted.

4.11 Resonator Implementations

A lot of different resonator designs have been tried out, here are listed some of the most relevant considering compactness and mobility.

4.11.1 Linear Configuration

The linear configuration design is used for its ease of setup, but major drawbacks are the normal incidence coupling on the input mirror, and the generation of a second harmonic beam in both directions, complicating the extraction. Linear cavities shaped as a Z are used to compensate for abberations in the optical elements [136], especially for compensating astigmatism induced when using Brewster cut crystals [137]. Other examples of linear resonators can be found in [133, 134, 138, 139].

4.11.2 Ring Configurations

Of the ring resonators, especially the four mirrors bow-tie setup [140] is widely used [123, 141]. This setup is used because of its flexibility when placing the components. It features a flat input coupler making mode matching easy. It has two foci, usually one with a large beam waist ($> 100\mu$m) for easy mode matching, and a much tighter focus for placement of a nonlinear crystal. Some aberrations can be compensated for, as well as thermal lensing with the proper choice of mirror radii and angles of incidence [142].

In order to reduce the round trip losses and/or make the resonator more compact, it is possible to reduce the number of mirrors to three or two. However, for each mirror removed, the alignment procedures become more difficult. A three mirror design has been demonstrated [125, 143], that compensated for both coma and astigmatism and used a flat input coupler.

With only two mirrors the experimental resonator used throughout in this work are an example of a very compact setup.

The alignment procedures are difficult compared to the bow-tie configuration.

4.11.3 Monolithic Rings

It is possible to have the entire resonator consisting of the nonlinear material by polishing mirrors onto the edges and coat the facets to obtain the desired reflectivity. Monolithic resonators are mechanically very stable, but can be more difficult to phase lock. Another problem is that it is not trivial to polish the facet of small crystals at the exact radius of curvatures needed, and difficult to change afterwards. Some examples of monolithic rings can be found in [135, 144–146].

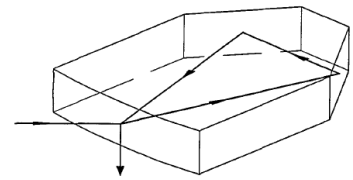

Figure 4.16. *The monolithic LN ring oscillator used by Gerstenberger [144]. Phase match is obtained along one of the long legs.*

Chapter 5

Laser-Induced Fluorescence and PDT

Laser-induced fluorescence (LIF) is a clinical diagnostic tool, that may be used in combination with photodynamic therapy (PDT). It may rely on the injection of a photosensitive drug, the fluorescent tumour marker or frequently also called the photosensitizer, as the drug also can be used for PDT sensitization. The fluorescent tumour marker fluoresces when illuminated within one of its absorption bands. After administration of the drug to the patient, it is selectively taken up by cancer cells, and thereby makes demarcation of any cancerous tissue possible. In this chapter laser-induced fluorescence as a clinical diagnostic tool will be treated, and the therapeutic modality of PDT will also be described.

5.1 Principle of Operation

The photosensitizer needed for fluorescence can either be topically applied to the skin injected directly into the suspected tumor volume or injected intravenously. For metabolized photosensitizers like ALA-induced protoporphyrin IX, the metabolism of the cell will start to convert the injected molecules to fluorescent and photodynamically active molecules. Cancer cells have, as in the case of ALA-induced protoporphyrin IX as a photosensitizer, an altered enzyme activity, resulting in a large concentration increase.

When the photosensitizer concentrated in the cancer cells are illuminated with light in one of its absorption bands, it will either fluoresce or make a nonradiative relaxation. The fluorescence path is called laser-induced fluorescence or photodiagnostics (PD), while the non-radiative energy transfer can result in the creation of cytotoxic species, and is the objective of photodynamic therapy. Due to energy losses in the fluorescence process, the emitted

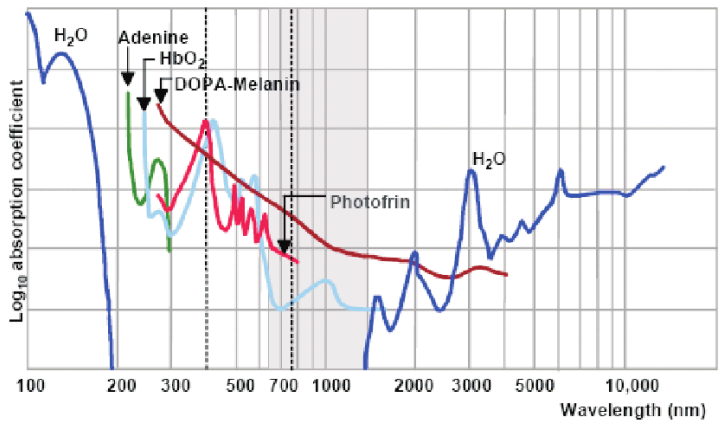

Figure 5.1. *The major chromophores absorption coefficient as a function of wavelength. A commonly used photosensitizer (Photofrin) is also shown. The grey area is the tissue optical window. Adapted from [147].*

fluorescence will be of longer wavelength than the incident light. The photosensitizers used experimentally in this project were both excited at 405 nm and emitted in the red spectral range at 635 nm (ALA-induced PpIX) and 652 nm (mTHPC). The fluorescence can be monitored externally using a camera, thereby establishing the presence of photosensitizer in the tissue. Such images provide information related to the concentration level of the photosensitizer throughout an extended area, and is therefore useful for demarcation of tumors or lesions.

The photosensitizer in this work has been selected for targeting cancer cells, although the selectivity could be changed to other parameters. The experiments have all been done on superficial targets, mainly skin, but also on mice organs and inoculated tumors in mice measured through the skin.

5.2 Photosensitizers

As the photosensitizer is to be used in human tissue, the penetration depth of the matching excitation light is important. In Fig. 5.1. the absorption spectra of the most important chromophores of human tissue is shown as a function of wavelength. The range from approximately 630 nm to 1300 nm is characterized by a low absorption coefficient and hence termed the tissue optical window. It can be seen that the longer the wavelength the larger the penetration depth, hence in order to activate a photosensitizer deep in the tissue it is important that it has an absorption band in the red or near infrared spectral region. A photosensitizer must also

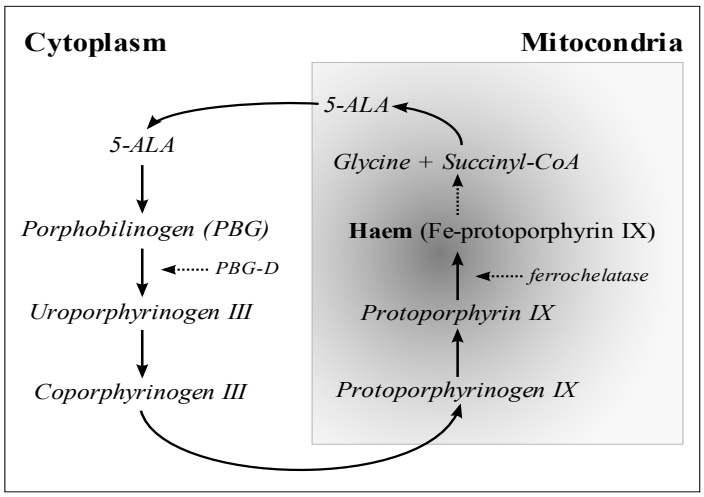

Figure 5.2. *The biosynthetic pathway for generation of haem. ALA is a natural occurring amino acid, that is synthesized in the first steps of the haem cycle. Ferrochelatase and PBG-D are important enzymes in the process, but their concentrations are lower and higher, respectively, in cancer cells. This gives rise to the large build up of PpIX in cancer cells. The dotted lines indicate feedback actions.*

be non-toxic and quickly cleared out of the system again, or it will result in prolonged periods of skin sensitivity. In the following the two photosensitizers used in the experimental work will be described.

5.2.1 ALA and PpIX

Amino-levulinic-acid (ALA[1]) is a natural occurring substance in the body, where it is metabolized in the haem cycle, according to the diagram shown in Fig. 5.2. ALA is produced in the mitochondria under negative feedback from the haem concentration. Upon entering the cytoplasm two ALA molecules condensate into porphobilinogen (PBG) using the enzyme ALA-dehydrase (ALA-D). PBG-deaminase (PBG-D) and uroporphyrinogen III cosynthase catalyze the process of assembling four PBG molecules to form the porphyrin skeleton. Finally in the mitochondria the PpIX is synthesized, and the only remaining process is for ferrochelatase to bind an iron atom in the center to create haem.

The negative feedback mechanism introduced by haem on the creation of ALA in the mitochondria, can be bypassed by supplying ALA from an exogenous source. The rate of haem pro-

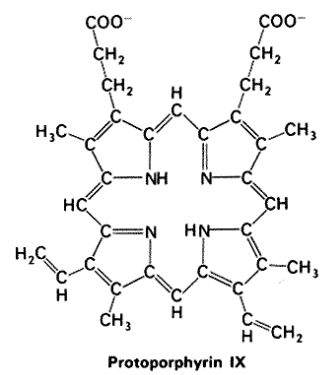

Figure 5.3. *The chemical structure of PpIX. The Fe-atom is later bound in the center, removing the two hydrogen atoms, in order to form haem.*

[1]Not to be confused with the omega n-3 fatty acid α-linolenic-acid, also commonly referred to as ALA.

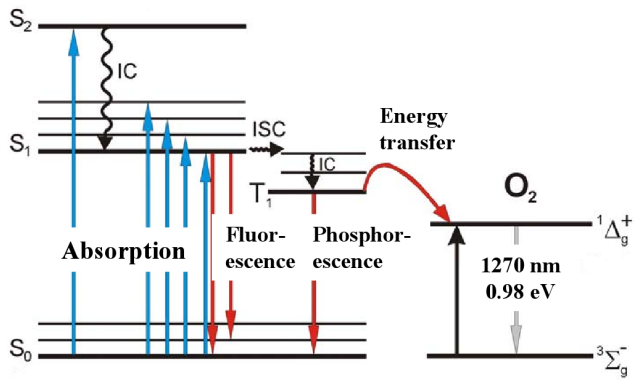

Figure 5.4. *Energy levels of PpIX and the energy transfer to oxygen. Excitation to the S_1-state is followed either by fluorescence or an inter-system-crossing (ISC) event. IC is nonradiative internal conversion. The decays involving change of spin, are dipole forbidden, and hence have a long lifetimes, making them meta stable states. The emission from a spin-changing decay is called phosphorescence, rather than fluorescence the emission from a spin-preserving deexcitation.*

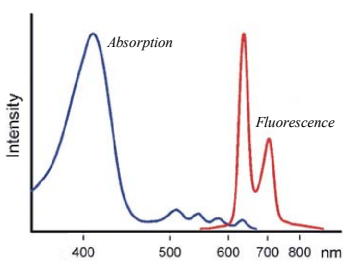

Figure 5.5. *The absorption and emission spectrum of PpIx.*

duction will then only be limited by the concentrations of the enzymes present. In cancer cells the concentration of ferrochelatase in the mitochondria has been found to be decreased compared to healthy tissue, and the ALA-D and PBG-D enzyme concentrations increased [148, 149]. The combination of a fast production of PpIX and a slow conversion into haem in cancer cells, gives rise to the difference in concentration between cancer cells and normal cells, also termed the selectivity. PpIX is both photodynamically active and give rise to fluorescence emission upon excitation, as illustrated in Fig. 5.5.

No fluorescence can, however, be detected after 24 hours in patients that have had ALA topically applied, resulting in a very short duration of skin photosensitization. The combined effect of high selectivity and only slight side effects (e.g. nausea) have resulted in a wide range of applications within various clinical fields [150–154]. The absorption of PpIX as a function of wavelength is plotted in Fig. 5.5, showing the dominant absorption peak around 405 nm, used for laser-induced fluorescence. Usually the small peak at 635 nm is used for PDT treatment, as the tissue absorption is low compared to the 530 and 405 nm absorption bands, allowing for a larger penetration depth.

The energy level diagramme for the PpIX system is shown in Fig. 5.4. When PpIX is excited to the S_1 level, a singlet state, it is possible to make a transition to a lower lying triplet state. This process is spin forbidden, but still have a finite possibility, due to the small energy difference between the singlet and triplet states.

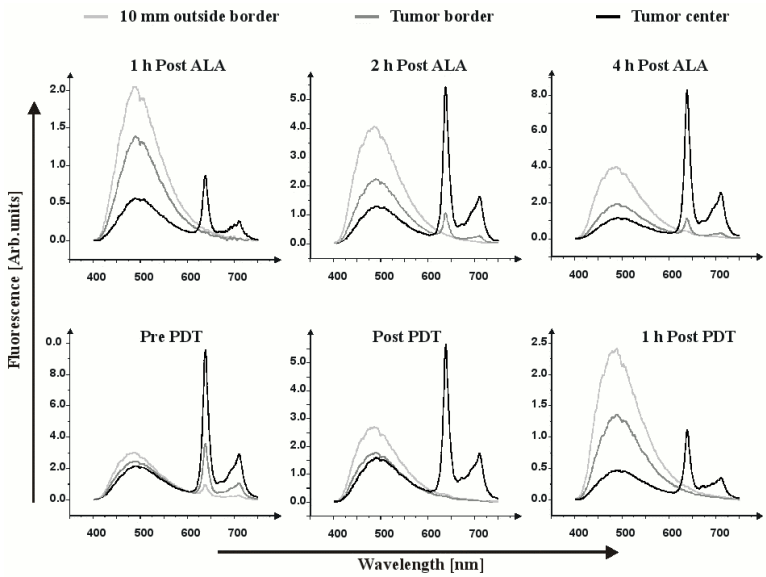

Figure 5.6. *The recorded fluorescence spectra, after illumination with a 405 nm source. Three positions are measured; center of tumor, edge of tumor, and 10 mm away from the tumor. The selectivity of the concentration to the cancer cells, can be seen from the fluorescence peaks at 635 nm, 2 hours and 4 hours after administration of ALA. Please note the different fluorescence scales.*

Further relaxation from the triplet state is also spin forbidden, resulting in a life time of approximately 100 μs. It is possible for the triplet state to transfer energy to an oxygen molecule that will be excited to a singlet state. This singlet oxygen is a highly cytotoxic species that will damage the cell, the desired effect in the PDT process. ALA-induced PpIX requires about 4-6 hours to reach its maximum concentration in cells after administration, and is usually cleared from the system in 24 hours.

The selective build up of PpIX in cancer cells can be seen in Fig. 5.6. Measurement were done 1 hour after topical application of the drug showing a difference in fluorescence from the center of tumor to the boundary. After 4 hours the change in fluorescence from the border to the center of the tumor increases to more than 10.

5.2.2 mTHPC

Meso-tetrahydroxyphenylchlorin or mTHPC, shown in Fig. 5.7, was used in some of the experimental work in mice. mTHPC is also known as Temoporfin or Foscan. Because mTHPC is hydrophobic, giving rise to difficulties in the administration of the

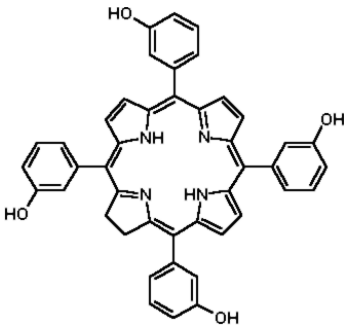

Figure 5.7. *Molecular structure of mTHPC.*

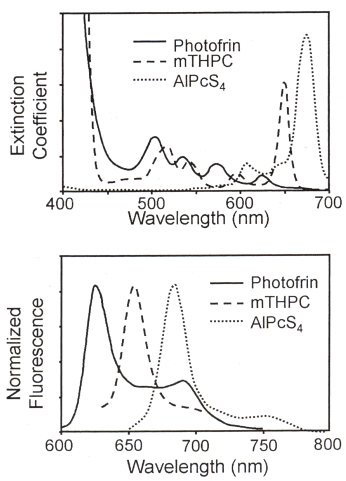

Figure 5.8. *Absorption and emission of mTHPC (dashed line). The treatment peak at 652 nm is very large compared to the 635 nm absorption peak in ALA.*

drug, some groups have recently suggested to administer the drug in a liposomal formulation. A novel approach is to use so called pegylated liposomes, produced by dissolving the drug into a mixture of polyethylene glycol (PEG), water and ethanol, a process called pegylation. This preparation can be administered systemically and given at least 24 hours to accumulate in the cells before starting the treatment. While the selectivity for the free form of mTHPC is lower than PpIX, with a reported value of 2 in carcinoma [155], the pegylated forms are more soluble and are found to provide a considerably greater selectivity [156]. Typically for hydrophobic photosensitizers, mTHPC localizes within the membranes of mitochondria, the Golgi apparatus and the endoplasmatic reticulum [157].

The treatment absorption peak can from Fig. 5.8 be seen to be locate at 652 nm allowing for larger penetration depth of the treatment light. mTHPC do also have a large absorption peak around 405 nm, that can be used for laser-induced fluorescence. The clearance of mTHPC is between 2 and 4 weeks, considerably longer than for PpIX. In this period the patient has to avoid as much exposure to light as possible.

5.3 Tissue Autofluorescence

When tissue is exposed to UV or near UV radiation it will fluoresce. This emitted fluorescence originate from the different fluorophores in the tissue, but mainly from ring-membered amino acids in collagen and glycoproteins. As this is the fluorescence of the tissue itself, it is called tissue autofluorescence. The fluorescence spectrum is dependent on excitation wavelength [160], as different fluorophores get excited at different wavelengths. By varying the excitation wavelength from 260 nm up to 480 nm, Gilies et al. [158] measured the autofluorescence as shown in Fig. 5.9.

For laser-induced fluorescence detection of tissue containing a photosensitizer, the autofluorescence will appear as a long tail, decreasing in intensity with increasing wavelength, superimposed on the recorded drug fluorescence spectrum, see Fig. 5.10. This contribution can be quantified by measuring on a sample of tissue, not containing any photosensitizer, or if impossible can measured before administration. This background fluorescence sets a lower limit of the amount of fluorescence from the photosensitizer that can be measured. In Fig. 5.10 the autofluorescence background has been approximated by a polynomial fit to the fluorescence spectrum at selected wavelengths, where the photosensitizer does not have any fluorescence. This fit can further be used to obtain the fluorescence signal, and can give information of the relative concentration of photosensitizer in the tissue, assuming that the

conditions in the skin are constant [159].

5.4 Bleaching of the Photosensitizer

As the photosensitizer is involved in the production of singlet oxygen (see Fig. 5.4), the possibility exists for the photosensitizer itself to be destroyed by oxidation. This bleaching of the photosensitizer, will reduce its concentration and thereby decrease the fluorescence and therapeutic effect [161]. As both PpIX and mTHPC have very large absorptions at 405 nm, the energy used for fluorescence diagnostics must be very low in order not to bleach the photosensitizer away and involuntarily start a PDT process.

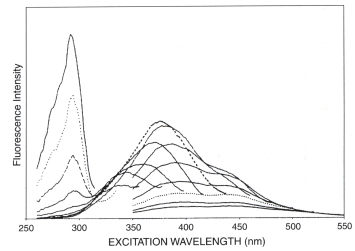

Figure 5.9. *The autofluorescence of normal skin, recorded for every 20 nm of excitation in the range 260 nm to 480 nm. From [158]*

5.5 Fluorescence Measurement Setups

5.5.1 Point Measurement

Point measurements can be done via small fiber probes, placed directly on the skin. The excitation light can be sent through the fiber and the fluorescence picked up by the same fiber. This is a simple measurement, that can provide insight to the local fluorescence properties in a small volume, and thereby clarify wether a particular part of the skin is part of a lesion or not. However, knowledge of the existence of the lesion or tumor must usually be acquired by other means beforehand, as this technique will be very slow for scanning larger areas. Due to the small excitation zone of less than a 1 mm^2, a low power light source of a few mW will be sufficient to detect the fluorescence. Gallium Nitride based diode sources are ideal for this type of experiment, as they are compact, and provide enough power to generate fluorescence in the small volume of blue light penetration in the skin.

By using two separate fibers, one excitation fiber and one pickup fiber, it is possible to make a 2-dimensional mapping of larger areas, by varying the distance between the two fibers (see Fig. 5.11. The larger the distance between the fibers, the longer the photons needs to travel, and hence due to multiple reflections, the probed volume will increase, as indicated in Fig. 5.11. By keeping the distance between the fibers fixed and moving both fibers, a mapping can be generated, although it will again be a slow process.

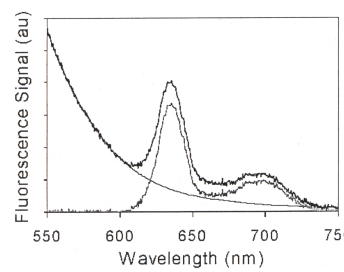

Figure 5.10. *The autofluorescence tail measured together with the fluorescence from PpIX. From [159]*

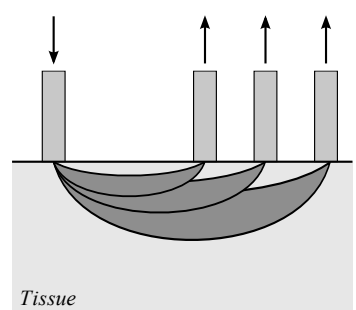

Figure 5.11. *The geometry in the point source measurements, with varying distance between the two fibers. The change in probed volume in illustrated.*

5.5.2 Extended Area Imaging

For larger areas or clinical screening purposes a complete imaging system with delivery optics of the excitation light and a camera is needed. The camera will, when equipped with suitable filters, be able to make a picture of the fluorescence intensity, and hence a demarcation of any tumor or lesion. The filters are needed to

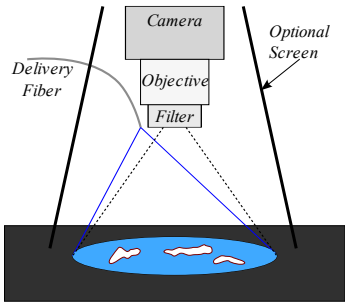

Figure 5.12. *Imaging setup for extended area fluorescence detection. A fiber delivers the excitation light to the tissue, and a camera picks up the fluorescence, using a (tunable) long-pass filter.*

remove the reflection from the excitation 405 nm blue light and the autofluorescence, and the short wavelength part of the ambient light. If both a long-pass and short-pass filter are combined into a band-pass filter, the filters can be tuned directly to the fluorescence peak of the photosensitizer used. However, as the fluorescence peaks are separated by several tens of nanometers, this setup will only detect one of the peaks.

In a clinical environment the ambient light levels might be very large in order to ensure optimum working conditions for a surgeon. In order not to bleach the photosensitizer extensively low laser intensities are used. This will inevitably lead to low levels of fluorescent light generated, and therefore a very sensitive camera is needed. The signal-to-background stray light ratio is an important parameter in order differentiate laser-induced fluorescence from background random specular or diffuse reflection of ambient light.

In order to reduce the background from ambient light as much as possible, different setups have been tried in the clinical work, when using a continuous wave source. Darkening of the room is the simplest technique, but light adaptation of the operator needs to be accounted for delaying the process. Furthermore, in a clinical setting during surgery it is not a feasible solution to turn of the lights to acquire a fluorescence image an then restore lighting.

A different route is to screen the camera and target area from ambient light, effectively enclosing the system by an opaque screen. This system is useable, but cumbersome to use, as the system needs realignment before each image, and the screen needs to be put in place and removed again.

In the experimental work reported on in Paper **VI** the ambient room lighting was turned off, and a cloth screen was used simultaneously to maximize the signal-to-background ratio. This combination was possible due to the experimental and non-clinical setting.

5.5.3 Time-Gated Imaging

One way to acquire fluorescence images with ambient light present, and without retorting to mechanical screens, is to use a pulsed laser system in combination with a time-gated camera. The idea is to use a short pulse of a few ns for excitation of the photosensitizer. This signal is triggering the camera which opens the shutter and starts the light acquisition. After a specified period a delay generator triggers the shutter to close. Two main benefits are achieved by doing this. First, as the integration time of the camera is only a few μs the ambient light will be reduced drastically than for a standard 50 Hz video frame rate of 20 ms a frame. Secondly due to the very short duration of exposure, the pulse energy can be made very large, while still maintaining a low overall average

power. A large pulse energy will increase the fluorescence signal an thereby increase the signal. Hence a substantial increase in signal-to-background is expected from a pulsed setup compared to a cw setup. If the pulses is synchronized in time with the video frame rate, a real-time fluorescence image can be generated and displayed to the surgeon while performing the surgery. This will alert the surgeon of areas of fluorescence that have not been treated yet, but that might otherwise not have been detected. On the other hand, due to the increased distinction of malignant and benign tissue, the amount of necessary tissue to be removed can be minimized. An important issue in neurosurgery and when treating e.g the intestines or vocal folds, where the amount of tissue to be removed must be kept to a minimum.

5.5.4 Imaging of Deeply Located Lesions

As the propagation of 405 nm light in human tissue is limited to a fraction of a millimeter, it is only the skin, the epithelial lining of the gastro-intestinal tract and the lungs, that can be imaged from the outside (or via an endoscope). If the position of a tumor is known or known approximately, imaging might still be possible using fluorescence tomography. The knowledge of the location of the interstitial tumor could acquired by a traditional means like CT scanning, ultrasound, X-ray, etc.

In case of an interstitial tumor it is possible to use thin optical fibers inserted from outside through the tissue and into the tumor itself. By measuring the fluorescence as a function of position of the fiber end, it is possible to make a 3-dimensional density map of the tumor. If several fibers are used simultaneously, excitation light can be sent through one of the fibers, and the fluorescence can be measured in the other fibers. Apart from measuring the physical extent of the tumor the fluorescence can also be used to monitor an ongoing PDT treatment, through the fibers. This will help reduce overexposure and the subsequent destruction of the surrounding healthy tissue.

5.6 PDT

Photodynamic Therapy occurs when the incident light on the photosensitizer results in the creation of singlet oxygen instead of fluorescence decay. The created singlet oxygen molecule is highly cytotoxic, as it can oxidise many of the components in the cell, leading to cell death. The diffusion length of singlet oxygen is a few tens of nanometers [162], and hence it is the position of the photosensitizer in the cell that defines the primary targets of the singlet oxygen. As the photosensitizer is also present in healthy tissue it is important to take measures to minimize the exposure to healthy areas. The photodynamic reactions are not discriminatory, concerning

malignant and non-malignant cells. The selectively destruction of cancer cells is due to the higher concentration of photosensitizer in these cells, not the fact that they are cancerous. ALA-PDT treatment is done using the 635 nm absorption line, which allows for the largest tissue penetration compared to the shorter wavelength peaks. However, it is important to remember that treatment can be done with 405 nm and 532 nm as well, and a lot faster, due to the higher absorption coefficient at these wavelengths. But such PDT will only be very superficial as the light has a very limited penetration depth. Hence, when using 405 nm for laser-induced fluorescence the intensity must be as low as possible, while still being capable of having a useful signal-to-background ratio.

Chapter 6

Clinical Results

Different clinical measurements were made throughout the project. A continuous wave source was used for imaging and verification of PDT treatment in patients diagnosed with skin cancer. The continuous wave system was rebuilt as a pulsed system, in order to measure the changes in the signal to background ratio. In this chapter some of the clinical results obtained in the project are presented.

6.1 The Portable Setup

The laser system to be used in the clinic was built on a 60x45 cm breadboard, from discrete optical components. A layout and a description of the experimental setup can be found in Paper **IV**. In order to make the setup mobile, it was placed on a the top shelf of a cart, with the current supply, water pump and reservoir, temperature controller for the crystal oven and piezo controller, placed on the shelves below. The breadboard placed on the top shelf was encased in black anodized aluminium plates, to serve as protection from the laser radiation. A picture of the cart with the breadboard on top are shown in Fig. 6.1.

Figure 6.1. *The mobile laser system used in the clinical trials. The black plates encase the breadboard system on the top shelf. Below are the temperature, piezo controller and water pump. The diode current supply is placed on the bottom on shock absorbing styrofoam.*

6.2 Measurements with cw Source

Measurements with the system operating in cw mode were done on patients being treated with ALA-PDT for skin cancer. Several trips to the department of dermatology at the University Hospital in Lund were made in order to measure the fluorescence before and after treatment with red light. The blue output beam from the resonator was coupled into a delivery fiber and routed to the camera, for illumination of the target area. The fiber used was typically a multimode large core fiber of 400-600 μm in diame-

ter. This provides for a reasonably slow beam divergence, but also introduces speckle problems, due to the spatial coherence properties of the laser. The spot is targeted at the cancer lesion on the patient, using mainly the center part of the beam to avoid edge effects. The induced fluorescence is picked up by the camera after passing through a band pass filter, that allows for separation of the different spectral contributions.

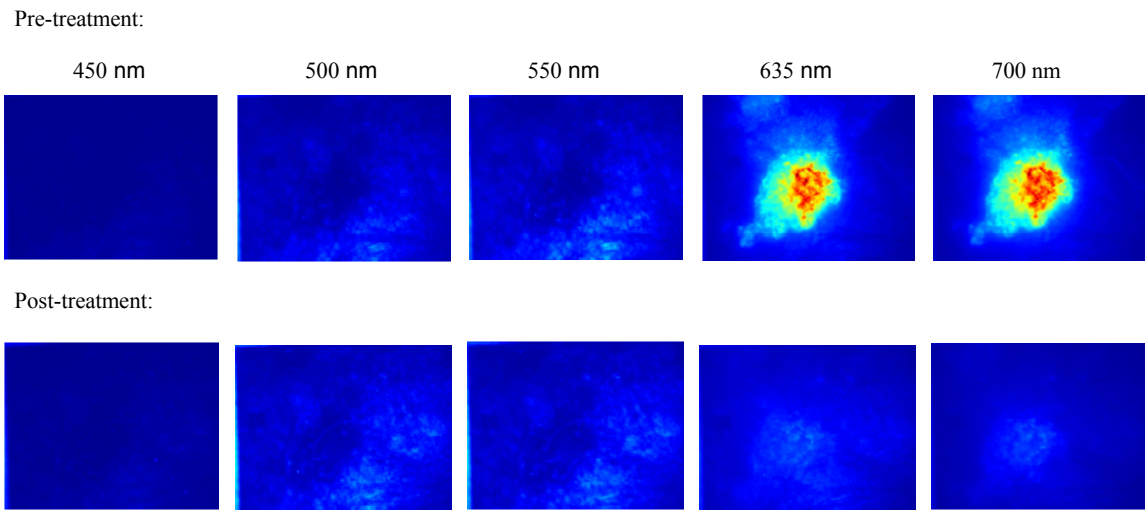

Figure 6.3. *Fluorescence picked up by the camera from a cw laser exposure. Top row is before ALA-PDT treatment, bottom row is after treatment.*

Figure 6.2. *A black and white image of the patient treated. The lesion is located in the center of the picture between the hairline and the eye (anonymized).*

In one of the clinical measurements a patient had a cancer lesion located between the left eye and the left ear (Fig. 6.2. The lesion was approximately 1 cm in radius. By measuring before and after the treatment it can be verified if the photosensitizer has been bleached by the PDT process as expected. In Fig. 6.3 five different wavelength filters have been applied in succession, clearly showing the two fluorescence peaks at 635 and 700 nm. The PDT treatment lasted 15 minutes using a diode array as source, about 4 hours after ALA had been topically applied to the lesion.

6.3 Measurements with Pulsed Source

In order to use the system in situations with ambient light present, the blue light source must be pulsed. This was achieved by moving one of the mirrors back and forth, thereby bringing the resonator on and off resonance (see Fig. 6.4). The periodic variation of the supplied voltage to the piezo is usually termed scanning the resonator. It is important to realize that this effect is not the

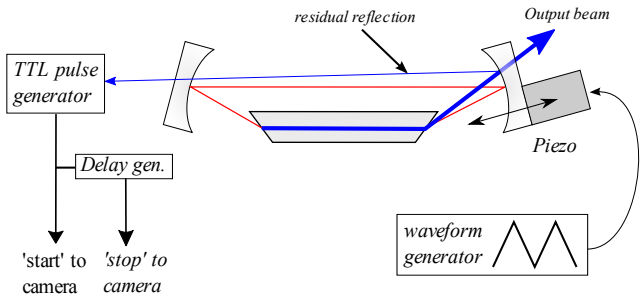

Figure 6.4. *A schematic of the triggering used in the pulsed setup. The small reflection from the output coupler, is used to trigger the camera to open the shutter. Simultaneously the signal is starting a delay generator, that fires after a set time, closing the camera shutter.*

same as the Q-switching usually applied to solid state lasers. In these lasers a higher population inversion can be achieved if the output coupling is blocked. Later when the output coupling is suddenly increased all the stored energy will be released as a giant output pulse. When scanning the external cavity, the Q-switching will only modulate the light, and the peak power should therefore be almost identical to the output power obtained when operating in continuous mode. However, due to the large thermal effects present in the PPKTP crystal used, the scanned output power was more than twice as large as the cw output power, as reported in Paper **V**.

When the piezo is scanned at constant velocity the pulses will be Lorentzian shaped, but the repetition rate and pulselength can be chosen within the limits set by the piezo driving the mirror. An experimental maximum of 6200 pulses per second were generated with the piezo, with an applied sinusoidal voltage. Because of the inertia of the mirror, the linear relationship between supplied voltage and piezo expansion is not valid around the turning points. Thus peaks located in these areas will be distorted. It is therefore important to tailor the supplied voltage pattern to minimize the influence of these nonlinear regions. The shortest observed pulse was 6 μs FWHM, but due to the inertia of the mirror the pulselength varied a lot from pulse to pulse.

In Fig. 6.4 the resonator is shown with the path of the blue output beam. Because the output mirror is about 4% reflective for 404 nm light, this specular reflection can be used to determine the beam output power, without disturbing the main beam. The specular beam is transmitted 96% through the input coupler and picked up by a detector, that will send a TTL high when a set threshold is reached. This change in signal level, triggers the camera to open the shutter and start integrating. After a set time a

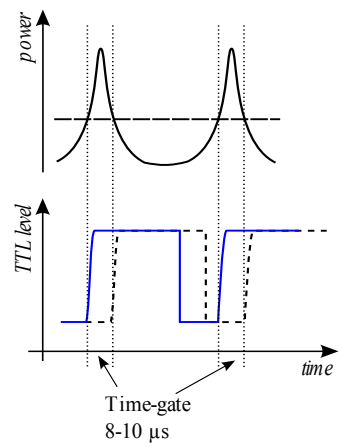

Figure 6.5. *The triggering due to the detected output power of the resonator. Top shows the scanning fringe pattern of the resonator. The dashed line is the threshold for the TTL pulse to be emitted. Bottom shows the other TTL signal from the delay generator, here tuned to the entire width of the pulse. The small window is the time-gated integration window of the camera.*

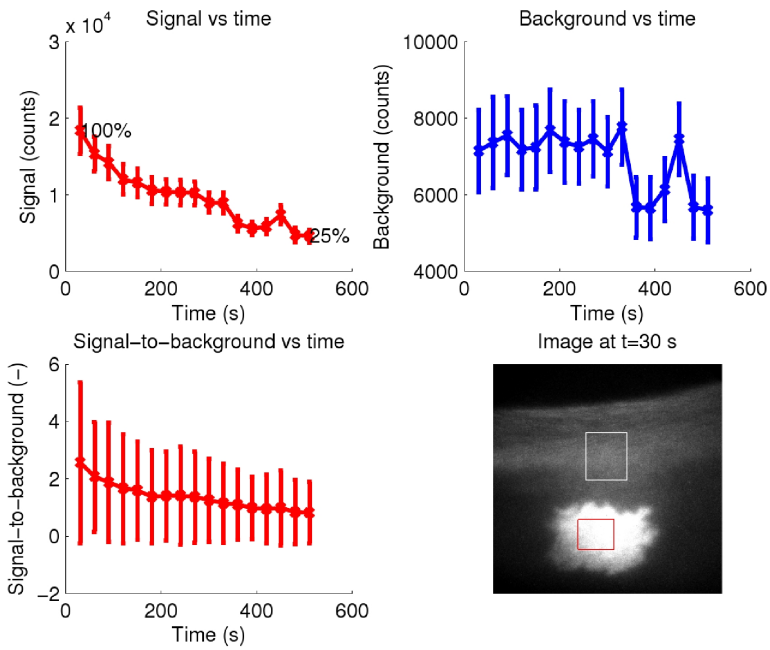

Figure 6.6. *The signal to background in an 8 minute long exposure to 10 mW average power radiation. The lower left shows how the signal and background area calculated as averages over a representative region in the picture.*

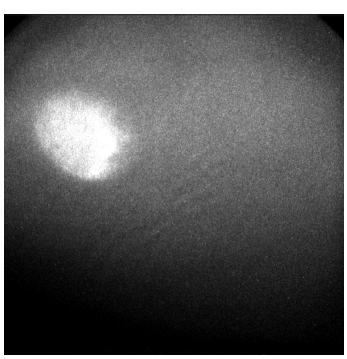

Figure 6.7. *An image at 635 nm of a healthy patient. Both ambient light and directed spotlights were used for added illumination, in order to simulate clinical relevant conditions.*

delay generator will trigger the camera to close its shutter and the integration will stop. The camera and delay generator both works with nanosecond resolution and can easily be tuned for maximum performance, by chopping out the piece of the pulse that is needed for best signal-to-background ratio. A delay of about a hundred nanoseconds is used to allow for the photosensitizer to relax, and for the emitted photon to escape the tissue. In Fig. 6.5 the triggering is shown graphically. The output signal from the resonator is shown along with the threshold for triggering. The delayed pulse from the delay generator can be seen to define the short window of light acquisition.

Due to the thermal problems in the PPKTP crystal the optimum beamwaist in the crystal is different for scanning mode operation and cw operation. Hence the system was rebuilt several times with different spherical mirrors in order to test for the optimum values. These results are reported in Paper **V**.

The average power obtained from the pulsed laser system is about 10 mW, which potentially might be a problem in relation to the bleaching of the photosensitizer. Hence a study was made on healthy patients (the author included) in which ALA was applied

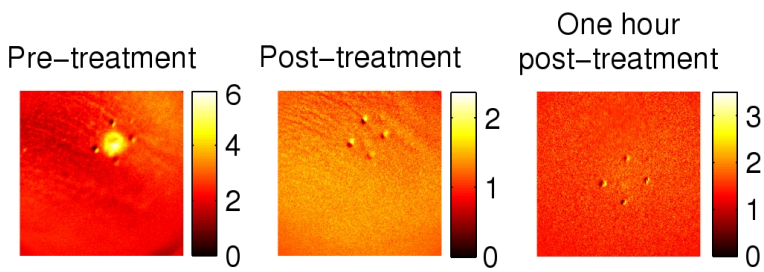

Figure 6.8. *Images of the fluorescence at 635 nm, acquired in pulsed mode, with full ambient lighting. Please note the difference in scales.*

to the smooth skin on the underarm. The ALA was covered by a small bandage to protect it from ambient light, and given 4 hours to be absroped by the skin. Immediately after the bandage was removed the tests were done with the pulsed laser on the arm.

Using ambient room lighting and spotlights directed at the ALA-treated area, pictures were taken at different wavelengths. The picture shown in Fig. 6.7 was filtered at 635 nm yielding the highest contrast with the background. The homogeneity within the fluorescent area is attributed to the non-cancerous tissue used, and the noise present in the picture is partly due to the high spatial coherence of the laser. By actively perturbing the fiber and scrambling the modes, this noise source can be reduced significantly. Even though a large part of the ALA should have been metabolized into haem after 4 hours, the fact that fluorescence could still be picked up in full lighting, shows that it would be clinically possible to detect the much larger fluorescent dose present in cancer tissue.

In order to estimate if bleaching were present due to exposure to the 405 nm high-power source, 16 images were taken with intervals of 30 seconds, and the signal to background were calculated for each measurement. In Fig. **??** the fluorescence signal, the background and the ratio are shown as function of time. It can be seen that some bleaching is observed, but not anything that would be damaging in a clinical situation in which the target area would only be illuminated for the duration where the cameras shutter would be open. In this test the target was illuminated for the entire 8 minutes.

At the Lund University Hospital patients were treated in a procedure similar to the one used with the cw system, except that the system were now optimized for maximum output power in scanning mode. A patient with a lesion on the stomach was given a topical administration of 20% ALA cream, and 4 hours were allowed to elapse before treatment.

Figure 6.9. *A tumor located next to the navel of the patient. The four dots are made with ink, that fluoresce when illuminated with 405 nm light. They are used for orientation of the false color images.*

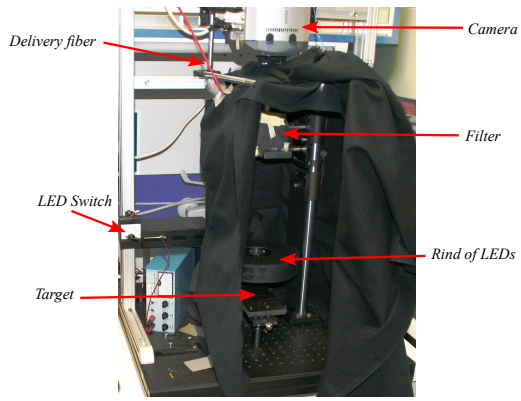

Figure 6.10. *A picture of the fluorescence setup used in the FosPeg study. The camera is placed on top, with the fiber to the left. the computer used to control the camear and process the image is placed on the table to the left.*

The fluorescent images made in full ambient lighting conditions are shown in Fig. 6.8. A large background is observed in all pictures, but the number of counts in the lesion area is between 2 and 3 times larger making it easily to visually observe the extent of the lesion.

6.4 Pharmacokinetics Study of FosPeg in Mice.

The laser system was also used in a large test regarding the pharmacokinetics of an mTHPC pegylated liposome preparation, called FosPeg, in mice. The aim of the study was to assess whether the detected fluorescence emitted from the tissue could be used to determine the concentration of the photosensitizer in the tissue, and thereby allow pharmacokinetic studies of the drug. A total of 30 mice were inoculated with a tumor on each hind leg. They were divided into 6 groups each consisting of 5 mice. Each group except for the control group were given FosPeg in the tail vein. The laser-induced fluorescence measurements were done 0.5 hour, 2 hours, 4 hours, 8 hours and 18 hours after the injection of the FosPeg intravenously. The results of the pharmacokinetic study are reported in Paper **VI**. The mice were imaged first in vivo lying on the small table, with their back facing the camera. These images showed that it was possible to detect the fluorescence from the underlying tumor, through the skin of the mouse.

The imaging system used in the experiments is shown in Fig. 6.10 and was built like the schematic in Fig. 5.12. The only difference was and added ring of LEDs placed about 7 cm above the sample. These LEDs were used for reflectance measurements, and

had center wavelengths of 405, 525, 635, 660 and 720 nm. In addition to these wavelengths a 470 nm filter setting was also used, in which the reflectance measurement from the 405 nm LEDs was used. After the initial in vivo imaging the mouse were sacrificed, and immediately placed on their back for *in situ* imaging of the organs and tumors. Each organ was then carefully extracted and the fluorescence image was recorded. The organ was subsequently chopped and stored for later high performance liquid chromatography HPLC processing, done in order to chemically establish the concentration of photosensitizer in the tissue.

6.4.1 Fluorescence Imaging

One of the applications in which laser-induced fluorescence is expected to make a significant impact, is real-time imaging of tumors and lesions, based on their fluorescence signature. In Fig. 6.11 an image of the tumor in one of the mice can be seen. 5 pictures were taken, one through each of the filters. As expected a large fluorescence signal can be seen at the 652 nm wavelength, of which FosPeg is highly absorbing. The background is not as pronounced, resulting in a decent contrast to aid in the demarcation.

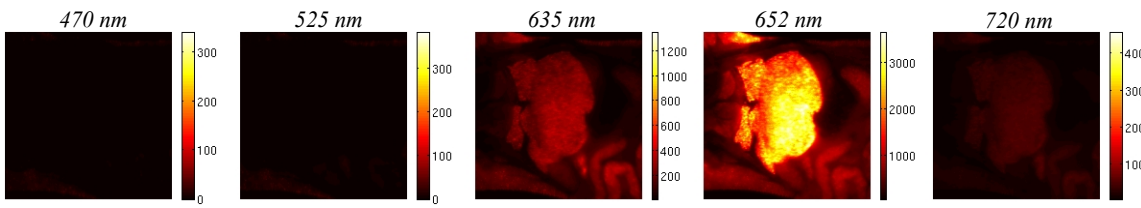

Figure 6.11. *A tumor imaged in the mice in situ. The wavelength relates to the liquid crystal tunable filter used in front of the camera. The excitation source was in all circumstances the 405 nm laser. Note the different scales.*

Each of the organs were excised from the mice and imaged individually, in order to correlate the amount of fluorescence detected, with the concentration that could be chemically measured using the HPLC technique. In Fig. 6.12 spleens from six different mice each from one of the different groups are shown. An increase in fluorescence is detected and peaks in the 8 hours image, as the 18 hour mouse is slightly lower in fluorescence.

The cancer cells should have a larger uptake of FosPeg than normal cells, and hence the fluorescence is expected to be somewhat higher for the tumors. In Fig. 6.14 it can be seen that the count number is a factor of 5 larger for the tumor than for the spleen cells, showing that there is a usable selectivity. The fluorescence from the cancer do not, however, fall off after 18 hours as was the case for the spleen. When used in patients Foscan is

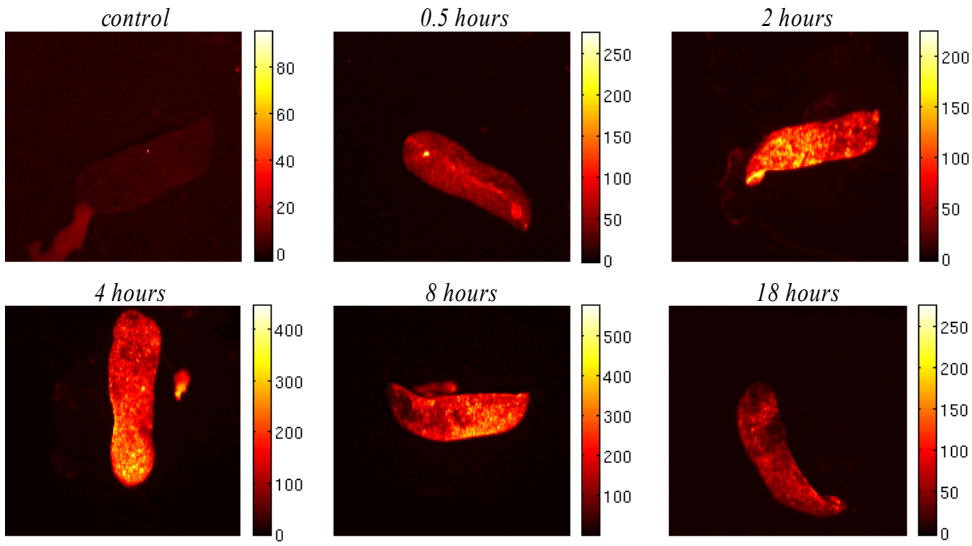

Figure 6.12. *Ex-vivo images of 6 different mice spleens at different times after administration of FosPeg. The first picture is a spleen from a control mouse that has not been injected with photosensitizer. Note the difference in color coding.*

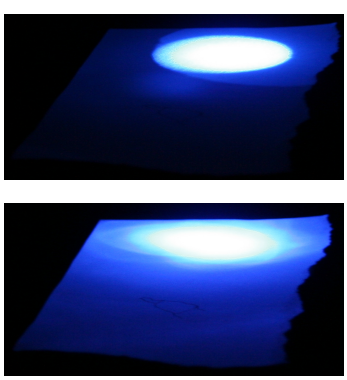

Figure 6.13. *The spotprofile for the light sources. Top is the laser source, and bottom is the LEDs. The pictures are unprocessed.*

usually allowed at least 24 hours of uptake in order to achieve the best selectivity. This could be the result of increased tumor concentration, and decreased concentration on non-cancer tissue.

6.4.2 Laser vs. LED Source

One of the benefits of using laser sources instead of LED based sources are the large coupling efficiency to optical fibers. This is an important issue when used in interstitial geometries, but for imaging in free space an LED source might be useful. In Fig. 6.13 are shown two images of the spots as they appeared on a white piece of paper, placed at the target area in the experimental setup. The images were taken with the same full-color SLR camera (Canon 350D), with identical exposure time, aperture and focal length. It can be seen that the directionality is greater for the laser compared to the LEDs, and the spatial pattern on the paper is more uniform. The total light power, however, seems to be greater for the LEDs than for the laser, an observation that is also true for the naked eye.

The fluorescence of the same organ with both sources are shown in Fig. 6.15 for easy comparison. It can be seen that the wide spectrum of the LED produces less fluorescence than the laser source. Speckle are non existant for the broad bandwidth LED, but can be a problem when using the laser source. It was not

possible to measure the spectrum of the LEDs, as the amount of light coupled into the 50 μm diameter fiber was too small to be detected with the optical spectrum analyzer.

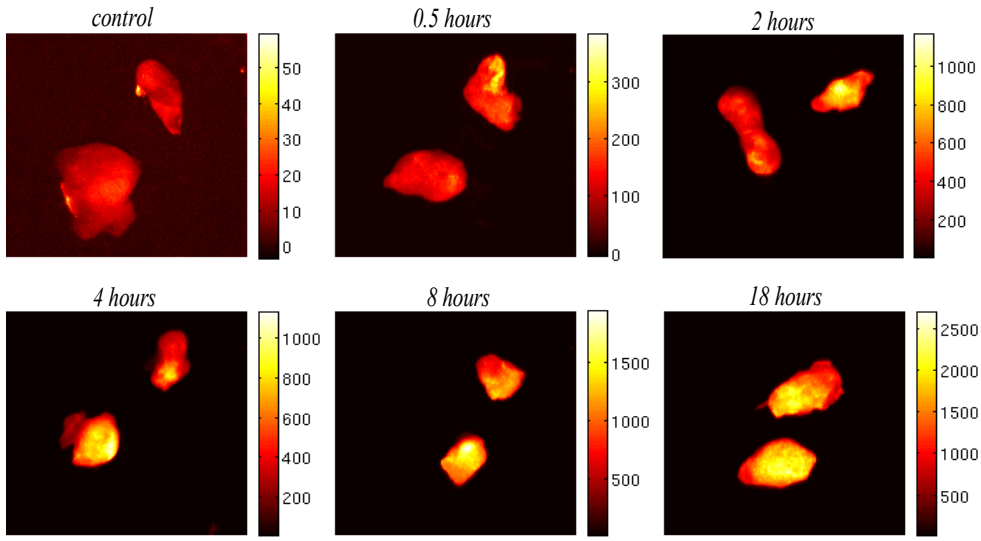

Figure 6.14. *Ex-vivo images of the inoculated tumors. The tumors are more uniformly fluorescing indicating a smooth distribution of photosensitizer in the cells. The peak fluorescence is found to be after 18 hours, compared to the 8 hours of the spleen.*

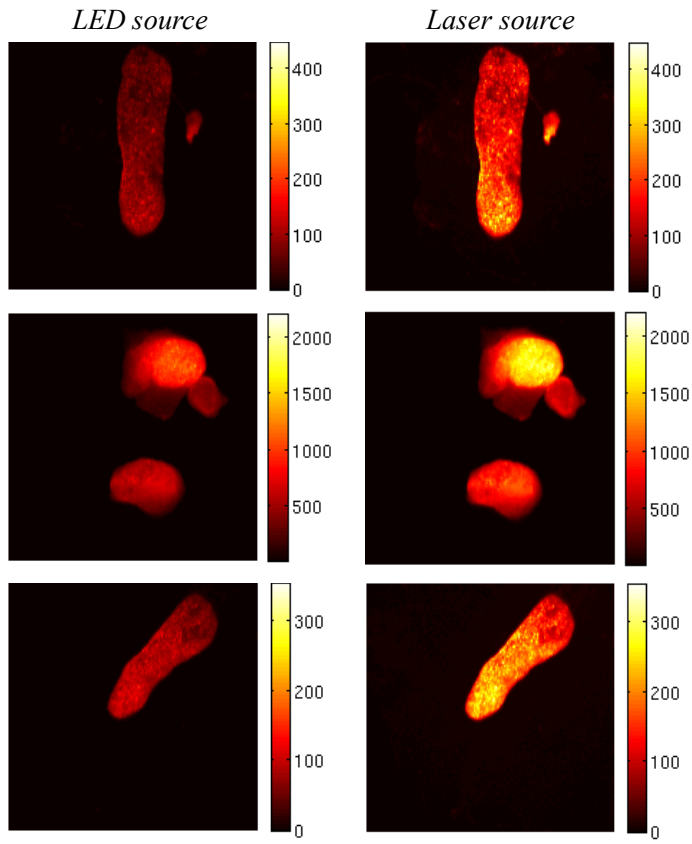

Figure 6.15. *The fluorescence obtained from the two sources. LEDs on the left are emitting less fluorescence due its broader bandwidth, compared to the laser. The top row is the spleen from a 4 h mouse, the middle row is the tumor from the same 4 hour mouse and the bottom is the spleen from an 8 h mouse.*

Comments on the Papers

I **Tunable high-power narrow-linewidth semiconductor laser based on an external-cavity tapered amplifier**

M. Chi, O. B. Jensen, J. Holm, C. Pedersen, P. E. Andersen, G. Erbert, B. Sumpf, and P. M. Petersen. *Opt. Express* **13**, 10589 (2005).

This paper is the first implementation of the tapered amplifier, in the Littrow configuration. The basic laser properties such as output power, tuning range and beam quality parameter M^2 are measured and reported. This was the first report of a tapered amplifier operating around 808 nm.
I participated in the planning and took part in the initial experiments.

II **Wavelength stabilization of extended-cavity tapered lasers with volume Bragg gratings**

G. Lucas-Leclin, D. Paboeuf, P. Georges, J. Holm, P. Andersen, B. Sumpf, and G. Erbert. *Appl. Phys. B* **91**, 493-498 (2008).

A tapered amplifier was stabilized in an external cavity configuration, but using a volume Bragg grating instead of a dispersive reflection grating. Again basic properties of the laser were measured and reported. In order to characterize the beam spatially and spectrally, a single pass second harmonic generation setup in a bulk PPKTP was performed.
I participated in all the measurements regarding the beam quality and second harmonic generation.

III **Generation of more than 300 mW diffraction-limited light at 405 nm by second-harmonic generation of a tapered diode laser with external cavity feedback**

O. B. Jensen, J. Holm, B. Sumpf, G. Erbert, P. E. Andersen, and P. M. Petersen.
Proceedings of SPIE **6455**, 645503 (2007).

This paper explored the bowtie resonator geometry and the usage of a shorter 10 mm PPKTP crystal. We observed the strong thermal dephasing behavior later reported in Paper **V**. The crystal suffered from severe grey tracking, indicating a too small beam waist in the crystal. This was remedied in the later papers by using a 30 mm crystal instead.
I participated in the experimental measurements.

IV **High power 404 nm source based on second harmonic generation in PPKTP of a tapered external feedback diode laser**

J. H. Lundeman, O. B. Jensen, P. E. Andersen, S. Andersson-Engels, B. Sumpf, G. Erbert, and P. M. Petersen.
Opt. Expres **16**, 2486 (2008).

A new laser source using an optimized design of that reported in Paper **I**. An even larger waveguide laser was used, in order to enhance the coupling, and the mount was improved in terms of cooling method and mechanical stability. The laser source was then coupled into an external resonator with a PPKTP crystal. The resonator was polarization phase locked and the basic attributes were reported in the paper.
I made all the experiments, and wrote the paper.

V **Threshold for strong thermal dephasing in periodically poled KTP in frequency doubling of an 808 nm high power tapered diode.**

J. H. Lundeman, O. B. Jensen, P. E. Andersen, and P. M. Petersen.
submitted to Appl. Phys. B.

In order to optimize the resonator in Paper **IV** four different resonators were constructed and characterized. From these results the relationship between the single pass conversion efficiency parameter and the temperature bandwidth reduction was found.
I made all the experiments, and wrote the paper.

VI **Pharmacokinetic study following systemic administration of a pegylated liposomal temoporn formulation using uorescence imaging techniques**

P. Svenmarker, J Axelsson, S. Grafe, J. H. Lundeman, H. Cheng, H. Xie, , N. Bendsoe, S. Svanberg, P. Andersen, K. Svanberg, and S. Andersson-Engels.
manuscript in preparation.

The laser source from Paper **IV** was used in the measurements of the pharmacokinetics of pegylated mTHPC injected in mice. A dose were administered to each of the mice, that were later sacrificed after 0.5, 2, 4, 8 and 18 hours. Immediately after the laser-induced fluorescence of the organs were collected when illuminated with the 404 nm source in cw mode. The recorded fluorescence was compared to the measured concentration obtained via a HPLC process.
I participated in all the fluorescence experiments and contributed to the writing of the manuscript.

VII **Bleaching of the age-related colouration of human donor lenses using monochromatic laser light**

L. Kessel, L. Eskildsen, J. H. Lundeman, O. B. Jensen, and M. Larsen.
Submitted to: Experimental Eye Research.

Human crystalline donor lenses with age related opacification, were treated with different lasers and the change in transmission were measured. The blue laser at 404 nm were used as well as a YAG, doubled and tripled. I participated in all the experiments with the blue laser and the doubled YAG.

Acknowledgements

A lot of people have supported and helped me over the years, directly related to the project or indirectly by making it possible for me to do work at all.

First I would like to thank my supervisors at Risø, Peter Eskil Andersen and Paul Michael Petersen for their believe in me and the project. They encouraged me and supported my work throughout the years. I enjoyed the many discussions we had about the various aspects of science and the project in general.

I would also like to express my gratitude towards Ole Bjarlin Jensen, who effectively became my lab-mate at Risø. I really appreciated the countless discussions about science, industry and other topics. I enjoyed the collaboration we did on several of the experimental setups, and learned a lot in the process.

From Risø I would like to thank Mingjuin Chi, Christian Pedersen and Bjarne Sass for your commitment to getting these tapered diodes up and running. It was a long and rocky path, but it paid off in the end. Birgitte Thestrup Nielsen, Eva Samsøe, Frederik D. Nielsen, Sren Blaaberg Jensen, you were all great colleagues, who taught me a lot in your different fields. I express my gratitude for having worked with all of you, and for the help you were always ready to supply if needed. Haynes Cheng thank you for being a very good travelling companion on our trip to Jena.

The group at Lund deserves a special thanks, as you always seemed ready to stop doing what you were presently doing and rush equipment into the clinic for some testing on patients, whenever I ventured over the bridge with the laser system in the back of the van.

To my supervisor Stefan Andersson-Engels, thank you for always taking the time to make sure the topic at hand was understood by me. And for the time and effort you put into getting the issues solved in the lab, ultimately stepping in yourself if needed. I truly admire that dedication and collaboration within your group.

Johan Axelsson and Pontus Svenmarker, thank you for the untiring working from you guys. I will always remember our trip to Jena and the clinical work we did on patients, as well as the experiments done in the lab, with ALA-cream applied to our own

arms.

Katarina Svanberg and in particular Niels Bendsøe who allowed the experimental diagnostics technique to be performed under close medical control in the clinic. Your optimism and excitement about the results as well as possible future applications were really a driving force pushing me forward.

Finally I need to give my deepest gratitude to my wife Anja, who endured four long years with a husband that many a night needed to work in the lab. Thank you for your support and cheering up when results were not exactly as expected; I could not have done all this without you.

References

1. T. H. Maiman. *Stimulated Optical Radiation in Ruby.* Nature **187**, 493–494 (1960).

2. R. N. Hall, G. E. Fenner, J. D. Kingsley, T. J. Soltys and R. O. Carlsson. *Coherent Light emission from GaAs Junctions.* Phys. Rev. Lett. **9**, 366–368 (1962).

3. M. I. Nathan, W. P. Dumke, G. Burns, F. H. Dill Jr and G. Lasher. *Stimulated emission of radiation from GaAs p-n junctions.* Appl. Phys. Lett. **1**, 62–64 (1962).

4. T. M. Quist, R. H. Rediker, R. J. Keyes, W. E. Krag, B. Lax, A. L. Whorter and H. J. Ziegler. *Semiconductor maser of GaAs.* Appl. Phys. Lett. **1**, 91–92 (1962).

5. B. G. Streetman and S. Banerjee. *Solid State electronic Devices.* Prentice Hall New Jersey 5th edition (2005). ISBN 0-13-025538-6.

6. H. Kressel and J. K. Butler. *Semiconductor Lasers and Hererojunction LEDs.* Academic Press New York (1977). ISBN 0-12-426250-3.

7. Peter Unger. *Introduction to Power Diode Lasers.* In R. Diehl, editor, *High-Power Diode Lasers : Fundamentals, Technology, Applications.* Springer Verlag (2000).

8. N. K. Dutta. *Basic principles of laser diodes.* In D. Webb and J. Jones, editors, *Handbook of Laser Technology and Applications: volume II* pages 525–560. Institute of Physics Publishing (2004). ISBN 0750309636.

9. G. P. Agrawal and N. K. Dutta. *Semiconductor Lasers.* Van Nostrand Reinhold New York 2nd ed. edition (1993).

10. M. Mikulla. *Tapered High-Power, High-Brightness Diode Lasers: Design and Performance.* In R. Diehl, editor, *High-Power Diode Lasers : Fundamentals, Technology, Applications.* Springer Verlag (2000).

11. A. Knauer, G. Erbert, R. Staske, B. Sumpf, H. Wenzel and M. Weyers. *High-power 808 nm lasers with a super-large optical cavity.* Semicond. Sci. Technol. **20**, 621–624 (2005).

12. M. Osinski and J. Buus. *The Linewidth Broadening Factor in Semiconductos Lasers - an Overview.* IEEE J. Quantum Electron. **QE-23**, 9–29 (1987).

13. G. P. Agrawal. *Fast-Fourier-Transform based beam-propagation model for stripe-geometry semiconductor lasers.* J. Appl. Phys. **56**, 3100–3109 (1984).

14. J. R. Marciante and G. P. Agrwal. *Controlling filamentation in broad-area semiconductor lasers and amplifiers.* Appl. Phys. Lett. **69**, 593–595 (1996).

15. B. Dahmani, L. Hollberg and R. Drullinger. *Frequency stabilization of semiconductor lasers by resonant optical feedback.* Opt. Lett. **12**, 876–878 (1987).

16. H. Stoehr, F. Mensing, J. Helmcke and U. Sterr. *Diode laser with 1 Hz linewidth.* Opt. Lett. **31**, 736–738 (2006).

17. A. D. Ludlow, X. Huang, M. Notcutt, T. Zanon-Willette, S. M. Foreman, M. M. Boyd, S. Blatt and J. Ye. *Compact, thermal-noise-limited optical cavity for diode laser stabilization at* 1×10^{15}. Opt. Lett. **32**, 641–643 (2007).

18. J. Alnis, A. Matveev, N. Kolachevsky, T. Wilken, T. Udem and T. W. Hansch. *Sub-Hz line width diode lasers by stabilization to vibrationally and thermally compensated ULE Fabry-Perot cavities.* arXiv:0801.4199v1 (2008).

19. H. Kogelnik and C. V. Shank. *Stimulated Emission In a Periodic Structure.* Appl. Phys. Lett. **18**, 152–154 (1971).

20. H. Kogelnik and C. V. Shank. *Coupled-wave theory of distributed feedback lasers.* J. Appl. Phys. **43**, 2327–2335 (1972).

21. D. M. Bird, J.R Armitage, R. Kashyap, R.M.A. Fatah and K.H. Cameron. *Narrow line semiconductor laser using fibre grating.* Electron. Lett. **27**, 1115–1116 (1991).

22. P. A. Morton, V. Mizrahi, T. Tanbun-Ek, R. A. Logan, Lemaire P. J., H. M. Presby, T. Erdogan, S. L. Woodward, J. E. Sipe, M. R. Phillips, A. M. Sergent and K. W. Wecht. *Stable single mode hybrid laser with high power and narrow linewidth.* Appl. Phys. Lett. **64**, 2634–2636 (1994).

23. A. K. Goyal, P. Gavrilovic and H. Po. *1.35 W of stable single-frequency emission from an external-cavity tapered oscillator utilizing fiber Bragg grating feedback.* Appl. Phys. Lett. **73**, 575–577 (1998).

24. B. L. Volodin, S. V. Dolgy, E. D. Melnik, E. Downs, J. Shaw and V. S. Ban. *Wavelength stabilization and spectrum narrowing of high-power multimode laser diodes and arrays by use of volume Bragg gratings.* Opt. Lett. **29**, 1891–1893 (2004).

25. M. G. Littman and H. J. Metcalf. *Spectrally narrow pulsed dye laser without beam expander.* Appl. Opt. **17**, 2224–2227 (1978).

26. William P. Risk, Timothy R. Gosnell and Arto V. Nurmikko. *Compact Blue-Green Lasers.* Cambridge University Press Cambridge, UK (2003). ISBN 0-521-52103-3.

27. D. D. Cook and F. R. Nash. *Gain-induced guiding and astigmatic ouput of GaAs lasers.* J. Appl. Phys. **46**, 1660–1672 (1975).

28. J. Hendrix, G. Morthier and R. Baets. *Influence of Laser Parameters and Unpumped Regions Near the Facets on the Power Level for Catastrophic Optical Damage in Short Wavelength Lasers.* IEE Proc. Optoelectron. **144**, 109–114 (1997).

29. *Material and Fabrication-Related Limitations to High-Power Operation of GaAs/AlGaAs and InGaAs/AlGaAs Laser Diodes.* Mat. Sci. Eng. B **44**, 359–363 (1997).

30. G. H. B. Thompson. *A theory for filamentation in semiconductor lasers including the dependence of dielectric constant on injected carrier density.* Optoelectron. **4**, 257–310 (1972).

31. E. Samsøe. *Laser diode systems for photodynamic therapy and medical diagnostics.* PhD thesis Lund University Lund, Sweden (2004).

32. R. Waarts, S. Sanders, R. Parke, D. Mehuys, D. Lang, S. O'Brien, K. Dzurko, D. Welch and D. Scifres. *Frequency-Doubled Monolithic Master Oscillator Power Amplifier Laser Diode.* IEEE Photon. Technol. Lett. **5**, 1122–1125 (1993).

33. A. K. Goyal, P. Gavrilovic and H. Po. *Stable single-frequency operation of a high-power external cavity tapered diode laser at 780 nm.* Appl. Phys. Lett. **71**, 1296–1298 (1997).

34. J. N. Walpole. *Semiconductor amplifiers and lasers with tapered gain regions.* Opt. Quantum Electron. **28**, 623–645 (1996).

35. E. S. Kintzer, J. N. Walpole, S. R. Chinn, C. A. Wang and L. J. Missaggia. Proc. Conference on Lasers and Electro-Optics pages Technical Digest, paper TuH5 (1992).

36. J. N. Walpole, E. S. Kintzer, S. R. Chinn, C. A. Wang and L. J. Missaggia. *High-power strained-layer InGaAs/AlGaAs tapered traveling wave amplifier.* Appl. Phys. Lett. **61**, 740–742 (1992).

37. D. Mehuys, D. F. Welch and L. Goldberg. *2.0 W CW, diffraction-limited tapered amplifier with diode injection.* Electron. Lett. **28**, 1944–1946 (1992).

38. E. S. Kintzer, J. N. Walpole, S. R. Chinn, C. A. Wang and L. J. Missaggia. *High-power, strained-layer amplifiers and lasers with tapered gain regions.* IEEE Photon. Technol. Lett. **5**, 605–608 (1993).

39. C. A. Wang and H. K. Choi. *Organometallic vapor phase epitaxy of high-performance strained-layer InGaAs-AlGaAs diode lasers.* IEEE J. Quantum Electron. **27**, 681–685 (1991).

40. D. Mehuys, S. O'Brien, R. J. Lang, A. Hardy and D. F. Welch. *5 W, diffraction-limited, tapered-stripe unstable resonator semiconductor laser.* Electron. Lett. **30**, 1855–1856 (1994).

41. S. O'Brien, D. Mehuys, R. J. Lang and D. F. Welch. *1 W CW single frequency, diffraction-limited unstable resonator semiconductor laser with distributed Bragg reflector mirrors.* Electron. Lett. **31**, 203–205 (1995).

42. B. Sumpf, R. Hulswede, G. Erbert, C. Dzionk, J. Fricke, A. Knauer, W. Pittroff, H. Wenzel and G. Trankle. *High brightness 735 nm tapered diode lasers.* Electron. Lett. **38**, 183–184 (2002).

43. B. Sumpf, G. Beister, G. Erbert, J. Fricke, A. Knauer, P. Ressel and G. Trankle. *Reliable 1-W CW Operation of High-Brightness Tapered Diode Lasers at 735 nm.* IEEE Photon. Technol. Lett. **16**, 984–986 (2004).

44. F. Dittmar, B. Sumpf, J. Fricke, G. Erbert and G. Trankle. *High-Power 808-nm Tapered Diode Lasers With Nearly Diffraction-Limited Beam Quality of M^2 = 1.9 at P = 4.4 W.* IEEE Photon. Technol. Lett. **18**, 601–603 (2006).

45. F. Dittmar, A. Klehr, B. Sumpf, A. Knauer, J. Fricke, G. Erbert and G. Trankle. *9-W Output Power From an 808-nm Tapered Diode Laser in Pulsed Mode Operation With Nearly Diffraction-Limited Beam Quality.* IEEE J Sel. Top. Quant. **13**, 1194–1199 (2007).

46. F. Dittmar, B. Sumpf, G. Erbert and G. Trankle. *Long-term reliability studies of high-power 808 nm tapered diode lasers with stable beam quality.* Semicond. Sci. Technol. **22**, 374–379 (2007).

47. A. E. Siegman. *How to (Maybe) Measure Laser Beam Quality.* Tutorial given at the Optical Society of America Annual Meeting (1997).

48. C. Pedersen and R. S. Hansen. *Single frequency, high power, tapered diode laser using phase-conjugated feedback.* Opt. Exp. **13**, 3961–3968 (2005).

49. E. Gehrig and O. Hess. *Dynamics of High-Power Diode Lasers.* In R. Diehl, editor, *High-Power Diode Lasers : Fundamentals, Technology, Applications.* Springer Verlag (2000).

50. S. Nakamura, S. Pearton and G. Fasol. *The Blue Laser Diode.* Springer Berlin 2nd ed. edition (2000).

51. http://www.nichia.com (June 2008).

52. W. R. Rapoport and C. P. Khattak. *Titanium sapphire laser characteristics.* Appl. Opt. **27**, 2677–2684 (1988).

53. P. A. Franken, A. E. Hill, C. W. Peters and G. Weinreich. *Generation of optical harmonics.* Phys. Rev. Lett. **7**, 118–119 (1961).

54. Richard P. Feyman. *The Feynman Lectures on Physics* volume 2. Addison-Wesley Menlo Park, California (1964). ISBN 0-201-02117-X.

55. Paul Michael Petersen and Torben Skettrup. *Ulineær Optik.* Polyteknisk Forlag Lyngby, Denmark (1994). ISBN 87-502-0756-3.

56. Richard L. Sutherland. *Handbook of Nonlinear Optics.* Marcel Dekker New York (1996). ISBN 0-824-79426-5.

57. J. A. Armstrong, N. Bloembergen, J. Ducuing and P. S. Pershan. *Interactions between light waves in a nonlinear dielectric.* Phys. Rev. **127**, 1918–1939 (1962).

58. A. E. Siegman. *Why the sinc function should be defined as* $(sinx)/x$ *and not as* $(sin\pi x)/(\pi x)$. Appl. Opt. **13**, 705–706 (1974).

59. Tso Yee Fan, C. E. Huang, B. Q. Hu, R. C. Eckardt, Y. X. Fan, Robert L. Byer and R. S. Feigelson. *Second harmonic generation and accurate index of refraction measurements in flux-grown KTiOPO4.* Appl. Opt. **26**, 2390 (1987).

60. M. Born and E. Wolf. *Principles of Optics.* Cambridge University Press Cambridge, UK 7th (expanded) edition (2002).

61. G. D. Boyd and D. A. Kleinman. *Parametric Interaction of Focused Gaussian Light Beams.* J. Appl. Phys. **39**, 3597–3639 (1968).

62. M. M. Fejer, G. A. Magel, D. H. Jundt and R. L. Byer. *Quasi-phase-matched second harmonic generation: Tuning and tolerances.* IEEE J. Quantum Electron. **28**, 2631–2654 (1992).

63. N. Bloembergen and A. J. Sievers. *Nonlinear optical properties of periodic laminar structures.* Appl. Phys. Lett. **17**, 483–486 (1970).

64. C. F. Dewey and L. O. Hocker. *Enhanced nonlinear optical effects in rotationally twinned crystals.* Appl. Phys. Lett. **26**, 442–444 (1975).

65. M. Okada, K. Takizawa and S. Ieiri. *Second harmonic generation by periodic laminar structure of nonlinear optical crystal.* Opt. Comm. **18**, 331–334 (1976).

66. D. E. Thompson, J. D. Mcmullen and D. B. Anderson. *Second-harmonic generation in GaAs "stack of plates" using high-power CO_2 laser radiation.* Appl. Phys. Lett. **29**, 113–115 (1976).

67. Y. Taira. *High-Power Continous-Wave Ultraviolet Generation by Frequency Doubling of an Argon Laser.* Jpn. J. Appl. Phys. **31**, L682–L684 (1992).

68. F. M. Librecht and J. A. Simmons. *Second-Harmonic Generation in Birefringent Crystals by a Gaussian Beam with an Elliptical Cross Section.* IEEE J. Quantum Electron. **QE-11**, 850–852 (1975).

69. G. D. Boyd, A. Ashkin, J. M. Dziedzic and D. A. Kleinman. *Second-harmonic generation using a focused Gaussian laser beam.* Phys. Rev. **137**, 1305–1320 (1965).

70. J. E. Bjorkholm. *Optical second-harmonic generation using a focused Gaussian laser beam.* Phys. Rev. **142**, 126–136 (1966).

71. T. Freegarde, J. Coutts, J. Walz, D. Leibfried and T. W. Hansch. *General analysis of type I second-harmonic generation with elliptical Gaussian beams.* J. Opt. Soc. Am. B **14**, 2010–2016 (1997).

72. A. Steinbach, M. Rauner, F. C. Cruz and J. C. Bergquist. *CW second harmonic generation with elliptical Gaussian beams.* Opt. Comm. **123**, 207–214 (1996).

73. D. McGloin and K. Dholakia. *Bessel beams: diffraction in a new light.* Contemporary Physics **46**, 15–28 (2005).

74. K. Shinozaki, C q. Xu, H. Sasaki and T. Kamijoh. *A comparison of optical second-harmonic generation efficiency using Bessel and Gaussian beams in bulk crystals.* Opt. Comm. **133**, 300–304 (1997).

75. J. Arlt, K. Dholakia, L. Allen and M. J. Padgett. *Efficiency of second-harmonic generation with Bessel beams.* Phys. Rev. A **60**, 2438–2441 (1999).

76. A. E. Siegman. *Lasers.* University Science Books Mill Valley, California (1986).

77. V. Magni. *Optimum beam for second harmonic generation.* Opt. Comm. **176**, 245–251 (2000).

78. V. Magni. *Optimum beams for effcient frequency mixing in crystals with second order nonlinearity.* Opt. Comm. **184**, 245–255 (2000).

79. V. G. Dmitriev, G. G. Gurzadyan and D. N. Nikogosyan. *Handbook of Nonlinear Optical Crystals.* Springer Berlin 2nd edition (1997). ISBN 3-540-61275-0.

80. National Labs Sandia. SNLO Sofware (version 40).

81. F. C. Zumsteg, J. D. Bierlein and T. E. Gier. *$K_xRb_{1-x}TiOPO_4$: A new nonlinear optical material.* J. Appl. Phys. **47**, 4980–4985 (1976).

82. G. Hansson, H. Karlsson, S. Wang and F. Laurell. *Transmission measurements in KTP and isomorphic compounds.* Appl. Opt. **39**, 5058–5069 (2000).

83. John D. Bierlein and Herman Vanherzeele. *Potassium titanyl phosphate: properties and new applications.* J. Opt. Soc. Am. B **6**, 622–633 (1989).

84. T. A. Driscoll, H. J. Hoffman and R. E. Stone. *Efficient second-harmonic generation in KTP crystals.* J. Opt. Soc. Am. B **3**, 683–686 (1986).

85. R. Blachman, P. F. Bordui and M. M. Fejer. *Laser-induced photochromic damage in potassium titanyl phosphate.* Appl. Phys. Lett. **64**, 1318–1320 (1994).

86. B. Boulanger, M. M. Fejer, R. Blachman and P. F. Bordui. *Study of $KTiOPO_4$ gray-tracking at 1064, 532, and 355 nm.* Appl. Phys. Lett. **65**, 2401–2403 (1994).

87. D. W. Anthon and C. D. Crowder. *Wavelength dependent phase matching in KTP.* Appl. Opt. **27**, 2650–2652 (1988). Letters to the editor.

88. G. M. Loiacono, R. A. Stoltzenberger and D. N. Loiacono. *Modified $KTiOPO_4$ crystals for nonncritical phase matching applications.* Appl. Phys. Lett. **64**, 16–18 (1994).

89. Y. S. Liu, D. Dentz and R. Belt. *High-average-power intracavity second-harmonic generation using $KTiOPO_4$ in an acousto-optically Q-switched Nd:YAG laser oscillator at 5 kHz.* Opt. Lett. **9**, 76–78 (1984).

90. M. V. Pack, D. J. Armstrong and A. V. Smith. *Measurement of the $\chi^{(2)}$ tensors of $KTiOPO_4$, $KTiOAsO_4$, $RbTiOPO_4$, and $RbTiOAsO_4$ crystals.* Appl. Opt. **43**, 3319–3323 (2004).

91. Q. Chen and W. P. Risk. *Periodcally Poling of KTiOPO4 using an applied electric field.* Electron. Lett. **30**, 1516–1517 (1994).

92. H. Karlsson and F. Laurell. *Electric field poling of flux grown $KTiOPO_4$.* Appl. Phys. Lett. **71**, 3474–3476 (1997).

93. A. Arie, Rosesnman G., V. Mahal, A. Skliar, M. Oron, M. Katz and D. Eger. *Green and ultraviolet quasi-phase-matched second harmonic generation in bulk periodically-poled KTiOPO4.* Opt. Comm. **142**, 265–268 (1997).

94. S. Wang, V. Pasiskevicius, F. Laurell and H. Karlsson. *Ultraviolet generation by first-order frequency doubling in periodically poled $KTiOPO_4$.* Opt. Lett. **23**, 1883–1885 (1998).

95. I. Juwiler, A. Arie, A. Skliar and G. Rosenman. *Efficient quasi-phase-matched frequency doubling with phase compensation by a wedged crystal in a standing-wave external cavity.* Opt. Lett. **24**, 1236–1238 (1999).

96. F. Torabi-Goudarzi and E. Riis. *Efficient cw high-power frequency doubling in periodically poled KTP.* Opt. Comm. **227**, 389–403 (2003).

97. R. Le Targat, J.-J. Zondy and P. Lemonde. *75%-Efficiency blue generation from an intracavity PPKTP frequency doubler.* Opt. Comm. **247**, 471–481 (2005).

98. A. Ashkin, G. D. Boyd, J. M. Dziedzic, R. G. Smith, A. A. Ballman, J. J. Levinstein and K. Nassau. *Optically-induced refractive index inhomogeneities in $LiNbO_3$ and $LiTaO_3$.* Appl. Phys. Lett. **9**, 72–74 (1966).

99. D. A. Bryan, R. Gerson and H. E. Tomaschke. *Increased optical damage resistance in lithium niobate.* Appl. Phys. Lett. **44**, 847–849 (1984).

100. J.-P. Meyn, C. Laue, R. Knappe, R. Wallenstein and M. M. Fejer. *Fabrication of periodically poled lithium tantalate for UV generation with diode lasers.* Appl. Phys. B **73**, 111–114 (2001).

101. C. Chen, Y. Wu, A. Jiang, B. Wu, G. You, R. Li and S. Lin. *New nonlinear-optical crystal: LiB3O5.* J. Opt. Soc. Am. B **6**, 616 (1989).

102. D. Eimerl, L. Davis, S. Velsko, E. K. Graham and A. Zalkin. *Optical, mechanical, and thermal properties of barium borate.* J. Appl. Phys. **62**, 1968–1983 (1987).

103. H. Hellwig, J. Liebertz and L. Bohaty. *Linear optical properties of the monoclinic bismuth borate BiB_3O_6.* J. Appl. Phys. **88**, 240–244 (2000).

104. H. Kogelnik. Bell Syst. Tech. J. **44**, 455 (1965).

105. T. Freegarde and C. Zimmerman. *On the design of enhancement cavities for second harmonic generation.* Opt. Comm. **199**, 435–446 (2001).

106. A. Ashkin, G. D. Boyd and J. M. Dziedzic. *Resonant Optical Second Harmonic Generation and Mixing.* IEEE J. Quantum Electron. **QE-2**, 109–124 (1966).

107. W. J. Kozlovsky, C. D. Nabors and R. L. Byer. *Efficient second harmonic generation of a diode-laser-pumped CW Nd:YAG laser using monolithic $MgO:LiNbO_3$ external resonant cavities.* IEEE J. Quantum Electron. **24**, 913–919 (1988).

108. A. Maitland and M. H. Dunn. *Laser Physics.* North-Holland Publishing Company Amsterdam (1969). ISBN 720401534.

109. H. Kogelnik. *Coupling and conversion coefficients for optical modes.* Proc. Symp. on Quasi Optics pages 333–347 (1964).

110. A. Douillet, J.-J. Zondy, A. Yelisseyev, S. Lobanov and L. Isaenko. *Stability and frequency tuning of thermally loaded continuous-wave $AgGaS_2$ optical parametric oscillators.* J. Opt. Soc. Am. B **16**, 1481–1498 (1999).

111. V. Magni. *Multielement stable resonators containing a variable lens.* J. Opt. Soc. Am. B **4**, 1962–1969 (1987).

112. I. Juwiler and A. Arie. *Efficient frequency doubling by a phase-compensated crystal in a semimonolithic cavity.* Appl. Opt. **42**, 7163–7169 (2003).

113. E. S. Polzik and H. J. Kimble. *Frequency doubling with $KNbO_3$ in an external cavity.* Opt. Lett. **16**, 1400–1402 (1991).

114. M. E. Innocenzi, H. T. Yura, C. L. Fincher and R. L. Fields. *Thermal modelling of continous-wave end-pumped solid-state lasers.* Appl. Phys. Lett. **56**, 1831–1833 (1990).

115. A. Sennaroglu, A. Askar and F. M. Atay. *Quantitative study of laser beam propagation in a thermally loaded absorber.* J. Opt. Soc. Am. B **14**, 356–363 (1997).

116. M. R. Spiegel. *Mathematical Handbook of Formulas and Tables.* Schaum's Outline Series. McGraw-Hill 35th printing edition (1996). ISBN 0070602247.

117. A. D. Ludlow, H. M. Nelson and S. D. Bergeson. *Two-photon absorption in potassium niobate.* J. Opt. Soc. Am. B **18**, 1813–1820 (2001).

118. P. Dube, L.-S. Ma, J. Ye, P. Jungner and J. L. Hall. *Thermally induced self-locking of an optical cavity by overtone absorption in acetylene gas.* J. Opt. Soc. Am. B **13**, 2041–2054 (1996).

119. P. L. Hansen and P. Buchhave. *Thermal self-frequency locking of a doubly resonant optical parametric oscillator.* Opt. Lett. **22**, 1074–1076 (1997).

120. T. Ikegami, S. Slyusarev, T. Kurosu, Y. Fukuyama and S. Ohshima. *Characteristics of a cw monolithic KTiOPO4 optical parametric oscillator.* Appl. Phys. B **66**, 719–725 (1998).

121. T. W. Hansch and B. Couillaud. *Laser frequency stabilization by polarization spectroscopy of a reflecting resonance cavity.* Opt. Comm. **35**, 441–444 (1980).

122. A. Hemmerich, D. H. McIntyre, C. Zimmerman and T. W. Hansch. *Second-harmonic generation and optical stabilization of a diode laser in an external ring resonator.* Opt. Lett. **15**, 372–374 (1990).

123. B. Beier, D. Woll, M. Scheidt, K.-J. Boller and R. Wallenstein. *Second harmonic generation of the output of an AlGaAs diode oscillator amplier system in critically phase matched LiB_3O_5 and -BaB_2O_4.* Appl. Phys. Lett. **71**, 315–317 (1997).

124. D. Woll, B. Beier, K.-J. Boller, R. Wallenstein, M. Hagberg and S. O'Brien. *1 W of blue 465-nm radiation generated by frequency doubling of the output of a high-power diode laser in critically phase-matched LiB_3O_5.* Opt. Lett. **24**, 691–693 (1999).

125. J. D. Bhalwalkar, Y. Mao, A. K. Goyal, P. Gavrilovic, Y. Conturie and S. Singh. *High-power 390-nm laser source based on efficient frequency doubling of a tapered diode laser in an external resonant cavity.* Opt. Lett. **24**, 823–825 (1999).

126. R. V. Pound. *Electronic frequency stabilization of microwave oscillators.* Rev. Sci. Instrum. **17**, 490–505 (1946).

127. R. W. P. Drever, J. L. Hall, F. V. Kowalski, J. Hough, G. M. Ford and A. J. Munley. *Laser phase and frequency stabilization using an optical resonator.* Appl. Phys. B **31**, 97–105 (1983).

128. Y. Kaneda and S. Kubota. *Continuous-wave 355-nm laser source based on doubly resonant sum-frequency mixing in an external resonator.* Opt. Lett. **20**, 2204–2206 (1995).

129. A. Arie, G. Rosenman, A. Korenfeld, A. Skliar, M. Oron, M. Katz and D. Eger. *Efficient resonant frequency doubling of a cw Nd:YAG laser in bulk periodically poled $KTiOPO_4$.* Opt. Lett. **23**, 28–30 (1998).

130. W. J. Kozlovsky, W. Lenth, E. E. Latta, A. Moser and G. L. Bonna. *Generation of 41 mW of blue radiation by frequency doubling of a GaAlAs diode laser.* Appl. Phys. Lett. **56**, 2291–2292 (1990).

131. W. J. Kozlovsky and W. Lenth. *Fast amplitude modulation of the blue 429-nm output from a frequency-doubled GaAlAs diode laser.* Opt. Lett. **19**, 195–197 (1994).

132. K. Hayasaka, Y. Zhang and K. Kasai. *Generation of 22.8 mW single-frequency green light by frequency doubling of a 50-mW diode laser.* Opt. Exp. **12**, 3567–3572 (2004).

133. G. J. Dixon, C. E. Tanner and C. E. Wieman. *432-nm source based on efficient second-harmonic generation of GaAlAs diode-laser radiation in a self-locking external resonant cavity.* Opt. Lett. **14**, 731–733 (1989).

134. P. G. Wigley, Q. Zhang, E. Miesak and G. J. Dixon. *High-power 467-nm passively locked signal-resonant sum-frequency laser.* Opt. Lett. **20**, 2496–2498 (1995).

135. W. J. Kozlovsky, W. P. Risk, W. Lenth, B. G. Kim, G. L. Bona, H. Jaeckel and D. J. Webb. *Blue light generation by resonator-enhanced frequency doubling of an extended-cavity diode laser.* Appl. Phys. Lett. **65**, 525–527 (1994).

136. X. G. Huang, W. K. Lee, S. P. Wong, J. P. Zhou and Z. X. Yu. *Effects of thermal lensing on stability and astigmatic compensation of a Z-fold laser cavity.* J. Opt. Soc. Am. B **13**, 2863–2868 (1996).

137. H. Kogelnik, E. P. Ippen, A. Dienes and C. V. Shank. *Astigmatical compensation cavities for cw dye laser.* IEEE J. Quantum Electron. **8**, 373–379 (1972).

138. G. W. Ross, M. Pollnau, P. G. R. Smith, W. A. Clarkson, P. E. Britton and D. C. Hanna. *Generation of high-power blue light in periodically poled $LiNbO_3$.* Opt. Lett. **23**, 171–173 (1998).

139. B. G. Klappauf, Y. Bidel, D. Wilkovski, T. Chaneliere and R. Kaiser. *Detailed study of an efficient blue laser source by second-harmonic generation in a semimonolithic cavity for the cooling of strontium atoms.* Appl. Opt. **43**, 2510–2527 (2004).

140. M. Brieger, H. Busener, A. Hese, F. v. Moers and A. Renn. *Enhancement of single frequency SGH in a passive ring resonator.* Opt. Comm. **38**, 423–426 (1981).

141. V. Ruseva and J. Hald. *Generation of UV light by frequency doubling in BIBO.* Opt. Comm. **236**, 219–223 (2004).

142. H. Abitan and T Skettrup. *Laser resonators with several mirrors and lenses with the bow-tie laser resonator with compensation for astigmatism and thermal lens effects as an example.* J. Opt. A: Pure Appl. Opt **7**, 7–20 (2005).

143. J. S. Nielsen. *Generation of 90-mW continuous-wave tunable laser light at 280 nm by frequency doubling in a KDP crystal.* Opt. Lett. **20**, 840–842 (1995).

144. D. C. Gerstenberger, G. E. Tye and R. W. Wallace. *Efficient second-harmonic conversion of cw single-frequency Nd:YAGlaser light by frequency locking to a monolithic ring frequency doubler.* Opt. Lett. **16**, 992–994 (1991).

145. W. P. Risk and W. J. Kozlovsky. *Efficient generation of blue light by doubly resonant sum-frequency mixing in a monolithic KTP resonator.* Opt. Lett. **17**, 707–709 (1992).

146. K. Fiedler, S. Schiller, R. Pachotta, P. Kurz and J. Mlynek. *Highly efficient frequency doubling with a doubly resonant monolithic total-internal-reflection ring resonator.* Opt. Lett. **18**, 1786–1788 (1993).

147. J.-L. Boulnois. *Photophysical processes in recent medical laser developments: A review.* Lasers Med. Sci. **1**, 47–66 (1986).

148. N. M. Navaone, C. F. Polo, A. L. Frisardi, N. E. Andrade and A. M. Battle. *Heme biosynthesis in human breast cancer-mimetic "in vitro" studies and some heme enzymatic activity levels.* Int. J. Biochem. **22**, 1407–1411 (1990).

149. M. Konda, N. Hirota, T. Takaoka and M. Kajiwara. *Heme-biosynthetic enzyme activities and porphyrin accumulation in normal liver and hepatoma cell lines of rat.* Cell. Biol. Toxicol. **9**, 95–105 (1993).

150. M. Kriegmair, R. Baumgartner, W. Lumper, R. Waidelich and A. Hofstetter. *Early clinical experience with 5-aminolevulinic acid for the photodynamic therapy of superficial bladder cancer.* Br. J. Urol. **77**, 667–671 (1996).

151. S. L. Marcus, R. S. Sobel, A. L. Golub, R. L. Caroll, S. Lundahl and D. G. Shulman. *Photodynamic therapy (PDT) and photodiagnosis (PD) using endogenous photosensitization induced by 5-aminolevulinic acid (ALA): current clinical and development status.* J. Clin. Laser Med. Surg. **14**, 59–66 (1996).

152. Q. Peng, T. Warloe, K. Berg, J. Moan, M. Kongshaug, K. E. Gierckshy and J. M. Nesland. *5-Aminolevulinic acid-based photodynamic therapy.* Cancer **79**, 2282–2308 (1997).

153. L. Gossner, M. Stolte, R. Sroka, K. Rick, A. May, E. G. Hahn and C. Ell. *Photodynamic ablation of high.grade dysplasia and early cancer in Barett's esophagus by means of 5-aminolevulinic acid.* Gastroenterology **114**, 448–455 (1998).

154. W. Stummer, S. Stocker, S. Wagner, H. Stepp, C. Fritsch, C. Goetz, A. E. Goetz, R. Kiefmann and H. J. reulen. *Intraoperative detection of malignant gliomas by 5-aminolevulinic acid-induced pophyrin fluorescence.* Neurosurgery **42**, 518–525 (1998).

155. T. Glanzmann, C. Hadjur, M. Zellwerger, P. Grosiean, M. Forrer, J. P. Ballini, P. Monnier, H. van den Bergh, C. K. Lim and G. Wagnieres. *Pharmacokinetics of tetra(m-hydroxyphenyl)chlorin in huiman plasma and individualized light dosimetry in photodynamic therapy.* Photochem. Photobiol. **67**, 596–602 (1998).

156. P. Westermann, T. Glanzmann, S. Andrejevic, D. R. Braichotte, M. Forrer, G. Wagnieres, P. Monnier, H. van den Bergh, J. P. Mach and S. Folli. *Long circulating half-life and high tumor selectivity on the photosensitizer meta-tetrahydroxyphenylchlorin conjugated to polyethylene glycol in nude mice grafted with a human colon carcinoma.* Int. J. Cancer **76**, 842–850 (1998).

157. M. H. Teiten, L. Bezdetnaya, P. Morliere, R. Santus and F. Guillemin. *Endoplasmatic reticulum and Golgi apparatus are teh preferential sites of Foscan localisation in cultured tumor cells.* Br. J. Cancer **88**, 146–152 (2003).

158. R. Gilies, G. Zonios, R. R. Anderson and N. Kollias. *Fluorescence excitation spectroscopy provides information about human skin in vivo.* J. Invest. Dermatol. **2000;115(suppl 4)**, 704–707 (2000).

159. B. C. Wilson, R. A. Weersink and L. Lilge. *Photodynamic Therapy Dosimetry.* In M.-A. Mycek and B. W. Pogue, editors, *Handbook of Biomedical Fluorescence* pages 529–561. Marcel Dekker New York (2003). ISBN 0-8247-0955-1.

160. H. Zeng and C. MacAulay. *Fluorescence Spectroscopy and Imaging for Skin Cancer Detection and Evaluation.* In M.-A. Mycek and B. W. Pogue, editors, *Handbook of Biomedical Fluorescence* pages 315–360. Marcel Dekker New York (2003). ISBN 0-8247-0955-1.

161. A. Johansson. *Spectroscopic Techniques for Photodynamic Therapy Dosimetry.* PhD thesis Lund University Lund, Sweden (2007).

162. J. Moan and K. Berg. *The photodegradation of porphyrins in cells can be used to estimate the tlifetime of singlet oxygen.* Photochem. Photobiol. **53**, 549–553 (1991).